A COMPUTATIONAL ASSESSMENT OF FLAME CHARACTERISTICS OF PREMIXED AND NON-PREMIXED ETHYLENE-OXYGEN COMBUSTION WITH A REDUCED CHEMICAL REACTION MECHANISM

by

Sam V. Cowart
Bachelor of Science, University of North Dakota, 2002
Master of Science, University of North Dakota, 2012

A Dissertation

Submitted to the Graduate Faculty

of the

University of North Dakota

In partial fulfillment of the requirements

for the degree of

Doctor of Philosophy

Grand Forks, North Dakota

May
2020

This dissertation, submitted by Sam V. Cowart in partial fulfillment of the requirements for the Degree of Doctor of Philosophy from the University of North Dakota, has been read by the Faculty Advisory Committee under whom the work has been done and is hereby approved.

Dr. Gautham Krishnamoorthy

Dr. Michael Mann

Dr. Frank Bowman

Dr. Edward Kolodka

Dr. Jerome Delhommelle

This dissertation is being submitted by the appointed advisory committee as having met all of the requirements of the School of Graduate Studies at the University of North Dakota and is hereby approved.

Dr. Chris Nelson
Associate Dean of the School of Graduate Studies

Date

PERMISSION

Title	A Computational Assessment of Flame Characteristics of Premixed and Non-premixed Ethylene-Oxygen Combustion With a Reduced Chemical Reaction Mechanism
Department	Chemical Engineering
Degree	Doctor of Philosophy

In presenting this dissertation in partial fulfillment of the requirements for a graduate degree from the University of North Dakota, I agree that the library of this University shall make it freely available for inspection. I further agree that permission for extensive copying for scholarly purposes may be granted by the professor who supervised my dissertation work or, in his absence, by the Chairperson of the department or the dean of the School of Graduate Studies. It is understood that any copying or publication or other use of this dissertation or part thereof for financial gain shall not be allowed without my written permission. It is also understood that due recognition shall be given to me and to the University of North Dakota in any scholarly use which may be made of any material in my dissertation.

Sam V. Cowart
May 2020

TABLE OF CONTENTS

LIST OF FIGURES

LIST OF TABLES

ACKNOWLEDGMENTS

I offer my sincere thanks to Dr. Gautham Krishnamoorthy, my academic advisor during my doctoral studies at the University of North Dakota. From my first inquiries into the Ph.D. program in the Chemical Engineering department, he was a solid advocate and supporter of my decision to attend and complete the program. Through numerous discussions, phone calls, emails, and extensive coursework, he guided me through the complex world of CFD simulation of combustion processes. I am grateful for his assistance and expertise. I look forward to future collaboration.

I would also like to acknowledge my dissertation committee members, Drs. Michael Mann, Frank Bowman, Edward Kolodka, and Jerome Delhommelle. Their support and encouragement were instrumental to my success through several iterations as a student at the University of North Dakota.

This entire endeavor would not have been possible without the support of several of the faculty at the United States Military Academy. Special thanks to BG (R) Leon Robert, COL John Burpo, LTC (R) Charles Elliott, and Dr. Andrew Biaglow are in order. Thank you, gentlemen, for selecting me to continue my contributions to the education, training, and inspiration of the Corps of Cadets.

The vast majority of my gratitude is saved for my wife Tara, and my son Caleb. Whatever my aspirations, you two have been the solid foundation that has allowed me to press on. Through late nights, early mornings, and years away from home, my mind always rested easy regarding the home front. I can’t say thanks enough to you guys. “It’s a ten!”

ABSTRACT

Conventional fuel-air combustion processes are widely used in the chemical processing industry, but often suffer from high NOx emissions and difficulties with CO_2 capture from flue gases. Oxy-fuel combustion offers advantages over fuel-air combustion that addresses these shortcomings. One possible fuel for oxy-fuel combustion is ethylene, a gas that is produced in large quantities industrially. The numerical literature regarding ethylene-oxygen combustion is limited in scope.

This study focuses on obtaining flame characteristics of premixed and non-premixed ethylene-oxygen combustion using numerical methods and computational fluid dynamics (CFD) approaches. This study offers several contributions to the current research: (1) the use of a reduced chemical reaction mechanism for ethylene combustion that has not been widely used, (2) numerical resolution of soot and radiative heat transfer effects in lean ($\Phi = 0.2$) premixed and non-premixed ethylene combustion systems, and (3) a methodology for obtaining accurate combustion characteristics while maintaining a low computational cost. Laminar flame speed, flame temperature, flame length, soot volume fraction, and radiant fractions are quantities of interest.

A commercially available CFD package is used to conduct simulations. Computational domains representative of experiments in ethylene combustion are designed and discretized to resolve flame characteristics while maintaining accumulation of numerical errors to less than 0.06%. Several unique inputs to the governing equations are added: a multi-step reaction mechanism, tailored radiation functions for CO_2 and H_2O, and the inclusion of acetylene as a precursor species for soot production.

In the premixed ethylene-oxygen study, flame velocities are reduced by up to 73% when radiative heat loss is accounted for and radiant fractions are in the range 0.12 – 0.17. In the non-premixed ethylene-oxygen study, soot profiles for oxygen indices between 21% - 90% are determined and compared against experimental measurements. Radiant fractions are in the range 0.09 – 0.26, depending on oxygen index. A model for the soot nucleation parameter is proposed that is validated against additional experiments.

This study shows that the application of a reduced reaction mechanism for premixed combustion of ethylene-oxygen is important for determination of flame characteristics that agree with experiment. This mechanism applied to non-premixed ethylene-oxygen combustion simulations performs equally well.

CHAPTER I

INTRODUCTION

Oxy-fuel combustion has been an active area of combustion research for several years. Oxy-fuel combustion differs from conventional fuel-air combustion such that the concentration of oxygen in the oxidizer stream is higher for oxy-fuel combustion than for fuel-air combustion due to the dominant presence of nitrogen in air. Oxy-fuel combustion is attractive from an environmental standpoint; the lack of nitrogen in the system eliminates the production of NOx while the resulting high concentration of carbon dioxide in the flue gas allows for easier CO_2 capture [1]. Much of the initial research was focused on hydrogen or light hydrocarbon combustion, as these fuels are heavily used and produced in industry. Another potential candidate for use as a fuel in oxy-fuel combustion systems is ethylene. Ethylene is the simplest olefin, is extremely flammable, and has a relatively high molecular weight with respect to other gaseous hydrocarbon fuels. The specific interest in ethylene combustion is due in part to its prevalence in organic compound production, and ethylene production has been linked to US GDP in recent years (see Figure 1.1) [2]. The global demand for ethylene was over 150 million metric tons in 2016, and it is produced in higher quantities than many other organic compounds [3, 4]. Ethylene has also been discussed as a potential fuel in the development of pulse detonation engines. The stable detonation characteristics of ethylene [5] along with its ability to ignite on a hot surface without the requirement for an external flame or spark [4, 6], makes it an interesting candidate for combustion research.

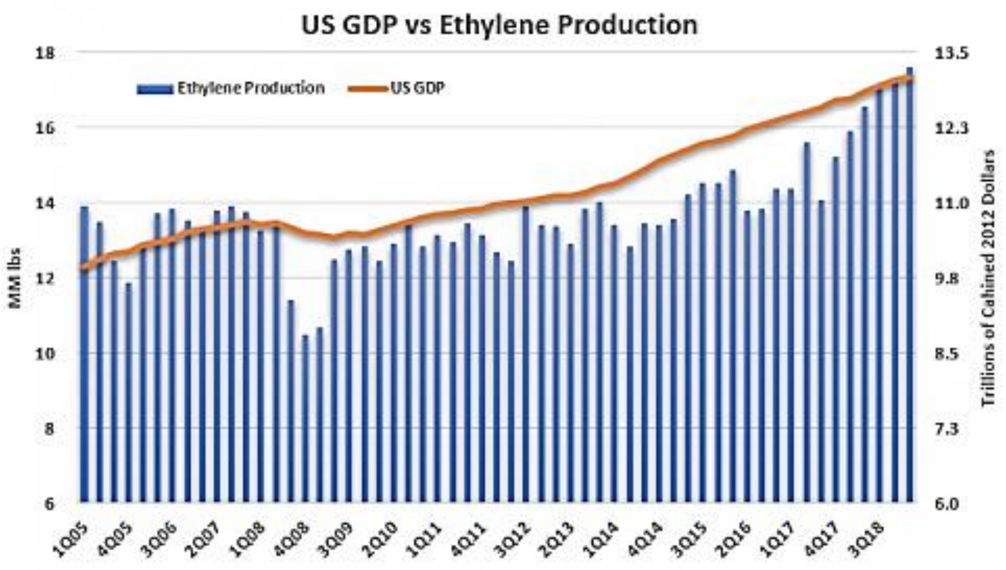

Figure 1.1. US ethylene production 2005 – 2018. Reprinted from [2].

The major approaches to combustion research in the literature are through experimental and numerical means. Experimental approaches in combustion focus on measuring flame temperatures, flame propagation velocities, fuel/air equivalence ratio limits, and ignition delay times. Numerically, much of the same information can be calculated with the added benefits of being able to rapidly change environmental conditions, examine chemical reaction details, and focus on individual aspects of the process such as transport phenomena or turbulence effects. This study focuses on numerical approaches.

Objectives and Hypotheses

The main objective of this study is to characterize ethylene-oxygen flames in both premixed and non-premixed combustion systems using computational fluid dynamics (CFD) approaches that are computationally efficient. Within the study of premixed combustion systems, the objectives are to examine and validate a multistep chemical reaction mechanism for the combustion of ethylene, model radiative heat loss from product gases, compare the effects of wall boundary and initialization conditions, and estimate accumulated error due to the process of discretizing time and space for calculation purposes. The main hypothesis for the premixed portion of this study is that the examined chemical reaction mechanism can be used for premixed systems to produce reasonably accurate results as compared to published experimental data. Two additional hypotheses are explored in this section: (1) radiative heat transfer effects resulting from the production of CO_2 and H_2O must be accounted for in small diameter tubes, and (2) flame propagation in small tubes can be accurately modeled with a no-cost, commercially available CFD code, negating the need for development of an in-house code.

In the non-premixed combustion section of this study, the objectives are to accurately model soot production and radiative heat transfer effects under low Reynolds number conditions at atmospheric pressure while varying oxygen concentration in the oxidizer stream. The major hypothesis for this section is that the same multistep reaction mechanism, using the same CFD code used in the premixed study, is applicable for producing accurate predictions of soot volume fraction in non-premixed systems at different oxygen indices. Further, the analysis of soot production in oxy-ethylene furnaces leads to the hypothesis that design and numerical simulations of these types of systems must account for radiative heat losses due to soot formation.

The overall contribution of this dissertation to the field of study in numerical analysis of combustion phenomena is through the development and use of computationally efficient methods to characterize flame velocities, temperatures, and heat transfer effects. These efficient methods involve invoking simplified chemical reaction mechanisms, radiation models, and computational meshes while obtaining results that are in general agreement with experimental literature.

Dissertation Organization

This dissertation is organized into a total of six chapters. Chapter 2 contains background theory into combustion processes, thermodynamics, chemical kinetics, and numerical methods for calculating important parameters in fluid dynamics. Chapter 2 also contains a review on the theoretical background of combustion phenomena, oxy-fuel combustion, importance of ethylene as a fuel, and experimental and numerical trends in combustion research. Chapter 3 focuses on numerical characterization of premixed ethylene-oxygen combustion, focusing on a computationally efficient method within a two-dimensional domain, with a background-methods-results format. Chapter 4 includes research presented in the same manner as Chapter 3 but examines non-premixed ethylene-oxygen flames. The focus of Chapter 4 is to model and evaluate oxygen index impact on soot production and the resulting radiative heat transfer effects. Chapter 5 summarizes the research in this study and presents final conclusions. The final chapter discusses the potential for future ethylene-oxygen combustion research derived from this study.

CHAPTER II

THEORETICAL BACKGROUND & LITERATURE REVIEW

This chapter details the background theory used in this study and reviews the current experimental and numerical literature regarding combustion of ethylene. The first portion of this chapter will focus on the general process of combustion of hydrocarbons in both fuel-air and oxy-fuel systems, before proceeding into a detailed discussion on calculation of combustion flow field properties. The remaining portions of this chapter are devoted to a discussion of the specifics of ethylene combustion, along with an overview of the current trends in experimental and numerical combustion research.

Combustion Theory

A combustion reaction is a oxidation/reduction reaction in which a fuel species is rapidly oxidized and produces gaseous species, and large quantities of heat energy [7]. A general reaction equation for the combustion of a hydrocarbon in pure oxygen is

$$C_xH_y + \left(x + \frac{y}{4}\right)O_2 \rightarrow xCO_2 + \left(\frac{y}{2}\right)H_2O$$

where x and y refer to the number of carbon and hydrogen atoms in the hydrocarbon molecule respectively. In this case, the generic hydrocarbon is oxidized by diatomic oxygen to produce carbon dioxide and water vapor. Combustion of a generic hydrocarbon in air follows the same process but includes nitrogen as a non-reacting species in a molar ratio to oxygen of approximately 3.76 to 1. The amount of heat energy produced by a combustion reaction is determined by calculating change in enthalpy (ΔH) as the reaction progresses from reactants to products.

$$\Delta H_{rxn} = \sum n\Delta H_{f,Products} - \sum m\Delta H_{f,Reactants}$$

In the above equation, the coefficients n and m refer to stoichiometric amounts of each reactant or product species, and ΔH_f is the heat of formation of chemical species that is usually determined at standard temperature and pressure. The heat that is released in a combustion reaction is the major contributor to the flame temperature, and the temperature rise associated with a combustion reaction can be determined using heat capacity values for the products of the reaction. Since enthalpy is a function of temperature and pressure, $H = H(T, P)$, then

$$dH = \left(\frac{\partial H}{\partial T}\right)_P dT + \left(\frac{\partial H}{\partial P}\right)_T dP$$

and

$$C_P \overset{\text{def}}{=} \left(\frac{\partial H}{\partial T}\right)_P$$

where C_p is the heat capacity at constant pressure. At constant pressure conditions, the temperature change associated with the reaction can be calculated from the heat of reaction:

$$\Delta H = \int_{T_o}^{T_f} C_P dT$$

In this equation, T_o refers to the initial temperature (usually 298 K) and T_f refers to the final flame temperature. If all the heat produced by the reaction is assumed to stay within the system and contribute fully to raising the temperature of the products of the reaction, then T_f is the adiabatic flame temperature (AFT). This is the theoretical maximum temperature of a flame produced in a particular combustion reaction. Actual flame temperatures vary from

AFT due to incomplete combustion, fuel lean or rich mixtures, dissociation reactions, and other competing reactions such as the water gas shift. Since heat capacity is also a function of temperature, $C_p = C_p(T)$, the calculation of flame temperature can be accomplished by assuming constant heat capacities or by iteration using various polynomial equations for heat capacity as a function of temperature [1, 7-9]. Adiabatic flame temperatures for oxy-fuel combustion are higher than the corresponding fuel-air combustion process. The presence of large quantities of nitrogen from the air provides an additional species to absorb heat energy released by the reaction, thus lowering the flame temperature.

Oxy-fuel combustion offers several advantages over conventional fuel-air combustion. In oxy-fuel combustion, nitrogen is removed from the oxidizer stream in an air separation unit (ASU) so that a high concentration of oxygen enters the combustion chamber along with the fuel stream. Upon combustion, the water is condensed and separated from the flue gas resulting in a high concentration of carbon dioxide in the remaining flue gas. Some of the flue gas is recycled to the oxidizer stream to increase conversion and to lower the flame temperature in the combustion chamber. A general schematic of an oxy-fuel combustion process [10] is shown in Figure 2.1.

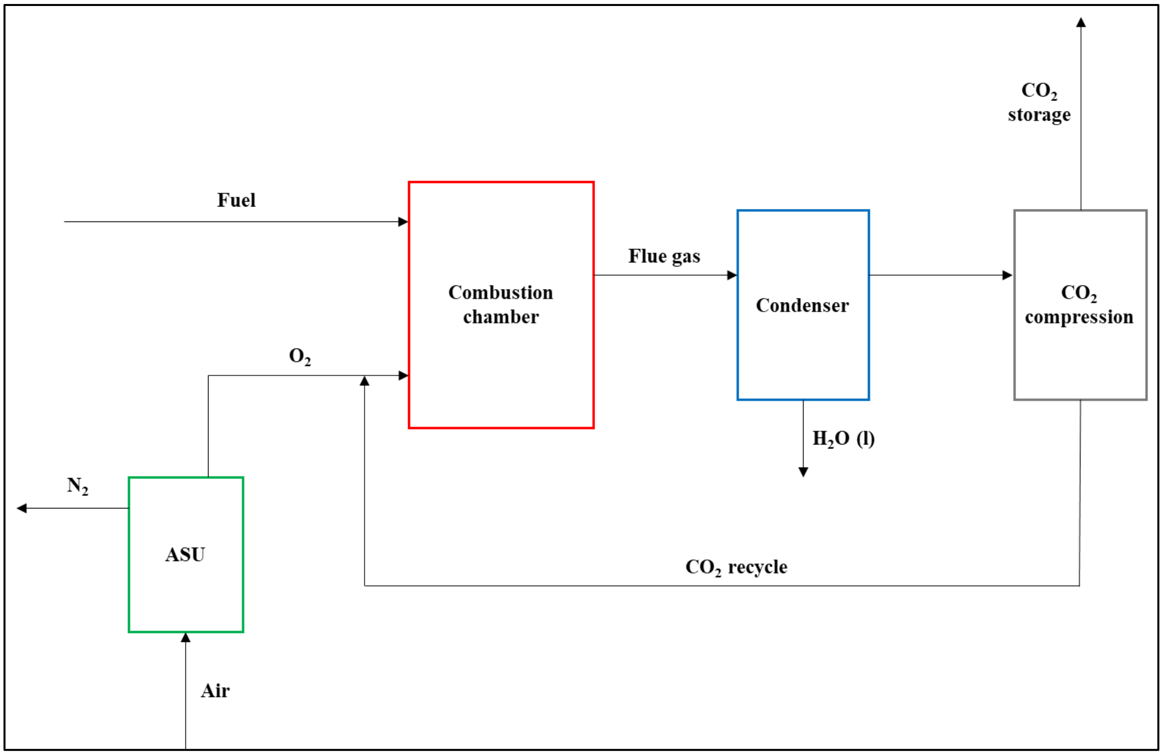

Figure 2.1. General schematic for a typical oxy-fuel combustion process.

The removal of nitrogen from the combustion process results in the elimination of NOx products, a significant concern for management of environmentally hazardous emissions [1]. Additionally, the CO_2 capture process is much easier than in conventional fuel-air combustion since the concentration of CO_2 in the product stream is much higher in oxy-fuel combustion. A major drawback of oxy-fuel combustion is the requirement for an air separation unit. The separation of oxygen from air is energy intensive, and often leads to efficiency losses that are economically unattractive. Likewise, the recycle of flue gases back to the oxidizer stream, although lowering and acting as a control on flame temperatures, introduces increased radiative heat transfer due to the presence of additional CO_2 and water vapor [1].

The calculation of flow field properties in a combustion system involves accounting for mass, momentum, energy, and species conservation within the system domain. The differential form of the governing equations are [11-13]:

$$\frac{\partial \rho}{\partial t} + \nabla \cdot \left(\rho \vec{V}\right) = 0$$

$$\frac{\partial (\rho u)}{\partial t} + \nabla \cdot \left(\rho u \vec{V}\right) = -\frac{\partial p}{\partial x} + \frac{\partial \tau_{xx}}{\partial x} + \frac{\partial \tau_{yx}}{\partial y} + \frac{\partial \tau_{zx}}{\partial z} + \rho g_x$$

$$\frac{\partial (\rho v)}{\partial t} + \nabla \cdot \left(\rho v \vec{V}\right) = -\frac{\partial p}{\partial y} + \frac{\partial \tau_{xy}}{\partial x} + \frac{\partial \tau_{yy}}{\partial y} + \frac{\partial \tau_{zy}}{\partial z} + \rho g_y$$

$$\frac{\partial (\rho w)}{\partial t} + \nabla \cdot \left(\rho w \vec{V}\right) = -\frac{\partial p}{\partial z} + \frac{\partial \tau_{xz}}{\partial x} + \frac{\partial \tau_{yz}}{\partial y} + \frac{\partial \tau_{zz}}{\partial z} + \rho g_z$$

$$\frac{\partial (\rho E)}{\partial t} + \nabla \cdot \left(\rho E \vec{V}\right) = -\nabla \cdot \vec{q} - \nabla \cdot \left(\rho \vec{V}\right) + \dot{Q} + \rho \vec{g} \cdot \vec{V}$$

$$\frac{\partial (\rho Y_i)}{\partial t} + \nabla \cdot \left(\rho Y_i \vec{V}\right) = \omega_i + \nabla \cdot (\Gamma_i \nabla Y_i)$$

where the first equation is the conservation of total mass, the second, third, and fourth equations are the conservation of momentum in the x, y, and z-directions, the fifth equation is the conservation of energy, and the last equation is the conservation of chemical species. Taken together, these governing equations constitute the full three-dimensional, compressible Navier-Stokes equations with chemical reactions. There are six dependent variables of interest in the governing equations: pressure (p), temperature (T), density (ρ), and the three components of the velocity vector (u, v, w). Temperature is accounted for in the energy conservation equation through the heat flux vector (q) and total energy (E). Additional terms in the Navier-Stokes equations are the body force terms (g), mass fraction (Y_i), reaction source term (ω_i), and diffusion coefficient (Γ_i) for species i, the stress tensor terms (τ_{ij}), and heat generation term (Q) due to viscous forces or radiative heat transfer in the fluid. A full listing of all notation used can be found in Appendix A.

To close the set of governing equations, an appropriate equation of state is needed to relate density, temperature, and pressure. The ideal gas law is often used for convenience:

$$p = \rho RT$$

where R is the specific gas constant. Additionally, the reaction source term (ω_i) is defined as a change in concentration for a particular species, based on a rate constant (k) and the order of the reaction. Determination of the rate constant for a reaction is based on Arrhenius kinetics [7, 14]

$$k = AT^n e^{-E_a/RT}$$

where E_a is the activation energy, and the values A, T, n, and E_a are determined experimentally for a particular reaction. The Navier-Stokes equations, along with the equation of state, and chemical kinetics information forms a set of coupled equations that must be solved simultaneously to determine flow field properties [11, 12]. This is a challenging task that is aided by the power of computers and forms the basis for the computational fluid dynamics (CFD) field of study. Specific CFD approaches applied to combustion systems will be discussed later in this chapter.

Ethylene as a Combustion Fuel

Initial research into combustion phenomena focused on the study of hydrogen or light hydrocarbon (methane) combustion due to the relative simplicity of reaction mechanisms. As the body of published research on these fuels increased, a natural progression toward examination of more complex fuels occurred. The interest in ethylene combustion has increased over the past decade due to several factors. Ethylene, the simplest olefin, is produced in higher quantities than other organic compounds and is heavily used as a feedstock for large scale production of other organic compounds [3, 4, 15, 16]. The use of ethylene in production processes often requires storing and transporting the gas under high pressures and/or temperatures. This poses an obvious safety concern [5]. Ethylene has also been considered for use as potential fuel, either as a transition fuel from hydrogen to hydrocarbon systems, or as a fuel in its own right [4, 6, 17-19]. The development of pulse detonation engine technology has also increased interest in ethylene as a fuel since it is extremely flammable, has a relatively high molecular weight compared to other gaseous hydrocarbon fuels, has stable detonation characteristics, and can be ignited on a hot surface without the requirement for a spark [4-6]. Additional chemical and physical properties of ethylene can be found in Appendix B.

Flame temperatures resulting from ethylene combustion depend on the equivalence ratio (Φ) of ethylene to oxidizer and the composition of the oxidizer. Adiabatic flame temperatures for stoichiometric ($\Phi = 1$) ethylene combustion in air are around 2370 K and are tabulated in the literature [1, 20]. Tabulated adiabatic flame temperatures for ethylene combustion in oxygen are hard to find but can be calculated using by assuming constant heat capacities of product gases or by using polynomial models for heat capacity as a function of temperature. The Shomate equation [9, 21]

$$C_P = A + Bt + Ct^2 + Dt^3 + \frac{E}{t^2}$$

can be used to determine constant pressure heat capacities as functions of temperature where *t* is the temperature per 1000 K and the variables *A*-*E* are tabulated curve-fit coefficients. Several other models exist [7, 8] that include more or fewer curve-fit coefficients. This can lead to large differences in calculated adiabatic flame temperatures depending on the method and source used to calculate heat capacities. Additionally, if constant volume heat capacities are used as in the case of combustion in a closed vessel, then the isochoric flame temperature is calculated in an analogous way to adiabatic flame temperature using constant volume heat capacity values [22]. Adiabatic and isochoric flame temperature values for ethylene combustion with several different oxidizer mixtures can be found in Appendix B.

Chemical reaction kinetics information is also diverse for a particular fuel/oxidizer combination. Reaction mechanisms provide the required kinetics information needed to determine rates of formation or consumption of a species during a reaction. Development and testing of reaction mechanisms ranging from several hundred elementary reaction steps [23, 24] to global one-step mechanisms is an active area of research. Many of the reaction mechanisms that have been proposed for ethylene combustion are derived from larger detailed mechanisms and validated numerically against experimentally observed ignition delay times and laminar flame velocities [5, 15, 18, 19, 25, 26]. Often, proposed mechanisms are developed for different ranges of pressure, temperature, or equivalence ratio, and have limited ranges of applicability.

Another area in which ethylene differs from other light hydrocarbon fuels is in radiative heat transfer. Carbon dioxide and water vapor are gases that emit radiation at high temperatures [27-29], but it is the production of soot particles during ethylene combustion that has been shown to have an significant impact on flame characteristics [30-32]. Radiative heat transfer can have a significant effect on overall heat transfer, and can have complex angular and spectral variations within a combustion system [33]. In the interest of computational efficiency, one method used to determine radiative emission from CO_2 and H_2O produced in ethylene combustion is through the equation [34, 35]

$$\dot{Q} = 4\sigma(T^4 - T_b^4)\sum_i (p_i a_i)$$

where Q is the radiative heat flux, σ is the Stefan-Boltzmann constant, T is the local gas temperature, T_b is the surrounding gas temperature, p_i is the partial pressure of gas species i, and a_i is the Planck mean absorption coefficient. Planck mean absorption coefficients for CO_2 and H_2O as functions of temperature are found in the literature [34].

Interest in ethylene combustion also centers around soot production during combustion. Ethylene is a soot-producing fuel because it readily oxidizes to acetylene, a major precursor of soot formation [36]. Soot particles produced during combustion of ethylene decrease flame temperatures through radiative heat transfer to the walls of combustion chambers and presents an obvious concern for environmental air quality and health effects [37]. The radiative heat transfer resulting from soot can adversely affect furnace wall lifetimes due to increased heat loading, but may decrease NOx production when ethylene is burned in air due to lower flame temperatures [30].

Experimental Trends in Flame Characterization

The experimental results found in the literature pertaining to ethylene combustion depend upon the type of combustion system studied. Premixed systems involve ethylene and the oxidizer initially well mixed in a combustion chamber at a predetermined equivalence ratio prior to ignition. Non-premixed systems, or diffusion systems, involve separate streams of ethylene and air flowing into a combustion chamber simultaneously and mixing during the process of combustion. Flame properties of interest in these studies are also different depending on the combustion system studied.

Premixed combustion system studies often attempt to characterize flame temperature, flame velocity, and manner of flame propagation. Usually, experiments are conducted in small tubes or channels so that multidimensional effects can be simplified. An example experimental setup is shown in Figure 2.2 [38].

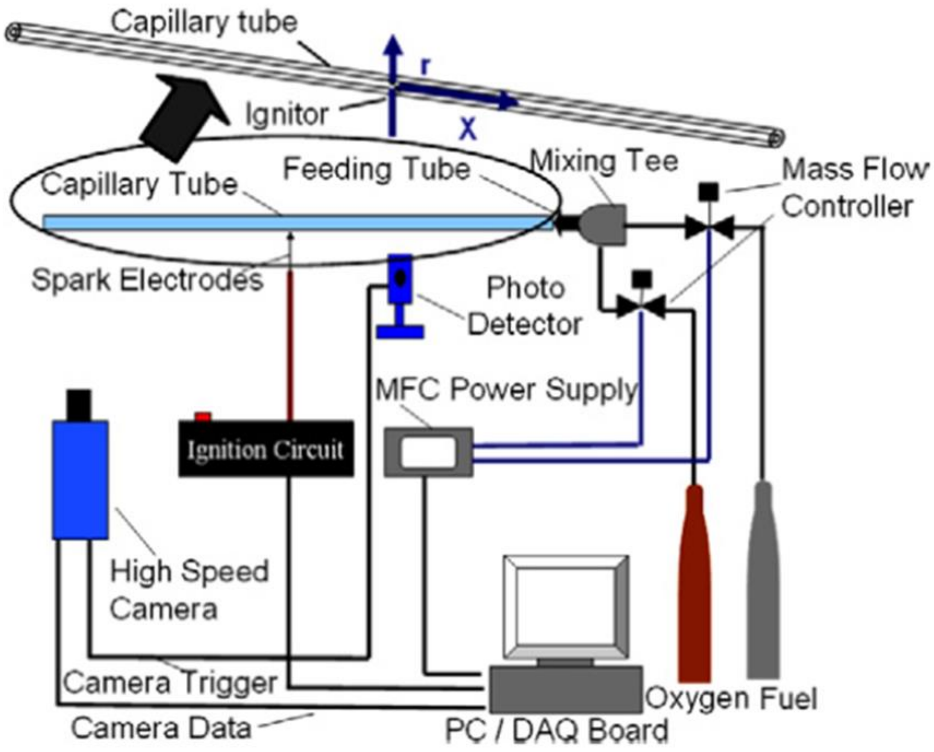

Figure 2.2. Example experimental setup for study of premixed combustion phenomena [38]. Reprinted from [38] with permission from Elsevier.

In these experimental studies, flame locations within the combustion chamber as a function of time are measured with high speed cameras. The objective of many experimental studies in premixed ethylene-air or ethylene-oxygen systems is to measure flame velocity and characterize the mode of flame propagation from the ignition source of the combustion to an open end at some distance away from the ignition. These flame velocities and modes of propagation can vary significantly, from subsonic deflagration processes to supersonic detonation processes. Often, a propagating flame front will begin as a deflagration and transition to a detonation in a process called deflagration-to-detonation transition (DDT).

The process of DDT, including the relative importance of contributing mechanisms behind the phenomenon, is an active area of research aimed at controlling accidental explosions and in potential uses of controlled detonation such as pulse detonation engines [39-42]. Although most researchers in DDT phenomena do not necessarily agree on the relative importance of the possible contributing factors that initiate transition from deflagration to detonation, they generally agree on the basic steps that occur in a DDT event [4, 39, 41, 43-49]. First, the ignition flame accelerates at an exponential rate, which stretches the flame and produces shock waves far ahead of the flame front. Second, the flame acceleration decreases and compression waves are formed directly ahead of the flame front, generating a small zone of preheated reactant gases. A compressed pocked of unburned reactant gas mixture is heated in this zone and begins to react, which produces a large pressure gradient. This increase in pressure enhances further reaction and generates a coupling between the heat released by reaction and the increase in pressure. Finally, the pressure gradient grows quickly into a strong shock wave and a transition to detonation occurs somewhere between the leading shock and the flame front. A qualitative plot of scaled flame velocity as a function of time for the process just described is shown in Figure 2.3 [49].

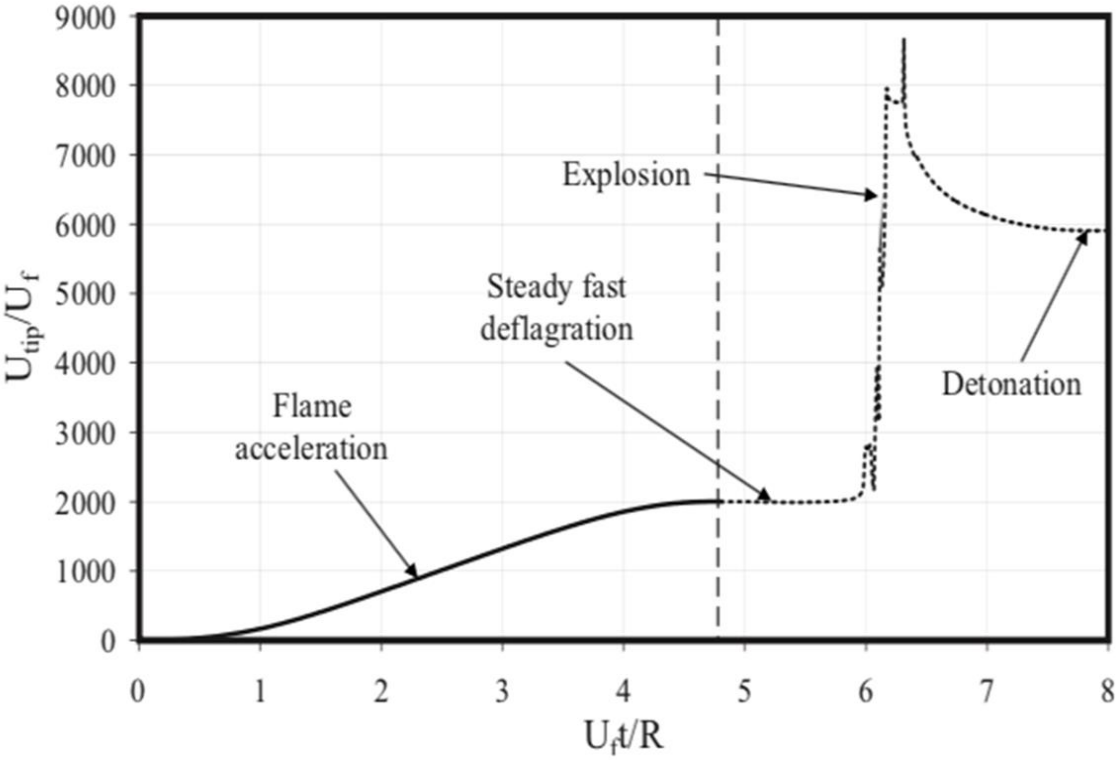

Figure 2.3. Generalized scaled flame tip velocity for a hydrocarbon fuel as a function of time for an initially laminar flame [49]. Reprinted from [49] with permission from the American Physical Society.

Commonly studied factors in DDT phenomena are turbulence, transport effects, flame-shock interactions, combustion chamber geometry, equivalence ratio, and reaction kinetics [39, 40, 43, 50]. The most common method for experimental study of DDT phenomena is through the use of shock tubes, as represented in Figure 2.2.

In experimental studies of non-premixed systems, a setup similar to that of premixed systems is used. In non-premixed systems, however, the fuel and oxidizer are fed into the combustion chamber simultaneously while combustion is occurring. The fuel and oxidizer feed can be either co-flow or counter-flow in application. In the combustion chamber, the fuel and oxidizer mix through convection and diffusion and a region of stoichiometric ratio is established. It is in this region of stoichiometric ratio where the combustion reaction occurs, and the flame resides. Figure 2.4 shows a typical non-premixed experimental setup [32].

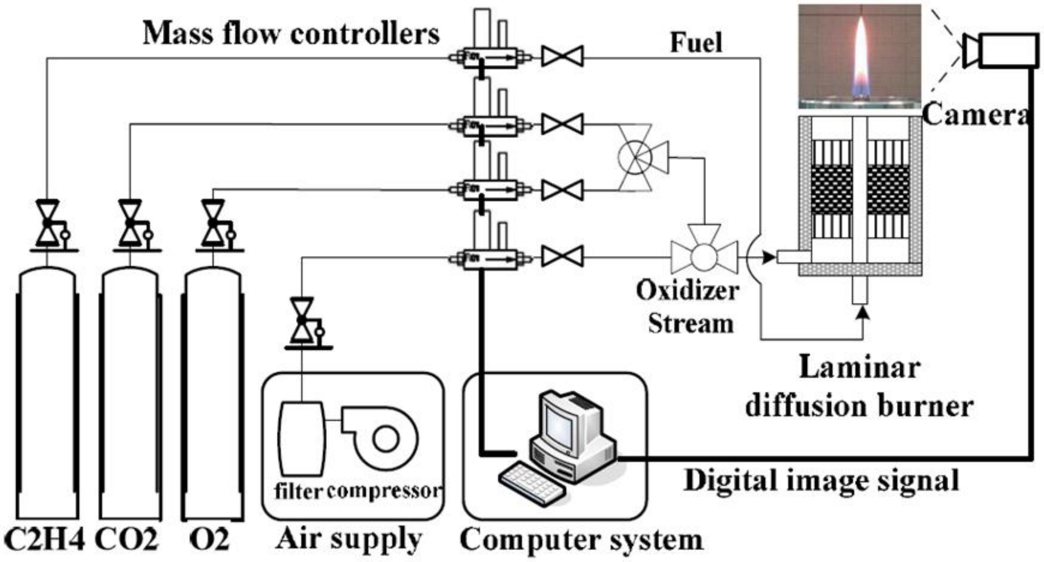

Figure 2.4. Typical experimental setup for study of non-premixed combustion systems [32]. Reprinted from [32] with permission from the American Chemical Society.

Experimental studies in non-premixed systems typically measure flame characteristics such as flame height, flame temperature, and laminar flame velocity under varying conditions of fuel/oxidizer composition, mass flow rates, system pressure, and turbulence. With fuels such as ethylene, experiments detailing soot formation and subsequent radiative heat transfer effects are often conducted [32, 37, 51-57]. Soot formation in non-premixed flames contributes to increased heat exchange within the internal surfaces of industrial furnaces [30, 31] but also contributes to pollution and health hazards [53, 56-59] making it an active area of combustion research.

Although the description of various experimental processes in premixed and non-premixed combustion research are rather generalized, detailed discussions of research that forms the experimental bases for this study follows in Chapter 3 for premixed combustion and Chapter 4 for non-premixed combustion.

CFD Approaches to Combustion Research

In contrast to the experimental setups described in the previous section, researchers have increasingly relied on numerical methods to describe combustion phenomena due to significant increases in computing power over the past few decades. The computing power increases are so significant that a numerical researcher referring to a simulation of a DDT process in 1996 wrote, "the fastest way to do the calculation would be to wait 20 years until computers were much bigger and faster [39]." Today, powerful CFD software is available through open-source and commercial providers that offers the ability to calculate complex reactive flow properties with a relatively low computational cost.

The basic operation of a CFD code is generally the same regardless of the source or software used. CFD codes apply the Navier-Stokes equations to a user-defined computational domain and apply numerical methods to arrive at a calculated solution for the flow properties. These numerical methods may be as simple as Euler's method or as complex as high order Runge-Kutta or finite difference methods [60]. Several research groups have used methods appropriate to the type of combustion problem they were studying; WENO (weighted, essentially non-oscillatory) schemes are useful in convection-dominated problems with sharp discontinuities [61] and MUSCL (monotonic upwind scheme for conservation laws) have been routinely used [4, 45, 62-65]. The CFD code ANSYS Fluent [66] used in this study utilizes a control volume approach to convert the mass, momentum, or energy conservation portions of the Navier-Stokes equations into algebraic equations that can be solved numerically [12, 67, 68]. An integral-form representation of the governing transport equation for a scalar quantity ϕ is:

$$\int_V \frac{\partial \rho\phi}{\partial t} dV + \oint \rho\phi\vec{v}d\vec{A} = \oint \Gamma_\phi \nabla\phi d\vec{A} + \int_V S_\phi dV$$

where *A* is the surface area vector, S_ϕ is a source term for the scalar quantity, and all other terms in the equation retain their definition from the original Navier-Stokes equation shown previously. The concept of discretization allows the replacement of a partial differential equation or set of partial differential equations that are applied to a continuum domain with an exact solution, such as the Navier-Stokes equations, by a set of equations that approximate the solution in a discrete domain [12]. Once the governing equation is discretized to a control volume, the resulting equation is [67]:

$$\frac{\partial \rho \phi}{\partial t} V + \sum_{f}^{N_f} \rho_f \vec{v}_f \phi_f \vec{A}_f = \sum_{f}^{N_f} \Gamma_\phi \nabla_\phi \vec{A}_f + S_\phi V$$

where the subscript *f* denotes the value of a parameter at a face of the control volume, and N_f is the number of faces that constitute the control volume. This discretized version of the governing equation is used to solve for the scalar quantity at the center of each control volume that makes up the entire computational domain.

The solution to the governing equations that have been spatially and temporally discretized can follow several methods. The values for the gradients and face values of the scalar quantity are based on values assigned or previously calculated at control volume centers. As an example, the face values of the scalar quantity (ϕ_f) in the convective term of the discretized equation use a solver scheme called “upwind.” In the upwind scheme, the face values are derived from control volume quantities located upstream from the face with respect to the velocity vector [67]. In a first-order upwind scheme, the value at the control volume face is assumed to be equal to the value at the center of the control volume that is located directly upstream of the face. Higher-order upwind schemes exist that use different assumptions to determine the relationship between face values and center values of the upstream control volume [67].

Temporal discretization follows a relatively simple process. Each of the scalar quantities in the governing equation is integrated over a small time interval (Δt). The time dependency of a scalar quantity can be expressed as a function of the quantity at some future time

$$\frac{\partial \phi}{\partial t} = F(\phi^{n+1})$$

such that

$$\frac{\phi^{n+1} - \phi^{n}}{\Delta t} = F(\phi^{n+1})$$

$$\phi^{n+1} = \phi^{n} + \Delta t F(\phi^{n+1})$$

where $F(\phi^{n+1})$ incorporates values obtained from spatial discretization, ϕ^{n} is the value of the scalar quantity at time n, and ϕ^{n+1} is the value of the quantity at some future time [67]. This equation call be solved iteratively within each time interval before advancing to the subsequent time interval. The spatial and temporal discretization approaches described here address the determination of the scalar quantity ϕ in the governing equations, but do not provide a means to determine gradients of the quantity ($\nabla\phi$). These values can be calculated with methods such as Green-Gauss or least squares methods [67].

Numerical calculations of combustion phenomena inherently involve chemically reacting species, which are accounted for in source terms applied to the governing equations regarding conservation of species mass. To adequately compute source term values in the discretized governing equation, appropriate chemical kinetics information must be supplied to the solver for all chemically reacting species. In the most basic form, a one-step chemical reaction can be represented by [1, 67, 69]:

$$\sum_{j=1}^{n} v_j' M_j \rightleftharpoons \sum_{j=1}^{n} v_j'' M_j$$

where M_j refers to a chemical species with a total number of n species, and the v' and v'' refer to stoichiometric coefficients of the reactant and product species with index j respectively. The change in concentration of a chemical species i over time due to a reaction is referred to as the reaction rate for that species and is given by [1, 14, 67]:

$$\frac{d[M_i]}{dt} = Rate = (v_i'' - v_i')\left(k_f \prod_{j=1}^{n} [M_j]^{v_j'} - k_r \prod_{j=1}^{n} [M_j]^{v_j''}\right)$$

where $[M_i]$ refers to the molar concentration of species i and k_f and k_r refer to the forward and reverse reaction rate constants respectively. The rate constants are calculated through the Arrhenius rate equation discussed earlier, and the total source term applied to the governing equation is dependent upon the molar mass of each species, the total number of reactions applied (N), and the individual reaction rates of species i for all reactions [67]. The source term (S) is calculated as the sum of the reaction rates of all species participating in all reactions:

$$S = \mathcal{M}_i \sum_{r=1}^{N} R_{i,r}$$

The number of reactions used in a combustion reaction mechanism can vary widely from several-hundred elementary reaction steps to one-step global reaction mechanisms. In the literature involving ethylene combustion, large detailed mechanisms such as the Gas Research Institute mechanism (GRI-Mech) or the mechanisms published by USC and UCSD

[24, 70] can be found which involve as many as 325 individual reactions. Mechanisms such as these can contribute to significant increases in computational expense and may include reactions for individual species that are unimportant or not included in the system under examination. At the opposite end of the spectrum, global one-step reaction mechanisms cut down on computational cost but may produce results that are not in good agreement with experiment, or neglect individual chemical species of interest [17]. An example of a global one-step reaction mechanism for ethylene combustion is

$$C_2H_4(g) + 3O_2(g) \longrightarrow 2CO_2(g) + 2H_2O(g)$$

where the equivalence ratio is unity. As a reasonable alternative to detailed or global reaction mechanisms, reduced reaction mechanisms can be found or developed that capture the important species and reactions of interest to a combustion scenario, while neglecting unimportant aspects. These reduced reaction mechanisms are often derived from detailed mechanisms and compared against experimental and numerical observations of laminar flame speed and ignition delay time [5, 15, 18, 19, 25, 26, 71]. The versatility of computational fluid dynamics is apparent when dealing with complex chemistry aspects. The ability to easily modify the reaction source term in the governing equations through the use or modification of a selected chemical reaction mechanism allows close examination of chemistry effects in the overall process.

Source term inclusion is not limited to chemical reaction aspects; heat transfer effects may also be included or modified through source terms in the energy conservation equation. Radiative heat transfer by emission from hot gases such as carbon dioxide or water vapor, or by the presence of soot particles, can affect flame temperatures and flame velocities. Common practices within CFD studies of combustion processes include the use of P-1 or discrete ordinates radiation models [29, 35, 72] to solve for the radiative transfer equation (RTE). A wavelength-independent form of the RTE accounting for absorption, scattering, and emission along a path (s) can be written as [67]

$$\frac{dI(\vec{r},\vec{s})}{ds}+(a+\sigma_s)I(\vec{r},\vec{s})=an^2\frac{\sigma T^4}{\pi}+\frac{\sigma_s}{4\pi}\int_0^{4\pi} I(\vec{r},\vec{s})\Phi(\vec{s}\cdot\vec{s}')d\Omega'$$

where the first term on the left-hand side of the RTE is the change in radiative energy within a medium along the path. The second term deals with radiant energy losses due to absorption and scattering within the medium. The right-hand side of the RTE deals with energy gains due to emission from other sources (first term) and scattering from other sources (second term) external to the medium. In each numerical model used to solve the RTE, several coefficients relating to absorption, scattering, or emission within the medium must be specified. Determination of these values can be accomplished via means such as Planck mean absorption coefficients [28, 34, 35] or the weighted-sum-of-gray-gases model [67, 73]. Although radiative effects are commonly considered in numerical studies of non-premixed ethylene combustion systems, they are routinely neglected in studies of premixed systems.

Computational fluid dynamics approaches specific to this study of premixed and non-premixed oxy-ethylene combustion are discussed in greater detail in the following chapters.

CHAPTER III

NUMERICAL INVESTIGATIONS OF LEAN, PREMIXED ETHYLENE-OXYGEN FLAME PROPAGATION AND THERMAL LOSSES IN SMALL TUBES WITH A REDUCED CHEMICAL REACTION MECHANISM

Abstract

Heat loss plays an important role on the flame propagation characteristics of premixed gas mixtures in small tubes. However, stringent spatial and temporal resolutions required to simulate these phenomena cause numerical investigations to resort to single-step global reaction mechanisms and ignore radiative losses. Both these restrictions are relaxed in this study where a reduced 10-step mechanism and an optically thin radiation model are employed to study flame propagation in lean ($\Phi = 0.2$) premixed ethylene-oxygen mixtures in millimeter-scale tubes (1 mm and 2 mm diameters). First, convergence in the spatial and temporal resolutions were ascertained and found to compare well with the characteristic reaction zone lengths and timescales determined from detailed reaction mechanisms. The accumulation of numerical errors over the simulation time frame was determined to be less than 0.06%. Radiative losses reduced the flame propagation velocities by 73% and 51% in the 1 mm diameter and 2 mm diameter tubes respectively and made the flames less concave. The flame velocities were moderately affected by the thermal boundary conditions (adiabatic versus isothermal walls). The radiant fractions were in the range 0.12 – 0.17. The slow CO oxidation reactions cause CO_2 concentrations to be lower than those predicted from single-step mechanisms.

Background

Combustion research into premixed and non-premixed ethylene-oxygen and ethylene-air systems has been steady over the past several years. The interest in ethylene combustion research stems largely from its attractiveness as a fuel, either on its own, or as a transitional fuel from hydrogen fuel systems to hydrocarbon systems [4-6, 17-19]. Ethylene is ubiquitous in the chemical processing industry; it is an intermediate product in the combustion of heavier hydrocarbons and it is a raw material for several other important industrial chemical processes [4, 15-19].

While there are several well-established experimental studies on ethylene combustion, the continual development and increase in computational capacity has allowed additional insight using numerical techniques coupled with computational fluid dynamics approaches. The focus of this chapter is to model premixed ethylene-oxygen combustion and flame characteristics in millimeter-scale tubes using a chemical reaction mechanism that has not been previously used for premixed combustion systems. This mechanism, developed by Lovas *et al.* [74] is a 10-step, 11-species compact mechanism that was originally developed for modeling soot production in ethylene-oxygen diffusion flames. The study described in this chapter applies that mechanism to a premixed ethylene-oxygen combustion scenario and validates its use through comparison of flame characteristics generated by the simulation to previously published experimental results.

Other researchers have used several different reaction mechanisms in similar numerical studies of ethylene-oxygen or ethylene-air premixed combustion leading to transitions from deflagration to detonation (DDT). Several have used simple, one-step global mechanisms [6, 16, 40, 45-47, 50, 65, 75] where the impact of chemical kinetics was thought to be of relatively little importance. Others have used more detailed mechanisms for hydrogen combustion scenarios [42, 44, 63, 64, 76] and sparingly for premixed ethylene combustion scenarios [5, 71, 77] to determine the impact of chemistry-turbulence interactions in the nature of flame propagation. Although single-step reaction mechanisms provide decreased computational cost, they likely come with tradeoffs in accuracy. Sensitivity analyses between various detailed mechanisms are in general agreement on the importance of the initial ethylene reaction with oxygen and the hydroxy radical/hydrogen radical oxidation reaction [15, 18]. The importance of these elementary reaction is neglected in one-step global reaction mechanisms. Table 3.1 provides a summary of the types of reaction mechanisms used by other authors in recent combustion simulation literature.

Table 3.1. Reaction mechanisms used in recent combustion studies; References [4-6, 40, 42, 45-47, 50, 63-65, 71, 74-77].

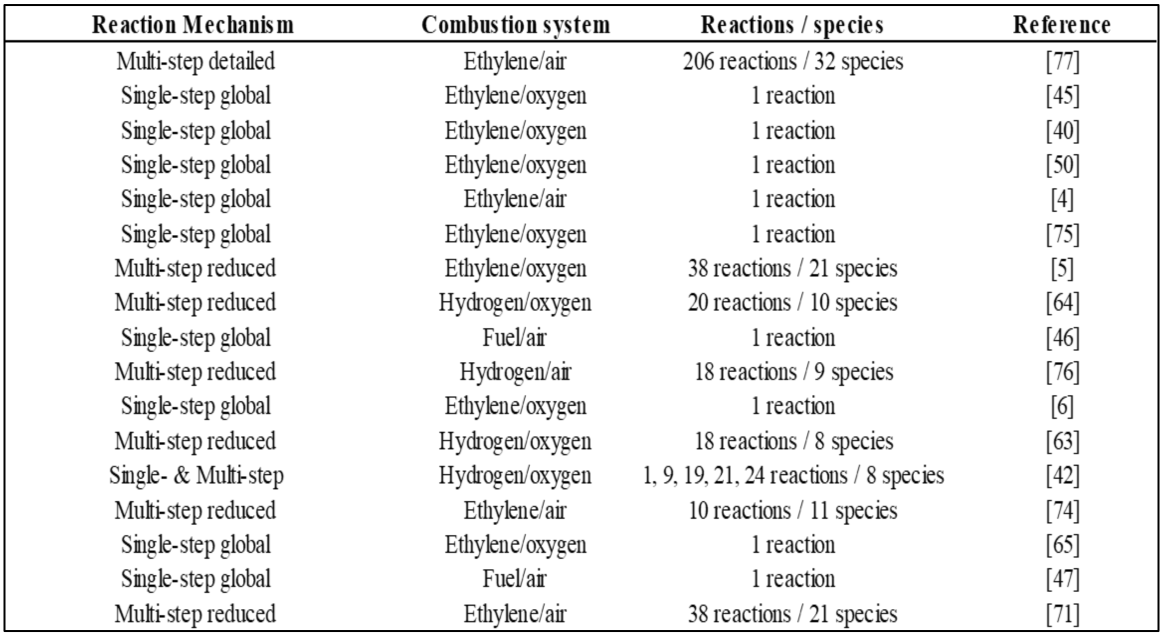

Reaction Mechanism	Combustion system	Reactions / species	Reference
Multi-step detailed	Ethylene/air	206 reactions / 32 species	[77]
Single-step global	Ethylene/oxygen	1 reaction	[45]
Single-step global	Ethylene/oxygen	1 reaction	[40]
Single-step global	Ethylene/oxygen	1 reaction	[50]
Single-step global	Ethylene/air	1 reaction	[4]
Single-step global	Ethylene/oxygen	1 reaction	[75]
Multi-step reduced	Ethylene/oxygen	38 reactions / 21 species	[5]
Multi-step reduced	Hydrogen/oxygen	20 reactions / 10 species	[64]
Single-step global	Fuel/air	1 reaction	[46]
Multi-step reduced	Hydrogen/air	18 reactions / 9 species	[76]
Single-step global	Ethylene/oxygen	1 reaction	[6]
Multi-step reduced	Hydrogen/oxygen	18 reactions / 8 species	[63]
Single- & Multi-step	Hydrogen/oxygen	1, 9, 19, 21, 24 reactions / 8 species	[42]
Multi-step reduced	Ethylene/air	10 reactions / 11 species	[74]
Single-step global	Ethylene/oxygen	1 reaction	[65]
Single-step global	Fuel/air	1 reaction	[47]
Multi-step reduced	Ethylene/air	38 reactions / 21 species	[71]

Another aspect of research into flame propagation in premixed systems is the selection of wall boundary conditions. There does not appear to be a consistent application or discussion of wall boundary conditions with respect to heat transfer effects throughout the experimental or numerical research literature. In the purely experimental literature, heat transfer at the walls is not usually discussed beyond specifying the material that comprises the wall [38, 41, 78, 79]. In studies that feature both experimental and numerical analyses, wall boundary conditions assigned in the numerical setup either follow an adiabatic/isothermal approach [80] or attempt to model heat transfer using physical properties of the materials used in the experiment [29]. A notable departure from this trend are the studies published by Martua *et al.* [81] and Brambilla *et al.* [82] that used varying wall temperatures along the path of flame propagation in both experimental and numerical setups. They observed different modes of flame propagation corresponding to different wall temperatures; higher wall temperatures resulted in steady flame propagation, while lower wall temperatures resulted in oscillatory propagation of flames that would extinguish and re-ignite repetitively [81, 82]. These results were also seen in an earlier numerical study of acetylene-air flame acceleration reported by Ott *et al.* in 2003 [83]. In the purely numerical research, the trend is to either select adiabatic or isothermal wall boundary conditions, but is inconsistent in reporting impacts of the choice of boundary condition [35]. Several DDT studies of hydrogen-oxygen systems noted that detonation onset occurred in different locations in the combustion chamber depending on the specified wall boundary condition. [63, 64, 84]. Other studies address heat transfer effects due to wall boundary conditions explicitly [35, 85]. Table 3.2 summarizes recent experimental and numerical research with varying wall boundary conditions and different fuel/oxidizer components in premixed combustion systems.

Table 3.2. Thermal boundary conditions used in experimental and numerical studies of various fuel/oxidizer mixtures; References [29, 35, 38, 41, 63, 64, 78-85].

Study type	Fuel/oxidizer system	Thermal BC	Reference
Experimental	Oxy-ethylene	Quartz-walled tube	[38, 41]
Experimental	Oxy-ethylene	Aluminum wall	[79]
Experimental	Oxy-ethylene	Aluminum alloy & quartz chamber	[78]
Experimental & numerical	Methane/air	Varying wall temperature (300 K - 1320 K) along the long axis of tube by external heat source	[81]
Experimental & numerical	Syngas/air	Numerically specified wall temps (550-1320 K) based on thermocouple measurements from experiment	[82]
Experimental & numerical	Oxy-methane	Experimental: stainless steel chamber; Numerical: assigned emissivity values based on stainless steel properties	[29]
Experimental & numerical	Methane/air & hydrogen/air	Experimental: quartz-walled chamber; Numerical: isothermal & adiabatic conditions	[80]
Numerical	Acetylene/air	Isothermal & adiabatic	[83]
Numerical	Hydrogen/oxygen	Isothermal & adiabatic	[63]
Numerical	Hydrogen/oxygen	Adiabatic	[84]
Numerical	Hydrogen/oxygen	Isothermal & adiabatic	[64]
Numerical	Oxy-methane	Isothermal	[85]
Numerical	Hydrogen/air	Isothermal & adiabatic	[35]

Much of the current research regarding ethylene combustion focuses on understanding the underlying processes by which the fuel/oxidizer mixture progresses from ignition, through flame acceleration, to full detonation. The remainder of this chapter focuses on the initial flame acceleration and steady deflagration phase of lean ($\Phi = 0.2$) ethylene-oxygen mixtures, and the ability of the chosen reaction mechanism to produce reasonably accurate results when compared to experimental data. Various aspects of heat transfer, wall boundary conditions, and variation in initialization conditions are also examined.

Numerical Methods

The computational fluid dynamics package, ANSYS Fluent (version 19.1) was used to model laminar flame propagation in ethylene-oxygen systems. The CFD solver uses a control volume technique to discretize a general transport governing equation [67]. The general transport equation is the same as was discussed in Chapter 2,

$$\int_V \frac{\partial \rho \phi}{\partial t} dV + \oint \rho \phi \vec{v} d\vec{A} = \oint \Gamma_\phi \nabla \phi d\vec{A} + \int_V S_\phi dV$$

where ϕ is the scalar quantity based on the governing transport equations of mass, momentum, or energy conservation; ρ is density, Γ_ϕ is a diffusion coefficient for ϕ, S_ϕ is a source term for ϕ, and $\vec{u}$ and $\vec{A}$ are velocity and surface area vectors, respectively. The governing equations use multi-dimensional and transient terms, with compressibility, chemical reactions, and radiative heat transfer also included. ANSYS Fluent has several features that make it an appropriate program to study combustion processes; simulations can be executed in multiple dimensions while turbulent flow, complex chemistry, and transport phenomena can be modeled simultaneously. Additionally, post processing of results can be executed within the program without exporting to another interface or software package.

In this study, the two-dimensional simulation of premixed ethylene-oxygen combustion focused on flame propagation during the deflagration phase of the process, prior to any transition to detonation. The modeling options invoked for the majority of the calculations are shown in Table 3.3.

Table 3.3. Modeling options used in calculations of premixed combustion in small diameter tubes.

Physical Model	**CFD Model**
Turbulence	None; laminar flow
Thermodynamic & transport properties	Kinetic theory of gases
Chemistry	Finite-rate with 10-step mechanism
Radiative heat transfer	User-defined source function based on Planck mean absorption coefficients
Solver and discretization schemes	Pressure-based solver with QUICK scheme for spatial discretization and first-order implicit time-stepping scheme
Ignition cell initialization	Initial temperature based on adiabatic flame temperature for lean ethylene/oxygen mixtures; constant pressure combustion
Equation of State	Soave-Redlich-Kwong (SRK)
Boundary conditions	Isothermal (T = 300 K)

When radiation effects were examined, user-defined functions based on either a Planck-mean or weighted-sum-of-gray-gas (WSGG) approach to determining absorption coefficients of CO_2 and H_2O were used. The radiative flux resulting from the emission of radiation from these gases was incorporated as a separate source term in the energy conservation equation. Laminar flow was used in all simulations, and the source term for species conservation was taken directly from the species production/consumption rates derived from the overall reaction mechanism. The QUICK scheme was used as the spatial discretization scheme due to its applicability when distinct upstream and downstream cells on structured meshes are present. This scheme blends a second-order upwind scheme with a central interpolation and tends to be more accurate with meshes aligned with the direction of fluid flow [67]. A first-order implicit temporal discretization scheme was used due to its inherent stability with respect to time step size.

Simulations were conducted in lean mixtures within tubes of either 1 mm or 2 mm diameter. The major products of combustion were artificially patched into one computational cell at elevated temperature and atmospheric pressure. Table 3.4 shows the initialization conditions used for the simulations in this chapter.

Table 3.4. Initialization values for premixed combustion simulations.

Parameter	Initialization Value(s)
Domain pressure	101325 Pa
Domain temperature	300 K
Unburned fuel mixture (mass fraction)	$C_2H_4 = 0.055$ $O_2 = 0.945$ (Fuel Lean, $\Phi = 0.2$)
Combustion product composition (mass fraction)	$H_2O = 0.5$ $CO_2 = 0.5$
Combustion product pressure	101325 Pa
Combustion product temperature	2000 K

Computational Domain

The computational domain was modeled after experiments conducted by Wu *et al.* [38, 41] to provide direct comparison between experimental and numerical results. In the computational domain used for this study, a plenum chamber was incorporated at the open end of the tube to mitigate the effect of outlet pressure waves on the flame stability and propagation within the tube. The domain schematic is shown in Figure 3.1 (a). The domain was meshed with 125,000 – 200,000 cells depending on the intended mesh resolution. The domain was also scaled in the y-direction to conduct simulations in both 1 mm and 2 mm tubes. The direction of flow in the domain was from left to right, as shown in Figure 3.1 (b), and the boundaries were treated isothermally at 300 K.

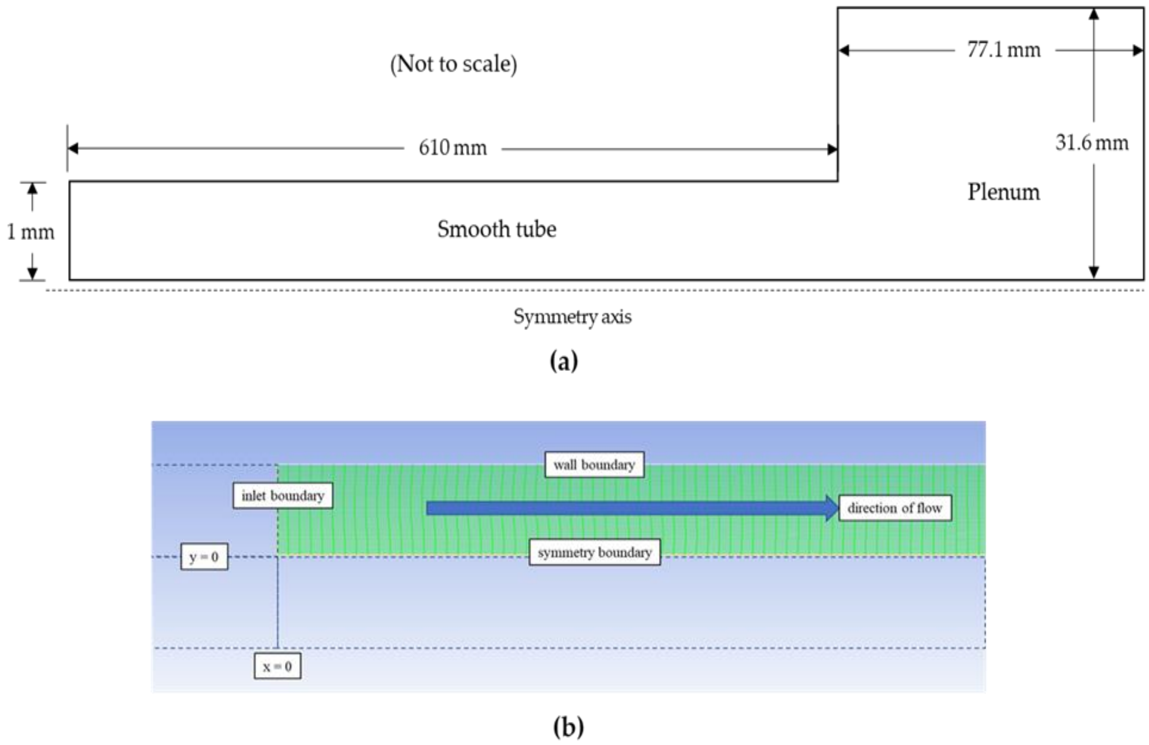

Figure 3.1. Computational domain schematic: (a) general dimensions with plenum chamber; (b) meshed region indicating direction of flow and several boundaries.

Reaction Mechanism

The choice of reaction mechanism can have a significant impact on the accuracy of calculation in simulations of combustion processes. Detailed mechanisms with several hundred or thousands of elementary reaction steps provide clarity in kinetic aspects but incur a heavy computational cost. Global one- or two-step mechanisms increase computational speed but often provide results that are not in good agreement with experiment [17]. Reduced mechanisms, derived from detailed mechanisms, can provide reasonable accuracy and computational speed by neglecting those unimportant reactions of those short-lived species contained in the detailed mechanism.

There are several examples in the literature of reduced mechanisms being proposed and compared against established detailed mechanisms [5, 15, 18, 19, 25, 26] such as the Gas

Research Institute (GRI), University of Southern California (USC), University of California San Diego (UCSD), Saudi Aramco, and Lawrence Livermore National Laboratory (LLNL) mechanisms. The usual criteria of comparison are ignition delay time and laminar flame speed. Reduced mechanisms that compare well with the detailed mechanisms using these criteria are considered valid.

The reaction mechanisms used in this study is a reduced 10-step global mechanism proposed by Lovas *et al.* in 2010 [74]. This mechanism was derived from a previous 10-step mechanism proposed by Singh and Jachimowski [17] with slight changes to hydroxyl radical consumption and the addition of acetylene formation/consumption steps. Table 3.5 shows the complete 10-step reaction mechanism used in this study along with reaction rate parameters.

Table 3.5. 10-step reaction mechanism [74] used for study of premixed ethylene-oxygen combustion.

Reaction	A	n	E_a
I. $O_2 + C_2H_4 \leftrightarrow 2CO + 2H_2$	7.800×10^{23}	0.000	35500.00
II. $O + CO + M \leftrightarrow CO_2 + M$	5.300×10^{13}	0.000	-4540.00
III. $OH + CO \leftrightarrow H + CO_2$	4.400×10^{6}	1.500	-740.00
IV. $O_2 + H_2 \leftrightarrow OH + OH$	1.700×10^{20}	0.000	48000.00
V. $O_2 + H \leftrightarrow OH + O$	2.600×10^{14}	0.000	16800.00
VI. $OH + H_2 \leftrightarrow H + H_2O$	2.200×10^{17}	0.000	5150.00
VII. $O + H_2 + M \leftrightarrow H_2O + M$	1.100×10^{20}	-2.000	0.00
VIII. $2H + M \leftrightarrow H_2 + M$	2.400×10^{19}	-1.000	0.00
IX. $C_2H_4 \leftrightarrow C_2H_2 + H_2$	2.500×10^{12}	0.000	71530.00
X. $C_2H_2 + 2OH \leftrightarrow 2H_2 + 2CO$	5.380×10^{22}	0.000	14000.00

Notes: Units are in seconds, moles, cubic centimeters, calories, and degrees Kelvin
Third body efficiencies for H_2 = 2.5 and for H_2O = 16.0; 1.0 for all other species

The rate constants for the forward and reverse reactions are given by

$$k_{f,r} = AT^{n}exp\left(\frac{E_a}{RT}\right)$$

where A is the pre-exponential factor, T is the local temperature, n is a temperature exponent, E_a is the activation energy, and R is the universal gas constant. This mechanism was shown to agree well in predicting concentration profiles and flame temperatures with respect to several larger mechanisms ranging from 30 to 171 species in numerical simulations of non-premixed ethylene-oxygen flames [74].

This study is the first to use the mechanism proposed by Lovas *et al.* for simulation of premixed ethylene-oxygen flames. It is useful to validate proposed reaction mechanisms against experimental data reflecting conditions for which the mechanism was not originally considered [26] to determine its range of applicability.

Results & Discussion

Prior to direct comparison against experimental data, the numerical model was subjected to several preliminary tests to determine effects of initialization condition and method of discretization on the flame velocity and relative concentrations of combustion products. Additionally, the discretization error associated with obtaining a high-resolution computational mesh was quantified to characterize the accuracy of results.

Initialization Conditions Study

The of method of initialization was examined to determine the effect on flame velocity and mole fraction of CO_2 and H_2O. In a previous experimental study [41], ignition of the ethylene-oxygen mixture was accomplished by either a spark or a hot wire running perpendicular to the long axis of the combustion chamber. Small differences in flame acceleration were observed. In this study, the experimental methods of initiation were replicated by igniting the mixture within a small volume equivalent to one computational cell (replicating spark ignition) or the entire inlet boundary (replicating wire ignition). Initialization values assigned to the domain in either ignition case are shown in Table 3.4. This analysis was conducted on coarse and fine meshes with the ultimate result that the manner of initialization did not make a significant difference in flame velocity, flame temperature, or combustion product concentrations. Table 3.6 shows the flame properties for the simulations subject to different initialization conditions.

Table 3.6. Flame characteristics for various methods of simulation initialization.

Initialization condition	**Flame velocity (m/s)**	**Flame temperature (K)**	**CO_2 (mol frac)**	**H_2O (mol frac)**
Fine mesh (Δx = 0.122 mm) Boundary initialization	2.39	2503	0.02	0.12
Fine mesh (Δx = 0.122 mm) One-cell initialization	2.38	2507	0.02	0.12
Coarse mesh (Δx = 0.244 mm) Constant pressure conditions	1.39	2483	0.02	0.12
Coarse mesh (Δx = 0.244 mm) Constant volume conditions	1.42	2500	0.02	0.12

Spatial & Temporal Discretization

A grid convergence study was conducted to ensure that the spatial discretization scheme could resolve flame velocities and thicknesses that agree with experimental values. The initial cell size was set at 0.25 mm in the x-direction with variable length in the y-direction based on internal tube diameter. The basis for the initial cell size was taken from numerical data compiled by Shultz and Sheppard [86] where characteristic reaction zone lengths and times were computed for ethylene-oxygen systems at various equivalence ratios using different reaction mechanisms. The initial spatial refinements in this study were conducted with a refined mesh throughout the entire computational domain at cell sizes of 0.122 mm and 0.0610 mm in the x-direction. Additional simulations in which only the cells adjacent to the wall boundary were refined produced similar flame velocities as the refinement of the entire domain, while reducing computational load. Figures 3.2 and 3.3 show the resulting flame velocities and product gas mole fractions in the 1 mm tube as cell size decreases from 0.122 mm to 0.0153 mm in the x-direction. The change in flame velocity as the grid was refined from 0.0305 mm to 0.0153 mm was less than 3%, so the grid was considered converged at a spatial resolution of 0.0305 mm.

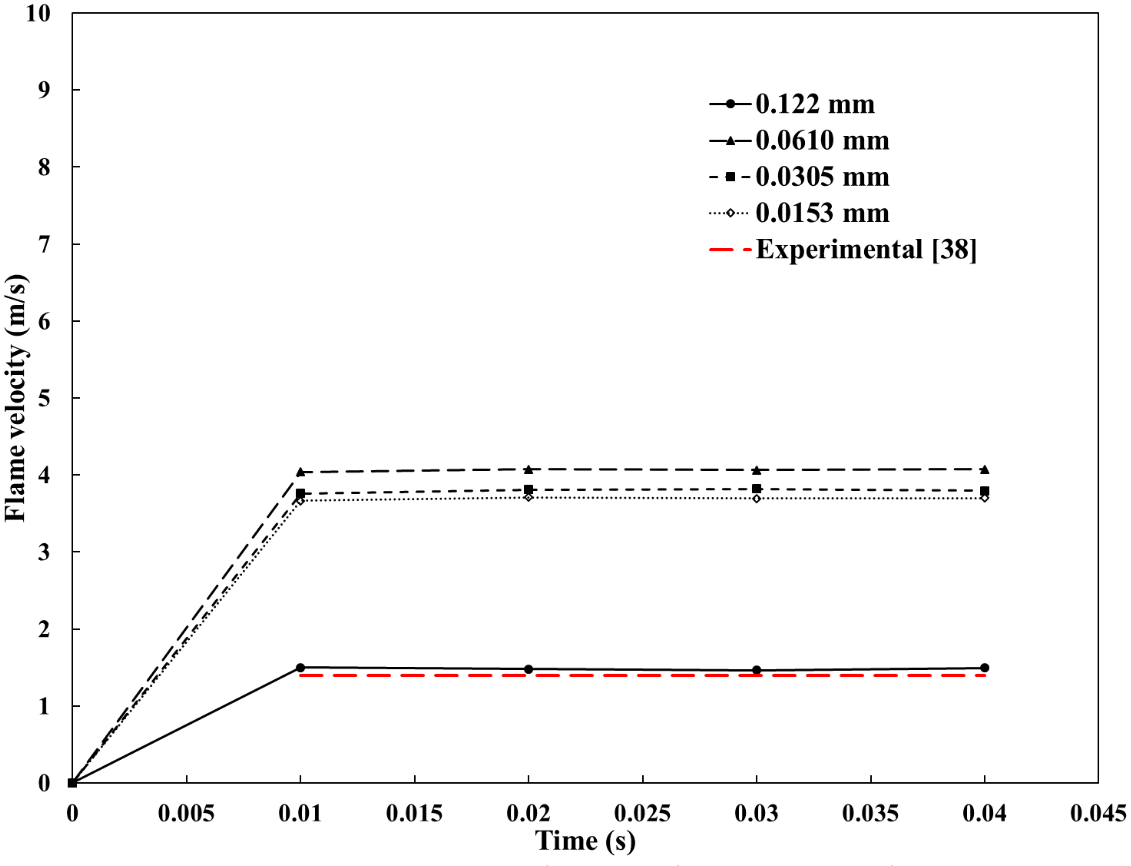

Figure 3.2. Flame velocities over time as a function of grid resolution for the 1 mm tube. Mesh refined in the boundary layer near the no-slip, isothermal wall. Experimental flame velocity [38] included for reference.

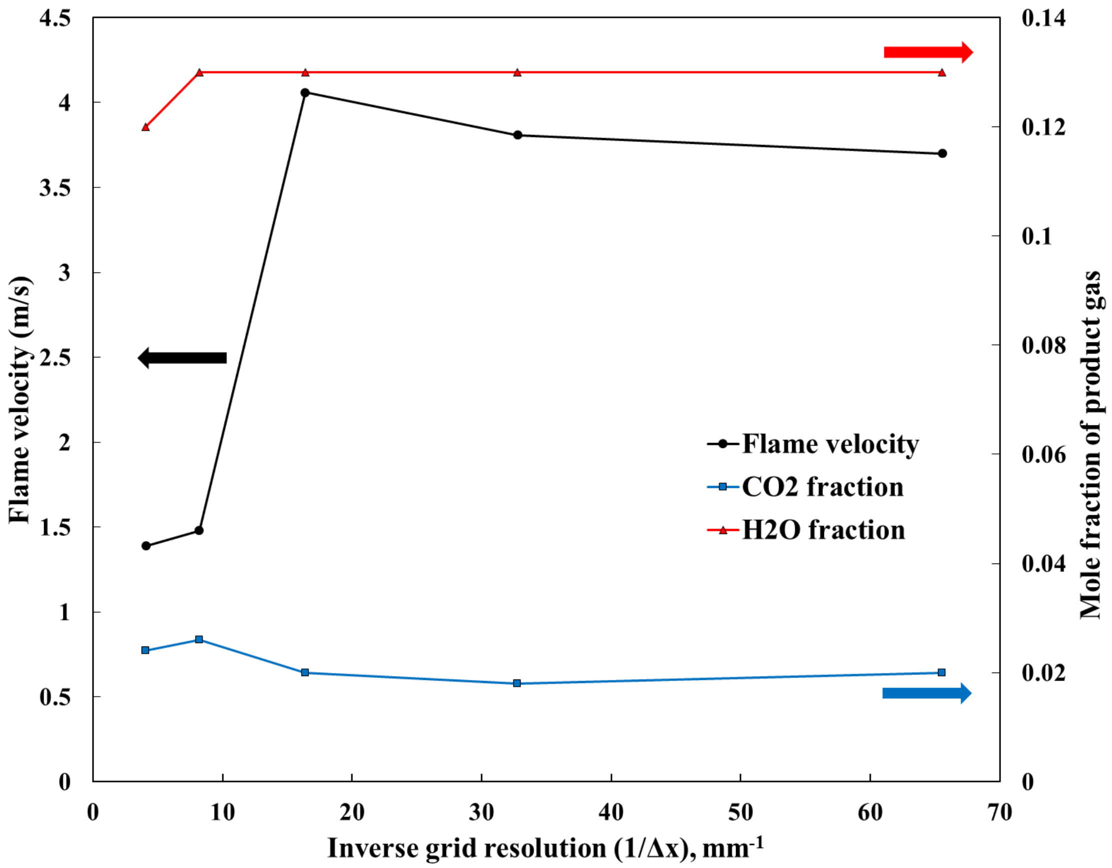

Figure 3.3. Flame velocity and mole fraction of CO_2 and H_2O as a function of inverse grid resolution in the 1 mm tube. Computation cell sizes decrease from left to right along the x-axis.

In a similar manner, a convergence study based on time step size was conducted. Data obtained from Schultz and Sheppard [86] indicated that the reaction time scales were on the order of microseconds. The time step convergence study used simulations with time step sizes of 10^{-5}, 10^{-6}, and 10^{-7} seconds. The flame velocities, flame temperatures, and mole fractions of combustion products were used to determine convergence. Figures 3.4 and 3.5 show the convergence of flame velocity and CO_2 mole fraction in 1 mm and 2 mm tubes. It is apparent that the flame velocities and mole fractions are relatively unchanged as the time step is reduced from 10^{-6} to 10^{-7} seconds. The average flame velocity values between these time step differed by 1.9% or less depending on the tube diameter, so the time step size was considered converged at 10^{-6} seconds, in agreement with published data.

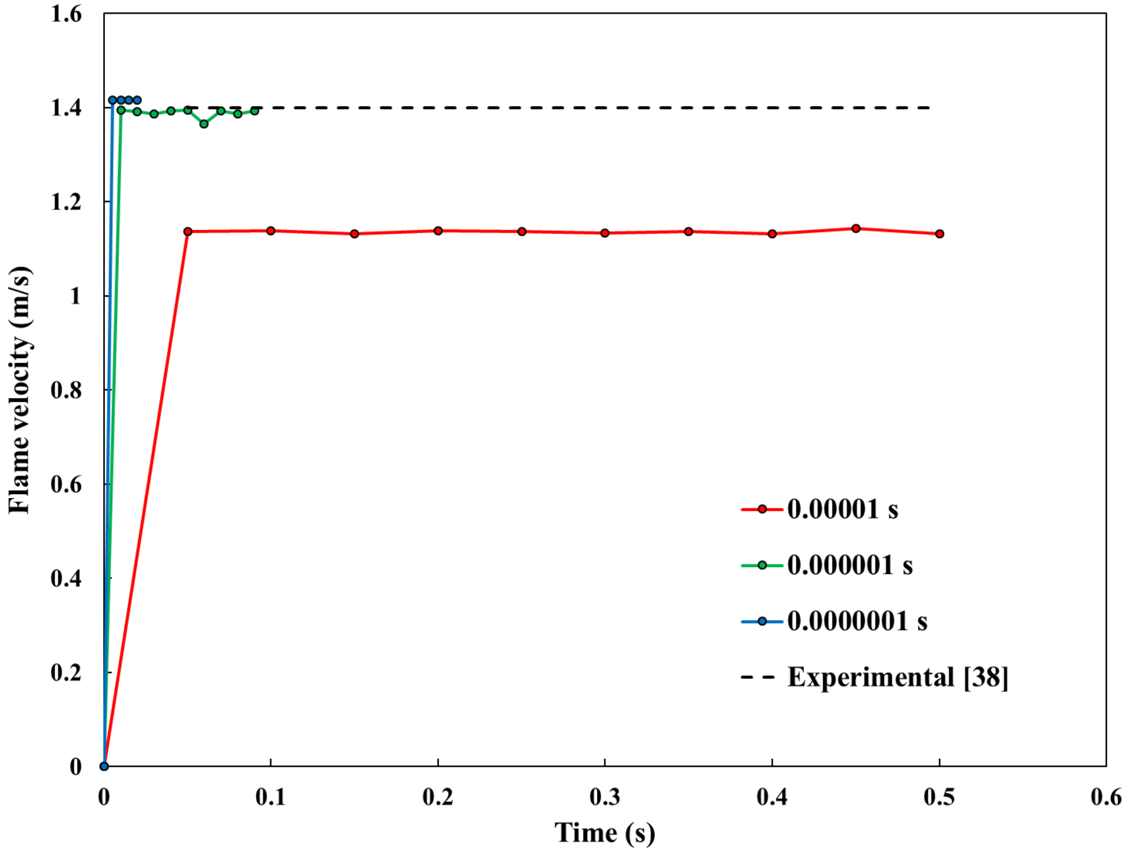

Figure 3.4. Time step convergence study in 1 mm tube reflecting differences in flame velocities for time step sizes ranging from 10^{-5} to 10^{-7} seconds.

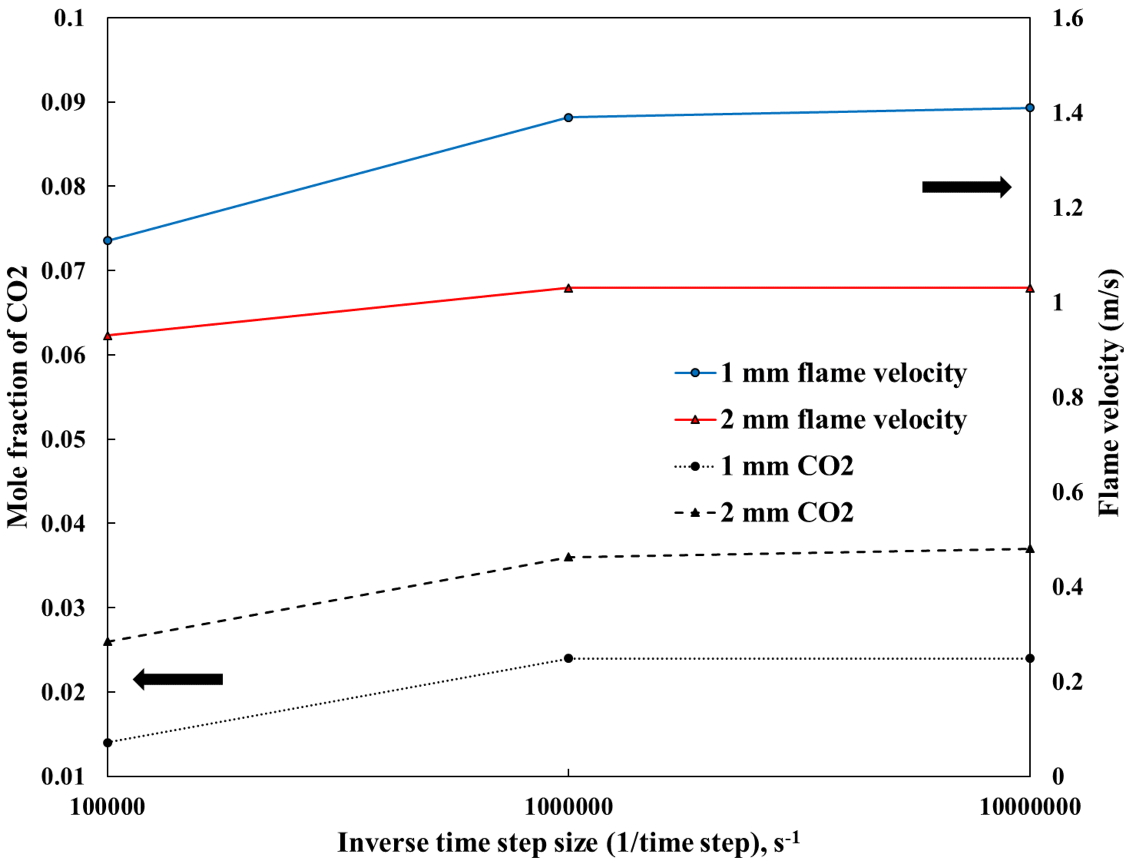

Figure 3.5. Flame velocities and mole fractions of CO_2 in 1 mm and 2 mm tubes as a function of inverse time step size. Time step size decreases from left to right along the x-axis.

Error Estimation Due to Discretization

As with any arbitrary division of a flow domain into a computational grid, integration error is introduced as the solver progresses from one computational cell into another. This error is a function of the grid resolution; higher grid resolution results in a smaller accumulated error but increased computational time. Alternatively, coarser grids result in lower computational time, but increased accumulated error and a lower limit on the total number of integration steps based on a desired upper limit of accumulated error.

In this study, a method for estimating the precision similar to that described by Smirnov *et al.* [87] was used to quantify error accumulation during spatial grid refinement. Table 3.7 shows the grid resolution in 2-D and the associated maximum number of time steps allowed based on a desired maximum error of 5%. The accumulated error shown in the table is based on 100000 time steps (at 1 microsecond per time step) for each of the grid resolutions shown, resulting in a total physical time of 0.1 seconds.

Table 3.7. Estimation of accumulated integration errors in simulations using different grid resolutions. The total number of time steps used with each mesh resolution was 100000.

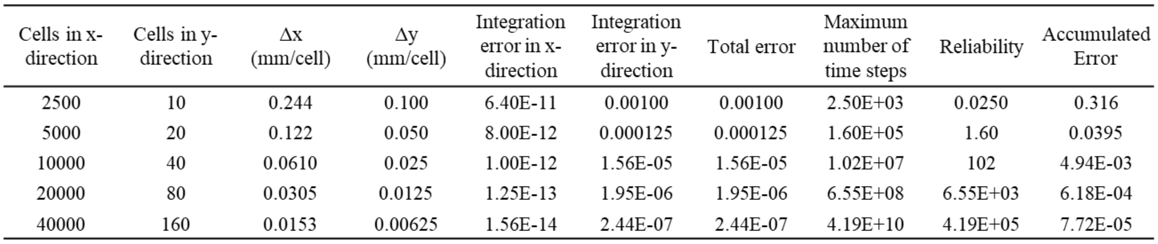

Cells in x-direction	Cells in y-direction	Δx (mm/cell)	Δy (mm/cell)	Integration error in x-direction	Integration error in y-direction	Total error	Maximum number of time steps	Reliability	Accumulated Error
2500	10	0.244	0.100	6.40E-11	0.00100	0.00100	2.50E+03	0.0250	0.316
5000	20	0.122	0.050	8.00E-12	0.000125	0.000125	1.60E+05	1.60	0.0395
10000	40	0.0610	0.025	1.00E-12	1.56E-05	1.56E-05	1.02E+07	102	4.94E-03
20000	80	0.0305	0.0125	1.25E-13	1.95E-06	1.95E-06	6.55E+08	6.55E+03	6.18E-04
40000	160	0.0153	0.00625	1.56E-14	2.44E-07	2.44E-07	4.19E+10	4.19E+05	7.72E-05

The estimates for integration error in each direction are based on the use of the QUICK solver scheme for spatial discretization. This scheme is based on a weighted average of second-order upwind and second-order central interpolation schemes [67]. The integration error is calculated for each spatial direction by

$$S_i = \left(\frac{1}{N_i}\right)^{k+1}$$

where S_i is the integration error with the index i indicating a specific spatial direction, N_i is the number of cells in the direction of integration, and k is the order of the spatial solver scheme. The total error (S_T) associated with a particular simulation is the sum of the integration errors in each of the dimensions used in the simulation. The maximum number of time steps is calculated by

$$n_{max} = \left(\frac{S_{max}}{S_T}\right)^2$$

where S_{max} is the maximum desired error, usually between 1% - 5%. Finally, the reliability (R_S) and accumulated error (S_{acc}) are calculated by

$$R_S = \frac{n_{max}}{n}$$

$$S_{acc} = S_T\sqrt{n}$$

where *n* is the total number of time steps used in the simulation. Larger values for reliability are better, as the number of time steps used is lower than the maximum number of time steps allowed to remain below the desired maximum error. With a desired error of less than 5%, only the coarsest mesh used in this study accumulated more error than was acceptable with simulations spanning 0.1 seconds. At the converged mesh resolution of 0.0305 mm per cell in the x-direction, the accumulated error was about 0.06%.

Tube Dimensions Study

Two different tube diameters were considered in this study, 1 mm and 2 mm. These were chosen to allow direct comparison to experimental data [38, 41]. Flame velocities and temperatures resulting from simulations in 1 mm and 2 mm tubes are shown in Figures 3.6 and 3.7. The flame velocities observed during experiment were 1 – 3 m/s in lean mixtures with equivalence ratios 0.18 – 0.4 [38].

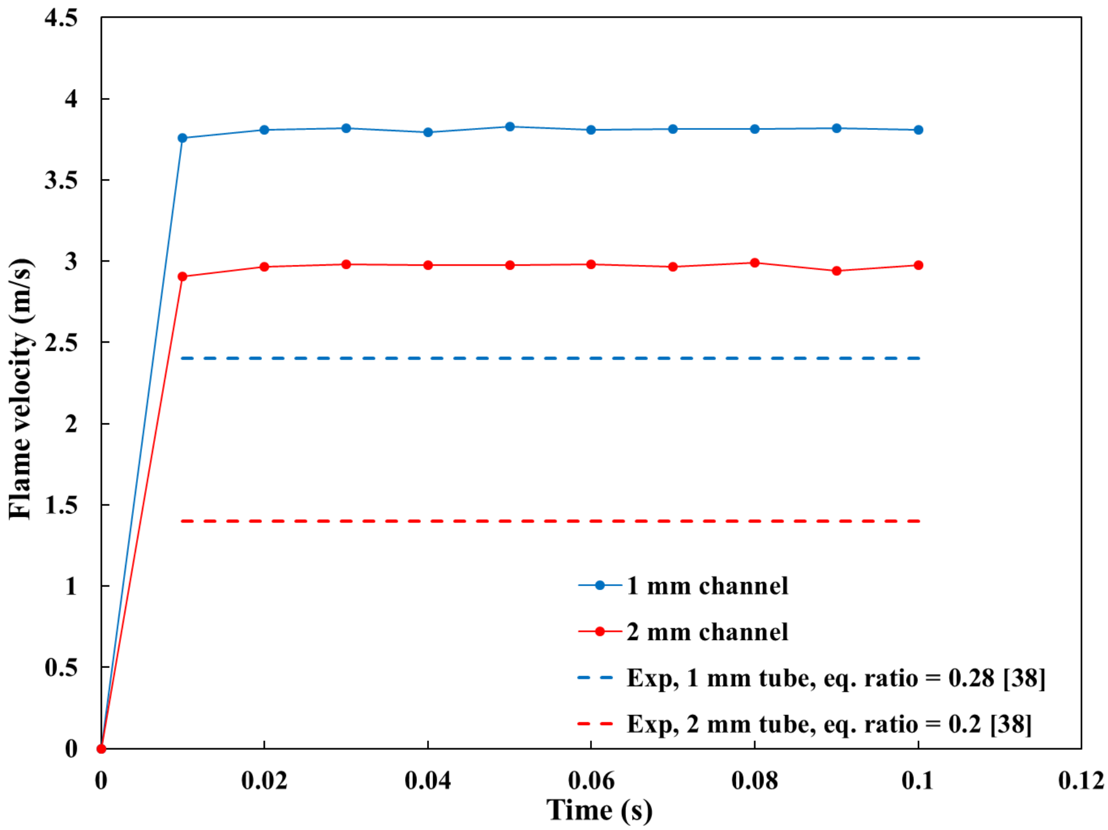

Figure 3.6. Flame velocity plots for 1 mm and 2 mm tubes. Experimental flame velocities [38] for both 1 mm and 2 mm tubes included as dashed lines.

Laminar flame speeds around 5.5 m/s were observed in experiments with stoichiometric (Φ = 1.0) ethylene-oxygen [41]. The average flame velocity in this study was 3.81 m/s for the 1 mm tube and 2.96 m/s for the 2 mm tube. These values are in reasonable agreement with experimental data, although efforts to reduce the differences are discussed in the following sections.

The flame temperature contours for the 1 mm and 2 mm tubes are shown in Figure 3.7. The flame temperature is slightly higher in the larger tube and compares well with calculated values of the adiabatic flame temperature for ethylene-oxygen at an equivalence ratio of 0.2.

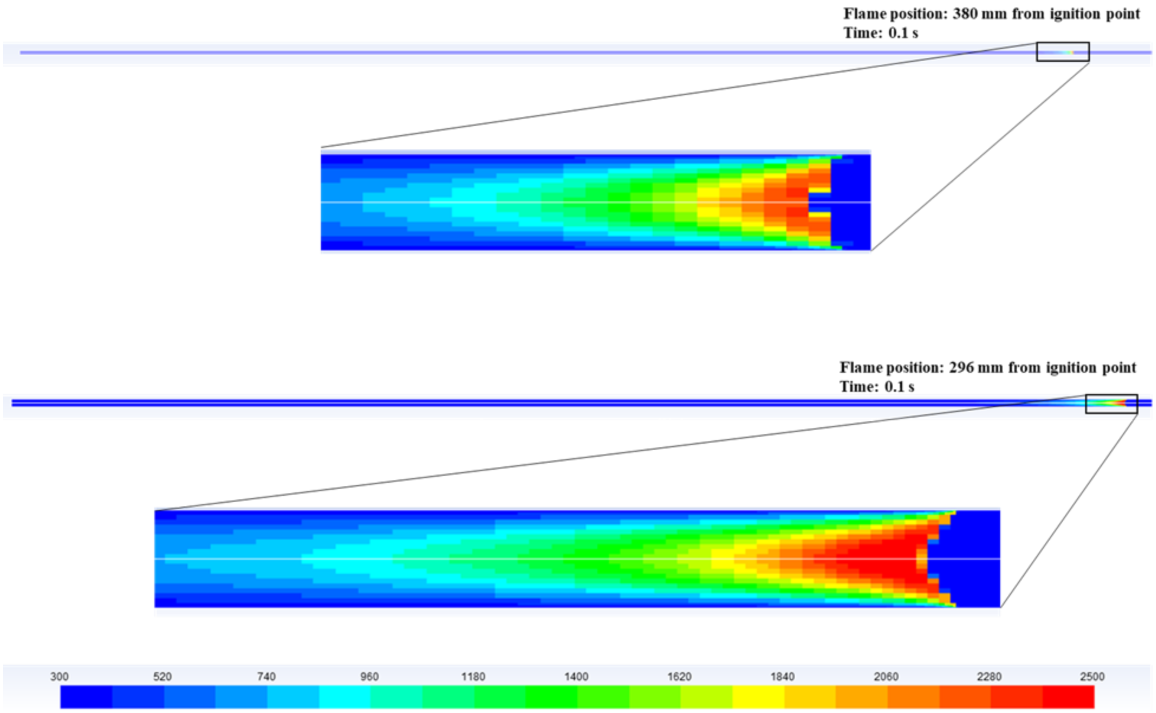

Figure 3.7. Flame temperature contours (K) for 1 mm and 2 mm tubes. Flow time is 0.1 seconds for both cases.

Radiation Effects

The effect of radiative heat loss during premixed combustion is an area that has not been extensively reported on. This study includes an examination of radiative heat loss during 1-D flame propagation using two different models, with the assumption that the transfer region between a fluid element and the unburned surroundings is optically thin. The radiation models were applied as user-defined functions in Fluent as additional terms in the energy conservation equation. The heat flux source terms were calculated using equations and curve fit parameters for absorption coefficients published by Barlow *et al.* [34, 88] for a Planck-mean approach, and by Krishnamoorthy [73] for a weighted-sum-of-gray-gas (WSGG) approach. The equations used to calculate the radiative flux arising from emission from high temperature CO_2 and H_2O are

$$\dot{Q} = 4\sigma(T^4 - T_b^4)\sum_i (p_i a_i)$$

for the Planck-mean approach and

$$\dot{Q} = 4\sigma\sum_j k_j w_j (T^4 - T_b^4)$$

for the WSGG approach. In these equations, Q is radiative heat loss per unit volume (W/m^3), σ is the Stefan-Boltzmann constant (5.669 x 10^{-8} W/m^2 K^4), T is local flame temperature (K), T_b is the background temperature (300 K), p_i is the partial pressure of species i (atm), and a_i is the Planck-mean absorption coefficient of species i (m^{-1} atm^{-1}). In the Planck-mean approach, the absorption coefficient was determined by

$$a_i = c_0 + c_1\left(\frac{1000}{T}\right) + c_2\left(\frac{1000}{T}\right)^2 + c_3\left(\frac{1000}{T}\right)^3 + c_4\left(\frac{1000}{T}\right)^4 + c_5\left(\frac{1000}{T}\right)^5$$

where the values polynomial coefficients are tabulated values found in the literature [34]. The Planck-mean approach uses species absorption coefficients that are functions of temperature only and are independent of incident radiation wavelength. In the WSGG approach, the absorption coefficient (k_j) was determined as a function of both temperature and five different wavelength bands (j), with weighting factors (w_j) specific to each band. The WSGG absorption coefficients were determined by

$$a_j = c_1 + c_2 T$$

where the curve fit coefficients and weighting factors were also found in the literature [73]. In this study, only the radiative effects of CO_2 and H_2O were considered, and the individual curve fit parameters used to calculate the absorption coefficients for the Planck-mean approach are shown in Table 3.8.

Table 3.8. Parameters used to calculate Planck-mean absorption coefficients for CO_2 and H_2O [34].

$$a_i = c_o + c_1(1000/T) + c_2(1000/T)^2 + c_3(1000/T)^3 + c_4(1000/T)^4 + c_5(1000/T)^5$$

	H_2O	CO_2
c_0	-0.23093	18.741
c_1	-1.12390	-121.310
c_2	9.41530	273.500
c_3	-2.99880	-194.050
c_4	0.51382	56.310
c_5	-1.86840×10^{-5}	-5.8169

Figure 3.8 shows the temperature-dependent Planck-mean absorption coefficients for CO_2 and H_2O as calculated by the curve fit polynomials. These polynomials are suitable for temperatures between the background temperature (300 K in this case) and 2500 K.

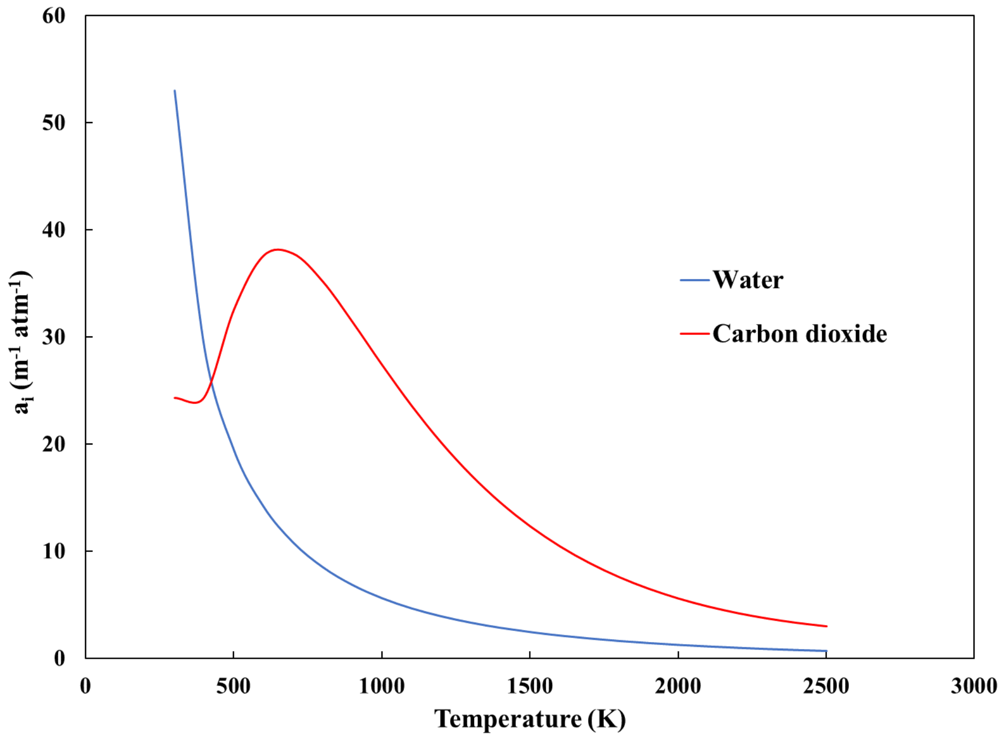

Figure 3.8. Planck-mean absorption coefficients for carbon dioxide and water vapor as calculated using equations and curve fit polynomials given by Barlow *et al.* [34].

The location of the flame in the 1 mm and 2 mm tubes along with temperature profiles for simulations conducted with and without the Planck-mean radiation model applied are shown in Figure 3.9. The radiative heat loss in these simulations result in lower flame temperatures and velocities. The larger-scale views in both portions of Figure 3.9 show the location of the flame front at a flow time of 0.1 seconds.

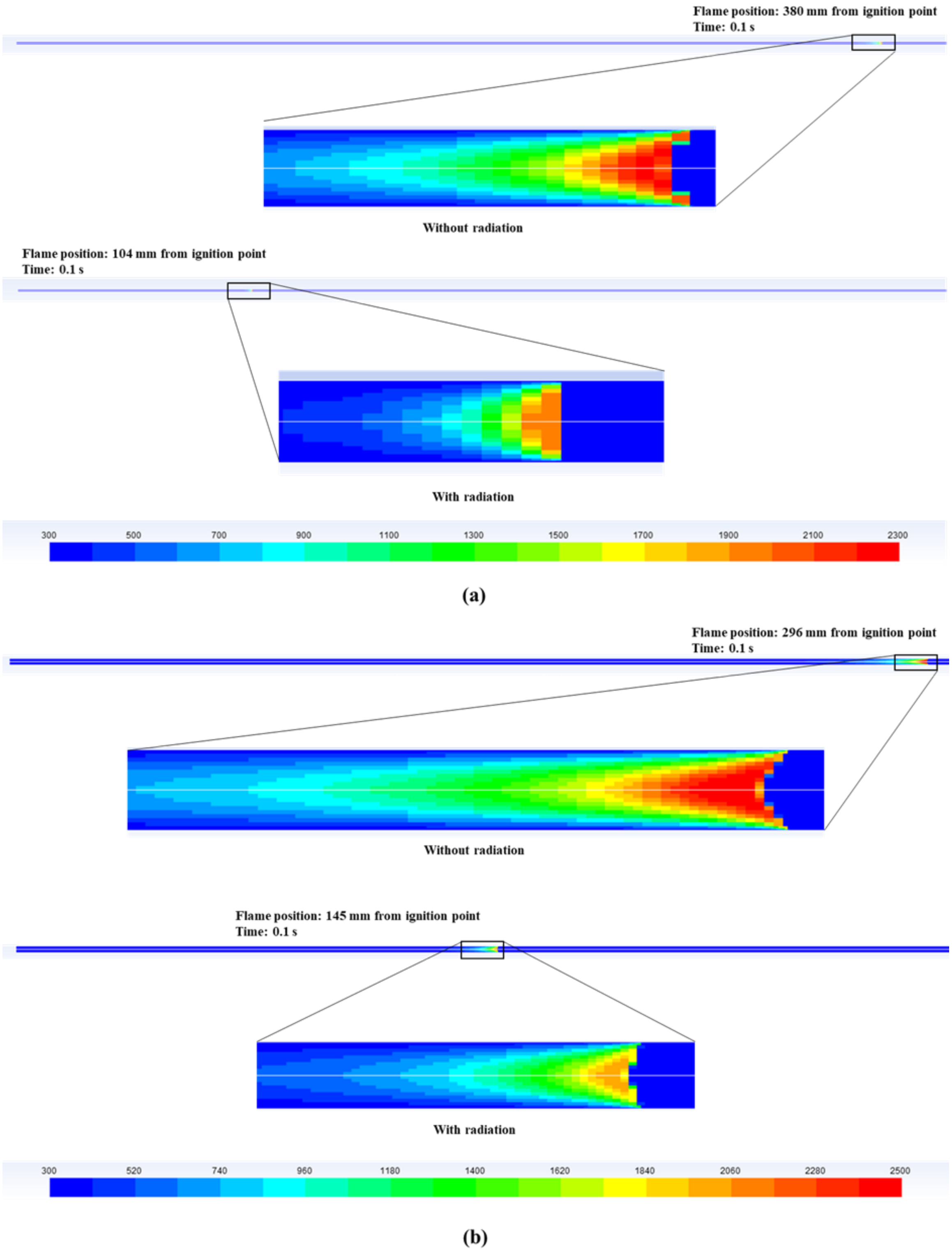

Figure 3.9. Flame front locations and temperature profiles (K) with or without radiation modeling in the Planck-mean absorption coefficient approach: a) 1 mm tube; b) 2 mm tube. Flow time is 0.1 seconds in all cases.

The result of these calculations is that flame speeds are about 73% lower in the 1 mm tube and about 51% lower in the 2 mm tube when radiative heat transfer is accounted for. Additionally, the flame shape became less concave as radiation was accounted for. These changes in flame shape also affect flame velocity due to changes in reaction zone surface area. Figure 3.10 shows a comparison of the fraction of energy lost by radiative effects to the energy produced by the combustion reaction.

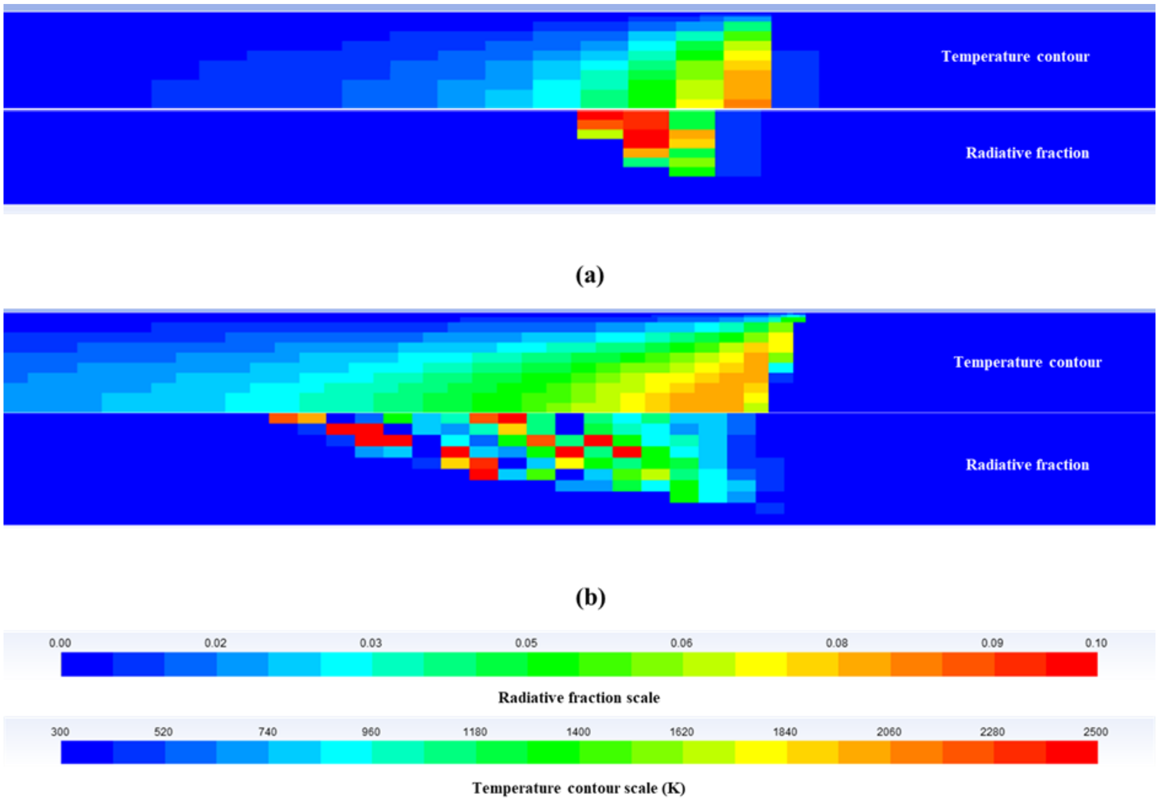

Figure 3.10. Temperature contours and corresponding fraction of radiative heat loss at same time step: a) 1 mm tube; b) 2 mm tube.

The fraction of heat loss due to radiative heat effects is between 12 – 17% for the 1 mm tube and is between 9 – 12% in the 2 mm tube. Radiative heat transfer effects are more significant in smaller tubes due to increased ratio of wall surface area to flame volume.

Application of the radiation model through the WSGG approach produced similar flame velocities as the Planck-mean approach in both 1 mm and 2 mm tubes. The magnitude of the source term reflecting heat losses due to radiation of CO_2 and H_2O was not significantly different between the two methods applied in this study.

Wall Boundary Conditions

The effect of wall boundary conditions was also examined. Most of the simulations discussed in this study used isothermal wall boundaries at 300 K. A set of simulations in both 1 mm and 2 mm tubes was conducted with adiabatic wall conditions to determine the effect on flame temperature and flame velocity. Figure 3.11 shows the flame temperature profiles in simulations with isothermal and adiabatic wall conditions.

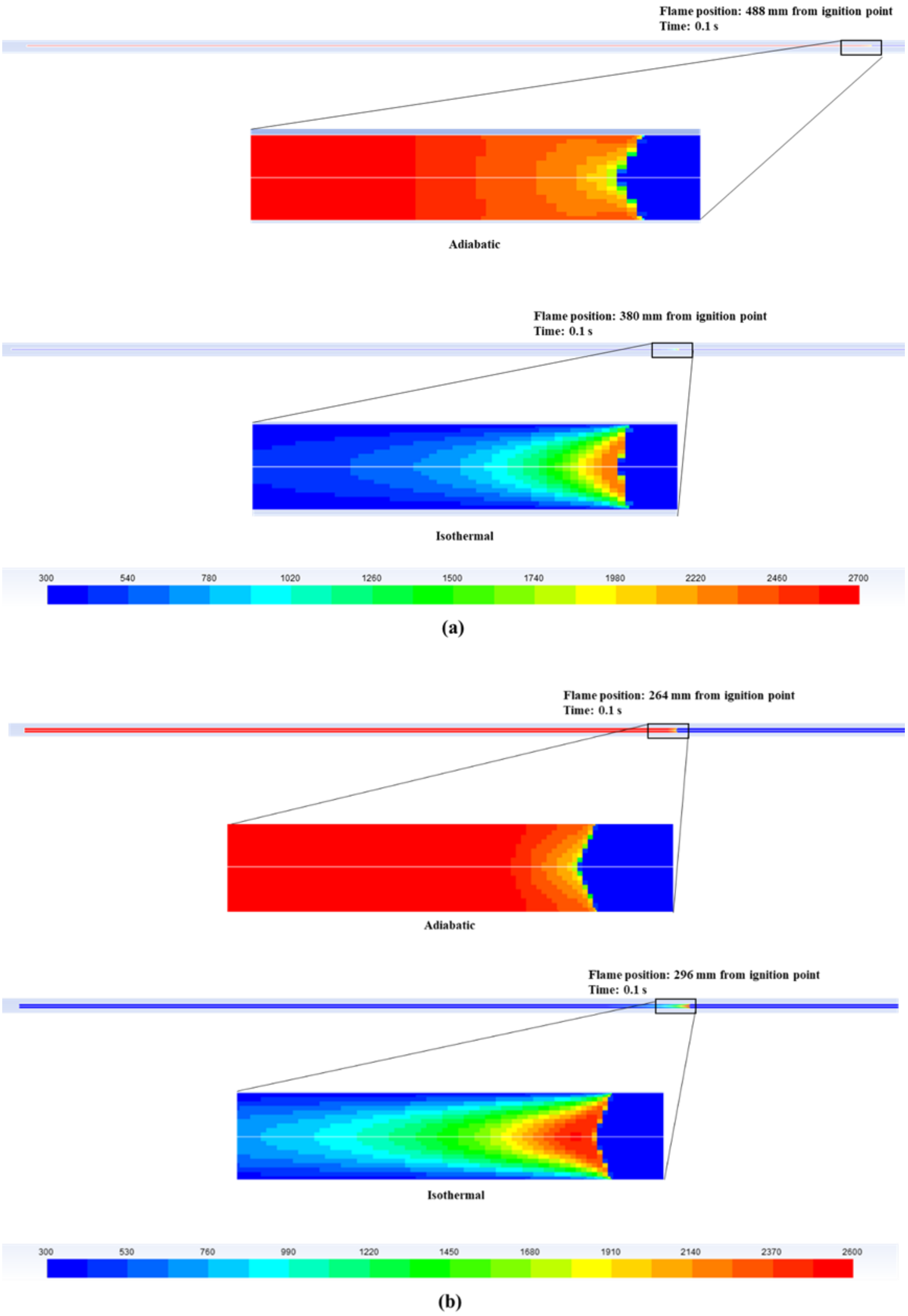

Figure 3.11. Flame temperature profiles with isothermal or adiabatic wall boundary conditions: a) 1 mm tube; b) 2 mm tube. The adiabatic case is the top illustration in both cases.

The application of adiabatic wall conditions had a larger impact on the flame velocity and flame temperature in the 1 mm tube than in the 2 mm tube. The flame velocity increased when adiabatic wall boundary conditions were applied to the 1 mm tube by approximately 28%. The 2 mm tube produced an opposite effect; the flame velocity decreased by approximately 11%. When isothermal conditions are applied, product gases first jet radially inward and then can travel by convection upstream or downstream, resulting in flame acceleration or deceleration in comparison to the adiabatic case. In both cases, the burned gas region behind the flame achieved a greater temperature in the adiabatic case than any region of the flame structure in the isothermal case. Heat transfer effects through wall surfaces are more significant as the tube diameter decreases.

Conclusions

The 10-step reaction mechanism used in this study that was developed for non-premixed systems has been shown to be useful in simulations of premixed ethylene-oxygen combustion. Laminar flame velocities and temperatures resulting from the use of the mechanism in simulations agree with previously published experimental data. Additionally, the use of this reduced mechanism can produce accurate results while keeping computational cost lower than use of detailed reaction mechanisms of several hundred steps. The use of single-step global reaction mechanisms results in an overestimation of CO_2 concentration at the flame front, resulting in lower flame temperatures and velocities. Additionally, as radiation modeling is applied, an overestimation of CO_2 concentration would yield a corresponding overestimation of radiative losses. The tradeoff between computational speed and accuracy is apparent with the choice of chemical reaction mechanism.

Spatial and temporal discretization was found to be sufficient at 0.0305 mm and 1 μs, respectively. These values agreed with previously published data on reaction zone length and reaction timescales at lean equivalence ratios. Adequate spatial and temporal discretization schemes are necessary to adequately resolve reaction zones; however, these schemes may change with the use of different reaction mechanisms. In any case, monitoring accumulated integration error due to discretization is an important factor to consider; larger computational domains result in larger accumulated integration error but finer cell sizes can keep the error under an arbitrary limit. The mesh resolution used in this study achieved an accumulated integration error of approximately 0.06%.

Researchers conducting simulations in millimeter-scale tubes would be advised to consider the method of modeling heat transfer through boundaries with computational domains of less than 2 mm diameter. Flame velocities in small tubes were greatly affected by thermal boundary conditions; a 28% increase in flame velocity was observed in the 1 mm tube when adiabatic conditions were applied. Additionally, radiative heat transfer effects are important to consider, especially as the size of the tube decreases. Flame velocity decreases of 73% and 51% were observed in the 1 mm diameter and 2 mm diameter tubes. Radiant fraction was larger with the smaller tube, and changes to flame shape were observed in both tubes when radiation was accounted for.

CHAPTER IV

IMPACT OF OXYGEN INDEX ON SOOT MODELING PARAMETERS AND RADIATIVE HEAT TRANSFER IN LAMINAR ETHYLENE-OXYGEN DIFFUSION FLAMES

Abstract

Numerical investigation of laminar ethylene-oxygen diffusion flames was conducted to model soot production and subsequent radiative heat transfer effects. A 10-step global chemical reaction mechanism for ethylene combustion was used to facilitate computational efficiency. This reaction mechanism included acetylene chemistry due to its importance as a soot precursor species. Adjustment of the soot nucleation parameter (C_α) was used in conjunction with the Moss-Brookes soot model to produce peak soot volume fraction predictions and soot profiles in agreement with experimental data over the range of oxygen indices 21% - 90%. A model for determination of the soot nucleation parameter as a function of oxygen index (OI) is proposed. This model was applied to additional experimental data featuring different fuel inlet Reynolds numbers and oxidizer compositions. The proposed model produced peak soot volume fractions in agreement with experiment when the oxidizer was O_2/CO_2, but underpredicted peak soot volume fraction when the oxidizer was O_2/N_2. Soot and non-gray radiative heat transfer effects were modeled with a weighted-sum-of-gray-gases (WSGG) approach with five gray gases. Increasing oxygen index from 50% to 90% resulted in decreases in laminar flame height from 36.4 mm to 18.2 mm and increases in radiant fraction from 0.09 to 0.26.

Background

Combustion processes are used routinely in everyday life across the globe. Although many combustion processes have been integrated into well-established applications, combustion phenomena remain a major area of active research. Some of the major aspects of combustion processes that arise in research are the complexity of chemical kinetics, heat and mass transfer, turbulence, and radiation [89]. Hydrocarbon combustion constitutes a major area of research, both experimentally and numerically, especially due to increased demand on limiting emission of pollutant and greenhouse gases. Hydrocarbon combustion produces emissions that are harmful to human health and the environment, such as CO, CO_2, NOx, and soot [32, 53, 89]. Accordingly, research aimed at minimizing these emissions and the design of new combustion chambers that adhere to current regulations is ongoing [30].

Oxy-fuel combustion has shown promise as a technology that can address the shortcomings of conventional combustion. In oxy-fuel combustion, nitrogen is removed from the oxidizer stream through an air separation unit. The resulting combustion products are largely carbon dioxide and water vapor. The water vapor can be condensed to separate the gases, and the remaining CO_2-rich flue gas can be recycled back to the combustion chamber to increase conversion, decrease flame temperatures, and increase the capability to sequester carbon dioxide from the process [1, 33, 72].

Hydrocarbon fuels, such as ethylene, often produce condensed carbon particles (soot) due to incomplete combustion in the fuel rich regions of the flame [89, 90]. However, it has been shown that the presence of CO_2 in hydrocarbon diffusion flames suppresses soot production [90]. While the actual mechanism of soot suppression by CO_2 is not well understood from a mechanistic point of view [31], there are three apparent controlling factors: the lowering of reactant concentrations of soot-producing reactions by dilution, lowering of the soot nucleation rate through a decrease in flame temperature, and increased consumption of soot particles and soot precursor species through oxidation reactions [32, 90]. Additionally, the presence of soot in combustion chambers increases radiative heat transfer within the chamber [1, 30] and is often the dominant factor when compared to radiative transfer due to combustion gases alone [30, 52].

To adequately compare soot production in oxy-fuel to conventional fuel-air combustion in numerical studies, it is important to accurately model soot production and resulting radiative heat transfer effects [72]. The practical application of CFD modeling on soot production and radiative heat transfer aims to account for soot impacts on heat loading of combustion chamber/furnace walls [30, 52]. However, soot formation in numerical studies is often neglected due to the complexity and increased computational time required [31]. Soot modeling itself is challenging; it involves complex chemical kinetics with vastly different timescales, heterogeneous phase reactions, and is highly dependent on local temperatures [30, 31]. In fact, as recently as 2018, there was a notable lack of versatile soot formation models that performed well within a wide range of oxidizer/flue recycle stream compositions in oxy-fuel combustion [32].

Generally, soot production begins with fuel pyrolysis to form acetylene as a soot precursor. Polycyclic aromatic hydrocarbons (PAH) can be formed from acetylene by hydrogen-abstraction-carbon-addition (HACA) reactions during combustion, which can then combine with acetylene to form larger PAH molecules. Further, additional hydrocarbons can attach to the surface, forming a soot particle. This particle can continue to grow by coalescence of additional hydrocarbons, or can shrink by oxidation reactions [31, 89, 91].

This process can be impacted by the composition of the oxidizer. Changes in the oxygen index affect soot production through competing mechanisms. The increased oxygen concentration increases flame temperature, which increases rates of soot nucleation and growth. Simultaneously, increased oxygen concentration enhances rates of soot oxidation and reduces flame residence times for soot production reactions, resulting in decreased soot volume fractions [37, 52, 92, 93].

The process described above is challenging to model and computationally intensive. Conserved scalar approaches based on mixture fractions have been used extensively to reduce computational times associated with numerical simulation of combustion processes. However, modeling of soot production cannot be simplified in this manner; soot-producing reactions and soot diffusion is slow compared to fast combustion reactions that can be assigned a conserved scalar. Therefore, individual transport equations for soot production must be included when conserved scalar approaches are used [94].

There have been several experimental and numerical studies regarding soot production in light hydrocarbon combustion. Generally, researchers observed increased flame length, increased flame temperature, and increased peak soot volume fraction as oxygen index increased [32, 52, 53, 95] but experimental data has also shown a sharp reduction in soot volume fraction as OI reaches high levels [95, 96]. The experimental basis for this study is a series of laser-induced incandescence (LII) measurements of soot volume fractions in laminar ethylene-oxygen diffusion flames conducted by Saanum and Ditaranto [96]. This study showed a strong soot volume fraction dependence on oxygen index resulting from differences in local flame temperatures and species profiles. Additionally, it showed that CO_2 presence in the oxidizer suppresses soot formation, as also explained by Liu *et al*. [90]. An additional set of experiments conducted by Escudero *et al*. [53] in which OI was varied with N_2 dilution, and experiments conducted by Zhang *et al*. [32] with CO_2 dilution were used to determine the validity of the soot nucleation parameter model proposed in this study.

A 10-step, 11-species reduced global chemical reaction mechanism proposed by Lovas *et al.* [74] that was validated for ethylene diffusion flames was used throughout this study. This mechanism was used due to its ability to produce laminar flame velocities and flame lengths that agree with experimental data while saving computational time. Additionally, this mechanism has not been widely used in the numerical combustion literature. Comparisons of numerical results against experimental or analytical values for laminar flame height, flame temperature, and radiative fraction are presented in this study.

Numerical Methods

The commercial CFD software package ANSYS Fluent (version 19.1) [67] was used to characterize non-premixed combustion properties of ethylene with various oxidizer compositions. The computational domain was constructed and discretized within ANSYS Workbench and imported into Fluent for computation. Solver settings specific to this study, procedures for obtaining mesh-independent results, initialization methods, and the use of various models to characterize flame properties are outlined in the following subsections.

Solver setup

A summary of the modeling options used in this study is shown in Table 4.1. The selection of these solver settings was made to adequately model the diffusion flame scenario with radiation, soot production, and detailed kinetics while maintaining a low computational cost.

Table 4.1. Modeling options used in study of non-premixed ethylene-oxygen combustion.

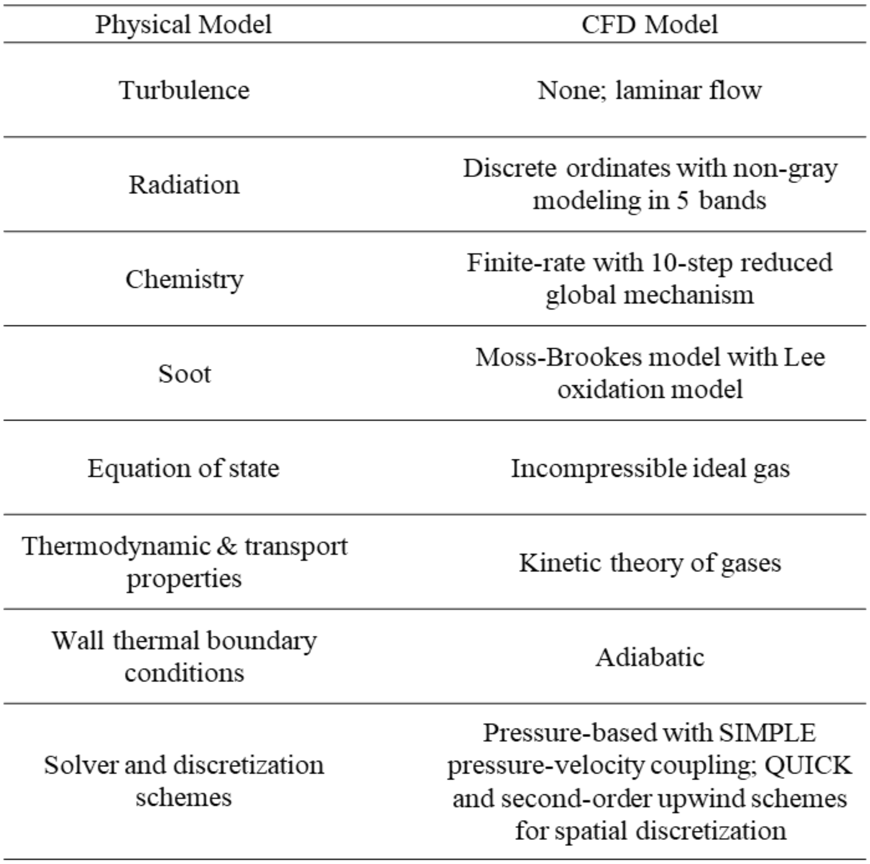

Physical Model	CFD Model
Turbulence	None; laminar flow
Radiation	Discrete ordinates with non-gray modeling in 5 bands
Chemistry	Finite-rate with 10-step reduced global mechanism
Soot	Moss-Brookes model with Lee oxidation model
Equation of state	Incompressible ideal gas
Thermodynamic & transport properties	Kinetic theory of gases
Wall thermal boundary conditions	Adiabatic
Solver and discretization schemes	Pressure-based with SIMPLE pressure-velocity coupling; QUICK and second-order upwind schemes for spatial discretization

The selection of spatial discretization schemes shown in Table 4.1 allowed second-order accurate methods to be employed while maintaining computational efficiency. The ideal gas equation of state was chosen due to its applicability to gas-phase fluid dynamics, lack of large pressure gradients in the system under study, and computational speed. The methods employed for radiation modeling, reaction modeling, and soot modeling are discussed in greater detail in the following sections.

Computational Domain and Initialization Methods

A computational domain was developed to resemble a general non-premixed combustion chamber. The general schematic of the chamber is shown in Figure 4.1. The computational domain includes inlet nozzles for the fuel and oxidizer components and an outflow boundary at the opposite end of the chamber.

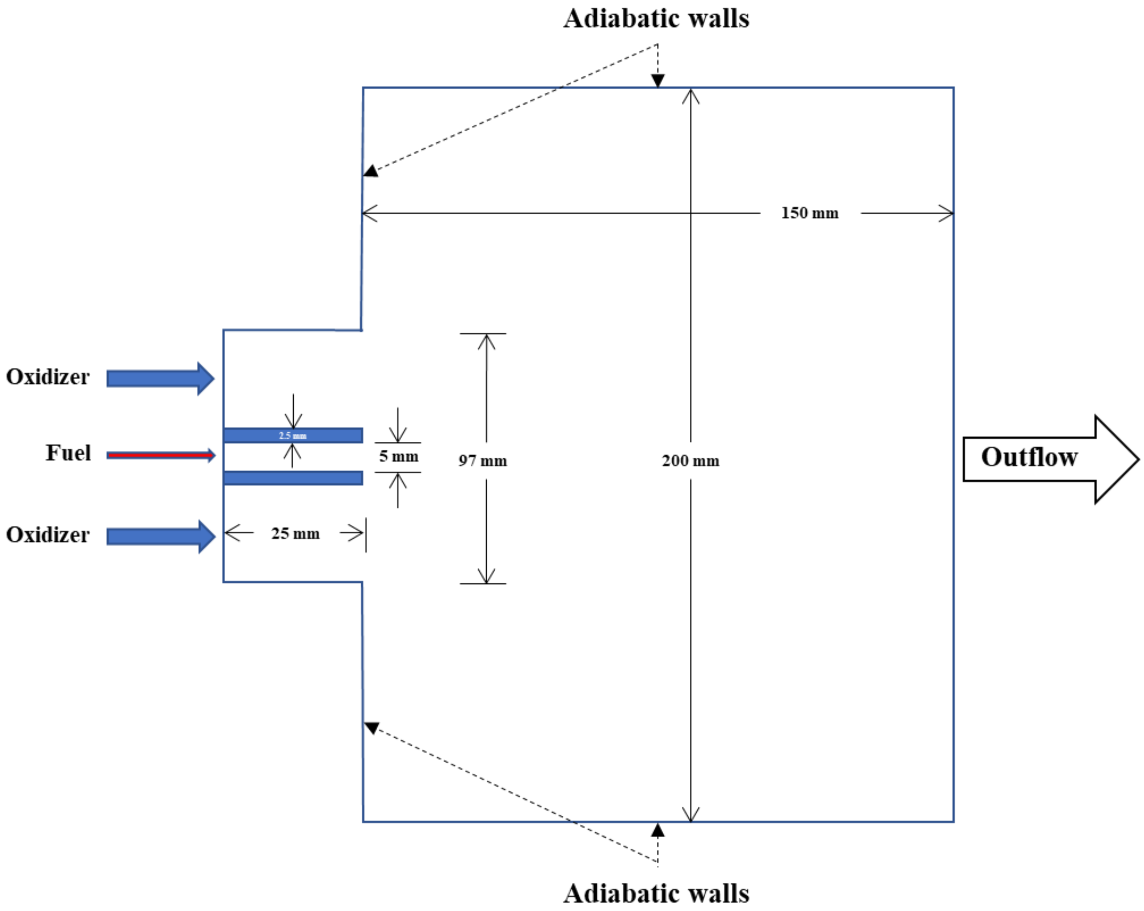

Figure 4.1. Schematic of non-premixed ethylene-oxygen combustion chamber.

The dimensions of the fuel and oxidizer inlets were specified to replicate the dimensions of a physical combustion chamber [97] for comparison purposes. The larger internal dimensions of the chamber were set large enough so that the flame would be fully encompassed within the chamber and that the side walls would not affect either the flow of fuel/oxidizer into the chamber or development of the flame.

The computational domain was divided into finite volumes with a mesh that is shown in Figure 4.2. The initial mesh consisted of 65196 computational nodes and the dimensions of each 2-D computational cell was 0.5 mm in both directions.

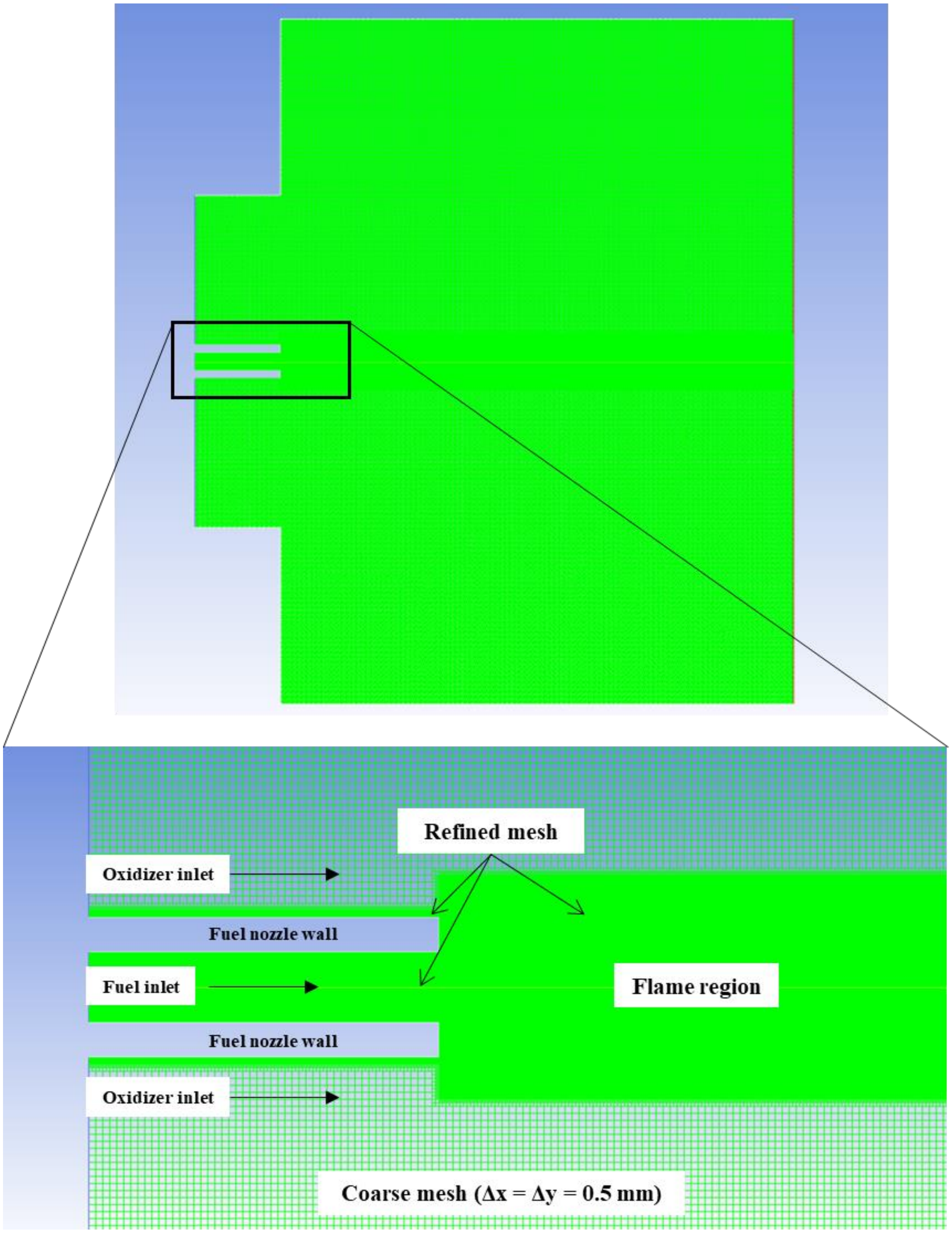

Figure 4.2. Computational domain showing overall mesh (above) and regions of mesh refinement (below).

The mesh within the region encompassing the flame was refined during a grid convergence study to achieve grid-independent results. A fully developed parabolic flow velocity profile was specified at the fuel inlet boundary while a flat velocity profile was specified at the oxidizer stream inlet. These profiles were chosen to closely replicate experimental conditions [96, 97]. Additionally, the mesh within the fuel inlet and the region adjacent to the no-slip wall of the oxidizer inlet was refined to ensure full resolution of flow characteristics of the fuel and oxidizer entering the combustion chamber. The refined region of the mesh can be seen in the bottom portion of Figure 4.2. A further discussion of the grid convergence study is found within the results section of this chapter.

Initialization of each simulation conducted in this study proceeded in a similar manner. The fuel inlet was specified as pure ethylene gas and the oxidizer inlet was specified with varying mole fractions of oxygen, carbon dioxide, and nitrogen. The mass flow rates of the fuel and oxidizer streams were constant throughout all simulations; these values are shown in Table 4.2 along with other initialization values common to the simulations conducted.

Table 4.2. Initialization values for non-premixed ethylene combustion simulations.

System Parameter	Value
Pressure	101325 Pa
Initial Temperature	300 K
Fuel Inlet Velocity	0.21 m/s
Oxidizer Inlet Velocity	0.23 m/s
Fuel Stream Temperature	300 K
Oxidizer Stream Temperature	300 K
Fuel Stream Composition	C_2H_4
Oxidizer Stream Composition	Air, O_2/CO_2
Initialization Kernel Temperature	1000 K

The combustion reaction was initiated within the domain by patching a small region of high temperature at the tip of the fuel nozzle. The composition of the oxidizer stream was varied from air to one of several different oxygen/carbon dioxide mixtures with a range of oxygen indices from 35% to 90% by volume.

Reaction Mechanism

The reaction mechanism used in this study is the same 10-step, 11-species reduced mechanism that was used in the non-premixed study as detailed in Chapter 3 (see Table 3.5). The mechanism was proposed by Lovas *et al*. [74] and was designed for use in diffusion flames such as those under study in this chapter. This mechanism is particularly suitable for this study due to the addition of acetylene, an important precursor species in soot production during hydrocarbon combustion [30, 31, 36, 55-57, 74].

Although this reduced mechanism was developed for premixed combustion systems, it has not been widely examined for use as a tool to reduce computational load over larger detailed reaction mechanisms. The study presented in Chapter 3 is the first to use this mechanism for non-premixed systems; the study presented in this chapter is the first to use this mechanism to characterize soot production in ethylene-oxygen flames at a range of oxygen indices.

Laminar Flame Length

Determination of laminar flame lengths used for comparative purposes in this study follow the analysis of Roper [98, 99] where flame lengths (H) are calculated by

$$\frac{H}{Q} = \left[4\pi D_0 \ln\left(1 + \frac{1}{S}\right)\right]^{-1} \left(\frac{T_0}{T_f}\right)^{0.67}$$

where Q is the volumetric flow rate of fuel, D_0 is the binary diffusion coefficient of fuel into air at ambient temperature, S is the ratio of volume of oxidizer to volume of fuel for complete combustion, T_0 is the ambient temperature, and T_f is a characteristic diffusion temperature. Roper *et al*. [100] used 1500 K for T_f as a reasonable mean temperature for the region of the flame controlling diffusion, and that strategy was adopted in this study. The binary diffusion coefficient (0.1655 cm^2/s) was obtained from an experimental study of the diffusion of various hydrocarbons into air at 298 K [101]. The theoretical flame lengths for the combustion scenarios examined in this study are reported in the results section.

Soot Modeling

The Moss-Brookes soot model was used to model soot production throughout this study. Compared to one-step or two-step soot models such as the Khan & Greeves or Tesner models, the Moss-Brookes model uses less empiricism in the determination of soot production [67]. Additionally, this model has been shown to accurately characterize soot formation in methane flames [94] and has been used to model soot production from heavier hydrocarbons such as ethylene and heptane [89, 102-104]. Within the Fluent application, the model solves two transport equations for soot nuclei concentration (b^*_{nuc}) and soot mass fraction (Y_{soot}) [67]:

$$\frac{\partial \rho b^*_{nuc}}{\partial t} + \nabla \cdot (\rho \vec{v} b^*_{nuc}) = \nabla \cdot \left(\frac{\mu_t}{\sigma_{nuc}} \nabla b^*_{nuc} \right) + \frac{1}{N_{norm}} \frac{dN}{dt}$$

$$\frac{\partial \rho Y_{soot}}{\partial t} + \nabla \cdot (\rho \vec{v} Y_{soot}) = \nabla \cdot \left(\frac{\mu_t}{\sigma_{soot}} \nabla Y_{soot} \right) + \frac{dM}{dt}$$

where N is the soot particle number density, M is the soot mass density, N_{norm} is a normalization constant (10^{15} particles), μ_t is the turbulent viscosity, and $\sigma_{nuc/soot}$ are the turbulent Prandtl numbers for nuclei and soot transport, respectively. The rate of production of soot particles used as a source term in the soot nuclei transport equation is given by the Moss-Brookes model accounting for nucleation and coagulation [67, 89, 94, 103]:

$$\frac{dN}{dt} = C_\alpha N_A \left(\frac{X_{prec}P}{RT}\right) \exp\left\{\frac{-T_\alpha}{T}\right\} - C_\beta \left(\frac{24RT}{\rho_{soot}N_A}\right)^{1/2} d_p^{1/2} N^2$$

where N_A is the Avogadro number, X_{prec} is the mole fraction of soot precursor species (C_2H_4 and C_2H_2 in this study), ρ_{soot} is the mass density of soot (1800 kg/m^3), and d_p is the mean diameter of a soot particle. The first term on the right-hand side of the above equation relates to soot nucleation; C_α is the nucleation parameter and T_α is the activation temperature for the nucleation reaction. The second term in the right-hand side of the equation deals with coagulation and C_β is the model parameter for coagulation.

The source term in the soot mass fraction transport equation is given by [67, 89, 94, 103]:

$$\frac{dM}{dt} = C_\alpha M_P \left(\frac{X_{prec}P}{RT}\right) \exp\left\{\frac{-T_\alpha}{T}\right\} + C_\gamma \left(\frac{X_{sgs}P}{RT}\right) \exp\left\{\frac{-T_\gamma}{T}\right\} \left[(\pi N)^{1/3} \left(\frac{6M}{\rho_{soot}}\right)^{2/3}\right]$$
$$- \left[C_{oxid}\sqrt{T}(\pi N)^{1/3} \left(\frac{6M}{\rho_{soot}}\right)^{2/3} \left(C_{\omega,1}\eta_{coll} \left(\frac{X_{OH}P}{RT}\right) + C_{\omega,2} \left(\frac{X_{O_2}P}{RT}\right) \exp\left(\frac{-T_{\omega,2}}{T}\right)\right)\right]$$

where M_P is the mass of 12 carbon atoms, representing the smallest soot particle. The first term on the right-hand side of the soot mass density source equation deals with nucleation. The second term deals with surface growth of soot particles; X_{sgs} is the mole fraction of the surface growth species (C_2H_4 and C_2H_2 in this study), T_γ is the activation temperature for surface growth, and C_γ is the surface growth model parameter. The final term in the equation (term entirely in brackets) refers to consumption of soot particles through oxidation by OH and O_2 based on the Lee *et al*. oxidation model [105]; C_{oxid} is the oxidation rate scaling parameter, η_{coll} is the collisional efficiency, and $T_{\omega,2}$, $C_{\omega,1}$, and $C_{\omega,2}$ are model parameters specific to soot oxidation. As the Lee model for soot oxidation includes molecular oxygen along with hydroxyl radical in soot oxidation processes, the Lee model was chosen over the Fenimore-Jones model [106] due to the high oxygen indices used in this study.

The default parameters assigned in Fluent for the Moss-Brookes soot model are shown in Table 4.3.

Table 4.3. Default Moss-Brookes soot model parameters used by Fluent [67].

C_{α}	$54\ s^{-1}$	T_{α}	21100 K
C_{β}	1	T_{γ}	12100 K
C_{γ}	$11700\ kg \cdot m \cdot kmol^{-1} \cdot s^{-1}$	$T_{\omega,2}$	19778 K
$C_{\omega,1}$	$105.81\ kg \cdot m \cdot kmol^{-1} \cdot K^{-1/2} \cdot s^{-1}$	η_{coll}	0.13
$C_{\omega,2}$	$8903.51\ kg \cdot m \cdot kmol^{-1} \cdot K^{-1/2} \cdot s^{-1}$		
C_{oxid}	0.015		

These parameters are appropriate for methane/air flames but can be adjusted to model soot production in combustion of higher hydrocarbons. Moss *et al.* indicated that soot nucleation parameter (C_{α}) values on the order of 10^9 were required to adequately predict soot volume fraction in ethylene/air diffusion flames [102]. The default values for methane were used in initial combustion simulations of ethylene/oxygen and subsequently adjusted to provide values closer to experimental data. The determination of appropriate soot nucleation parameters for ethylene-oxygen combustion is a focus of this study.

Radiation Modeling

The radiative transport equation (RTE) was solved using the discrete ordinates (DO) method available in Fluent. The DO method was chosen due to its applicability for accurately solving problems involving participating media and particulate effects common in combustion scenarios while keeping computational costs low compared to other radiation models [67]. The angular discretization was kept moderate with $N_{\Theta} = N_{\phi} = 3$. This resulted in a total of 36 control angles for the solution of the RTE within each computational cell in the domain.

The non-gray formulation of the DO model was used to capture radiative heat transfer of high temperature combustion products and soot by specifying five gray bands. The use of the gray-band DO model for spectral intensity I_λ as a function of wavelength (λ), position ($\vec{r}$), and direction ($\vec{s}$) results in the RTE being written as [28, 67]

$$\nabla \cdot (I_\lambda(\vec{r},\vec{s})\vec{s}) + (a_\lambda + \sigma_\lambda) I_\lambda(\vec{r},\vec{s}) = a_\lambda n^2 I_{b\lambda} + \frac{\sigma_s}{4\pi}\int_0^{4\pi} I_\lambda(\vec{r},\vec{s}')\Phi(\vec{s}\cdot\vec{s}')d\Omega'$$

where a_λ is the spectral absorption coefficient, *n* is the refractive index, $I_{b\lambda}$ is the black body intensity from the Planck function, σ_s is the scattering coefficient, Φ is the scattering phase function, and Ω' is the solid angle. Particulate effects on radiative heat transfer from soot production were also included through an addition of particulate-specific absorption coefficients, emission factors, and scattering factors to the RTE.

In this study, the gas-phase refractive index and scattering coefficient were assumed constant, and that the scattering phase function was isotropic ($\Phi(\vec{s}\cdot\vec{s}') = 1$). A weighted sum of gray gases approach was used to calculate absorption coefficients and emission weighting factors within each band through a user-defined function (UDF) [73]. The total radiative flux per computational cell was computed as the difference between the sum of radiation absorption and emission in all five bands. Absorption coefficients (a_i) and emission weighting factors (w_i) within each band (index *i*) were calculated by [73]:

$$a_i = K_{ij}\sum p_n$$

$$w_i = C_{1,j}T + C_{2,j}$$

where p_n is the partial pressure of species n (CO_2 or H_2O) and the coefficients K_i, C_1, and C_2 refer to values obtained by curve fitting weighted sum of gray gas emissivity to total gas emissivity using correlations found in the literature [73]. The index j refers to molar ratios of H_2O to CO_2 used to determine coefficients in Table 4.4.

Table 4.4. Values for determining absorption coefficients and emission weighting factors based on five gray gases and molar ratios of H_2O to CO_2 [73].

Bands (i)	**1**	**2**	**3**	**4**
		H_2O / CO_2 (j) = 0.11		
K	0.06592	0.99698	10.00038	100.00000
C_1	7.85445E-05	-9.47416E-05	-5.51091E-05	7.26634E-06
C_2	2.39641E-01	3.42342E-01	1.37773E-01	4.40724E-02
		H_2O / CO_2 (j) = 0.5		
K	0.10411	1.00018	9.99994	100.00000
C_1	9.33340E-05	-3.08707E-05	-1.01806E-04	-2.25973E-05
C_2	1.89029E-01	2.87021E-01	2.54516E-01	6.54289E-02
		H_2O / CO_2 (j) = 1		
K	0.20616	1.39587	8.56904	99.75698
C_1	9.22363E-05	-4.25444E-05	-9.89282E-05	-3.83770E-05
C_2	1.91464E-01	2.34876E-01	2.47320E-01	9.59426E-02
		H_2O / CO_2 (j) = 2		
K	0.21051	1.33782	8.55495	99.75649
C_1	1.07579E-04	-3.09769E-05	-1.13634E-04	-3.43141E-05
C_2	1.54129E-01	2.43637E-01	2.84084E-01	8.57853E-02
		H_2O / CO_2 (j) = 3		
K	0.22606	1.42179	9.19411	99.99325
C_1	9.87576E-05	-3.08707E-05	-1.19403E-04	-2.83286E-05
C_2	1.74045E-01	2.40128E-01	2.98507E-01	7.08215E-02

The range of applicability of this method is for gas temperatures below 2500 K and was suitable for this study. Temperatures above 2500 K were encountered only in small regions of the flame, and the molar ratios of water to carbon dioxide used to determine absorption coefficients and emission weighting factors were well represented in the flame region as shown in Figure 4.3.

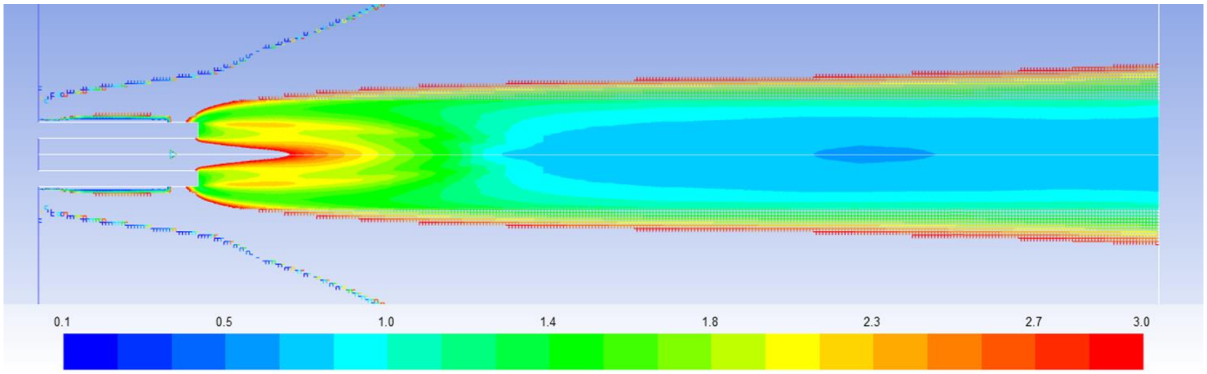

Figure 4.3. Region of computational domain showing molar ratios of H_2O to CO_2 between 0.11 and 3.

The region covered by the applicable molar ratios is consistent with flame location, region of soot production, and region of significant radiative heat transfer.

The objective of radiation modeling in this study is to characterize the fraction of heat generated by the combustion reaction that is lost due to radiative transfer. This radiative fraction was examined for each of the oxygen indices studied, and a discussion of the impacts of radiative loss on non-premixed oxy-fuel combustion systems is presented in the results section.

Results & Discussion

The results of grid resolution, laminar flame length, oxygen index effects on soot production, and radiative fraction are presented in this section. Simulation results are compared to experimental measurements or theoretical predictions. Finally, a model for determining the soot nucleation parameter based on oxygen index is proposed and compared against a different set of experimental soot volume fraction measurements.

Computational Grid Resolution & Inlet Boundary Conditions

A computational grid resolution study was first conducted to ensure that soot volume fraction values obtained with this model were invariant to changes in the mesh. For the grid study, 35% O_2 was selected as the oxidizer and the standard Moss-Brookes soot model with default parameters was used for each successive grid refinement simulation. The region of grid refinement was restricted to the region where the flame resided as well as the fuel and oxidizer inlet regions as shown in Figure 4.2. This was done to limit the impact of grid refinement on computational load. To determine adequate mesh resolution, the values of maximum soot volume fraction were compared among successive grid refinements, wherever they occurred in the domain. Additionally, the soot volume fraction obtained at a constant height (10 mm) above the burner nozzle were compared among successive grid refinements. Figure 4.4 shows the maximum soot volume fraction calculated within the entire domain as well as the value at 10 mm above the burner nozzle as a function of grid refinement

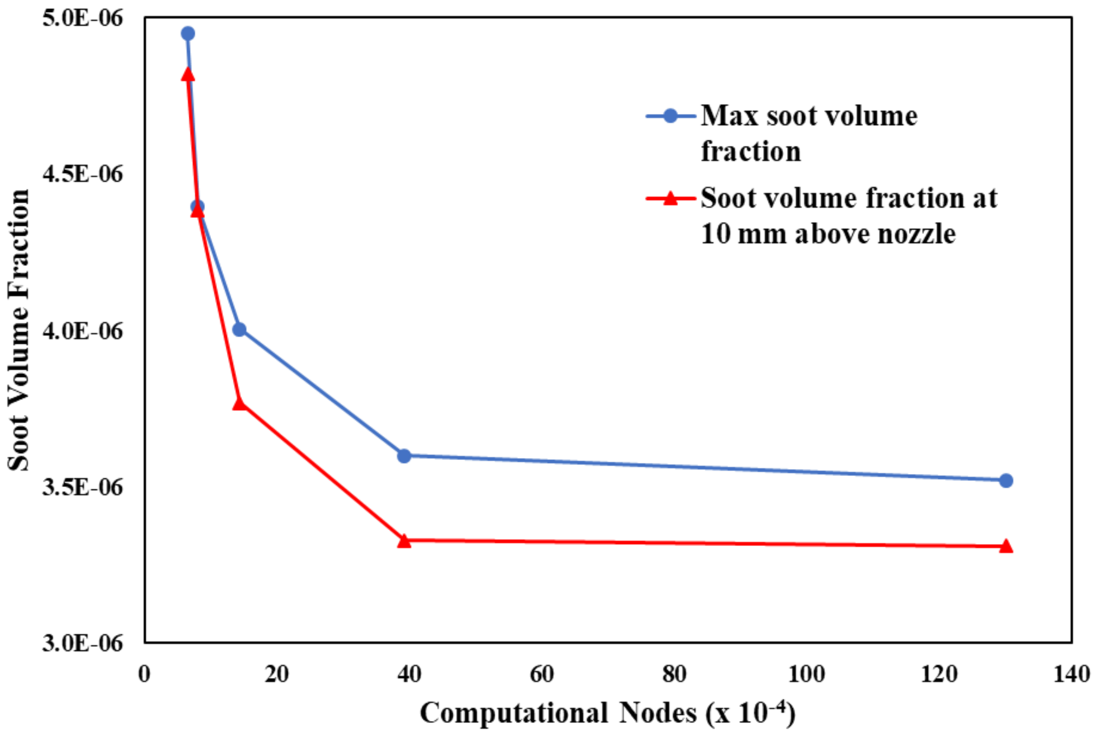

Figure 4.4. Soot volume fraction results obtained as a function of grid resolution for 35% O_2. Maximum soot volume fraction levels and levels at a common distance above the nozzle are displayed.

The number of computational nodes examined ranged from 65196 nodes in the coarsest mesh to slightly greater than 1.3 million in the finest mesh. With mesh cell sizes smaller than 0.0625 mm in the x- and y-directions, the values of soot volume fraction did not change significantly. The grid was considered converged at 0.0625 mm between cell centroids resulting in a total of 392602 computational nodes in the domain. This mesh resolution was used throughout the remainder of the study.

The peak soot volume fraction was evaluated under different boundary conditions for the fuel inlet stream. Either a flat, stabilized fuel inlet velocity profile or a fully developed, parabolic profile was used. The predicted peak soot volume fractions changed between 5-8% depending on the velocity profile and oxygen index. It was determined that a fully developed velocity profile should be used to maintain consistency in comparison of predicted results to experimental data. The experimental description [97] of the oxidizer inlet specified that the stream was stabilized into a flat profile; that boundary condition was used for the oxidizer inlet in all simulations.

Computational Flame Length

The validity of the computational model was tested by comparison of numerical and theoretical laminar flame lengths. The laminar flame length for each oxygen index studied was compared to lengths as determined by the theoretical method and simplifying assumptions given by Roper [98, 99] and a binary diffusion coefficient for ethylene into air at 298 K [101]. Table 4.5 lists the theoretical values for laminar flame height for the combustion scenarios examined.

Table 4.5. Theoretical flame height [98] for various oxidizer compositions in a laminar ethylene flame.

Oxygen Index	Volume Ratio of Oxidizer to Fuel	Volumetric Flow Rate of Fuel (cm^3/s)	Theoretical Laminar Flame Height (mm)
21% O_2 (Air)	14.3	4.12	99.7
35% O_2	8.57	4.12	61.1
50% O_2	6.00	4.12	43.8
70% O_2	4.29	4.12	32.2
90% O_2	3.33	4.12	25.7

Under the same fuel inlet flow conditions, laminar flame heights are expected to decrease with increasing oxygen concentration in the oxidizer stream [37, 52, 59, 98]. The peak concentration of OH radical along the flame axis is the usual criterion for flame length [59, 99]. In simulations conducted with the modeling setup in this study, the same trend was observed. Figure 4.5 (a) – (c) shows the mass fraction of OH radical along the flame axis produced numerically in flames with 50%, 70%, and 90% O_2 by volume.

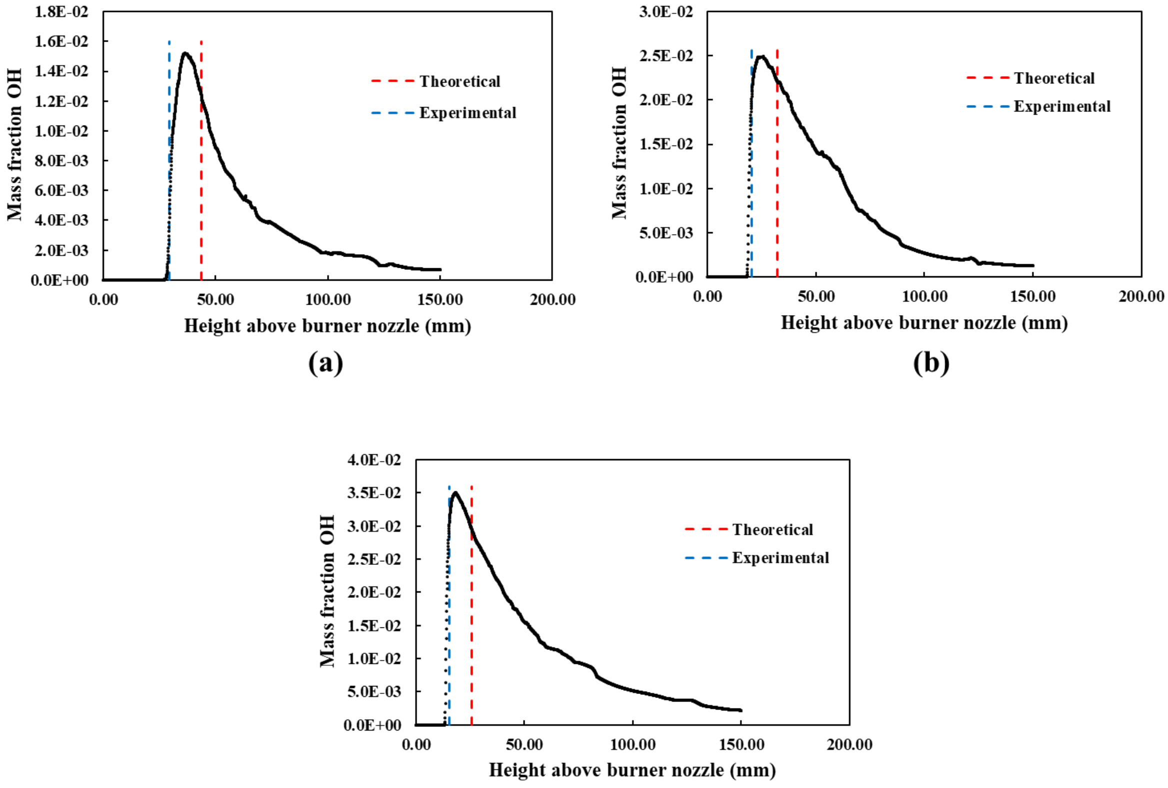

(a)

(b)

(c)

Figure 4.5. OH radical profiles along the flame axis as a function of height above the burner nozzle: (a) 50% OI, (b) 70% OI, (c) 90% OI. Theoretically predicted laminar flame heights [98] and experimentally measured flame heights [96] included as dashed lines for reference.

It is apparent from Figure 4.5 that the peak OH radical concentration produced in this study slightly underpredicts theoretical laminar flame height but slightly overpredicts experimental flame heights. However, it corresponds closely with both the theoretical solution and experimental measurements and displays the trend of decreasing flame height with increasing oxygen index.

Dependence of Oxygen Index on Soot Model Parameters

The Moss-Brookes soot model was used to predict soot volume fractions produced during non-premixed combustion of ethylene with varying concentrations of oxygen in the oxidizer stream. In one of the original papers describing the use of the Moss-Brookes model for predicting soot volume fraction in ethylene flames [102], it was shown that simple scaling of the soot nucleation parameter (C_α) was sufficient to achieve peak soot volume fraction values in agreement with experimental measurements. In this study, a similar approach was used to adjust peak soot volume fraction predictions in line with previous measurements in ethylene flames over the set 21% (air), 35%, 50%, 70%, and 90% O_2 by volume. The experimental baseline for soot volume fraction values is outlined in Saanum and Ditaranto [96], where diffusion flames of varying O_2 / CO_2 ratios were examined. Measurements of peak soot volume fraction and soot volume fraction at varying heights above the burner nozzle for each flame were conducted via a laser-induced incandescence (LII) method. Peak soot volume fractions observed for these experiments are shown in Figure 4.6.

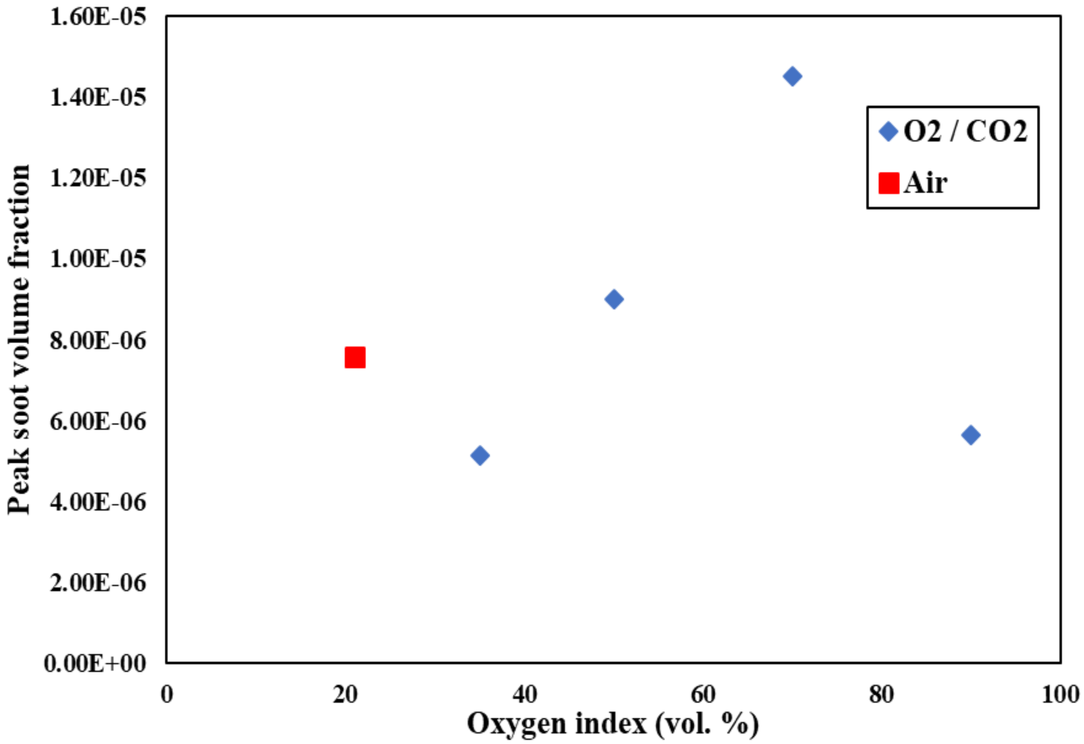

Figure 4.6. Experimental measurements of peak soot volume fraction in ethylene-oxygen diffusion flames at different oxygen indices [96].

Soot volume fraction generally increases with increasing oxygen index, with a maximum value of around 15 ppm at 70% O_2. The decrease in soot volume fraction at higher OI beyond 70% is likely due to a reduction in flame height and the increasing prevalence of soot oxidation processes.

To determine parameter-independent soot predictions as a function of OI, the initial set of simulations were conducted to determine peak soot volume fraction values when soot model parameters were held constant. Figure 4.7 shows peak soot volume fraction as a function of oxygen index when all soot model parameters were kept constant across the range of oxygen indices.

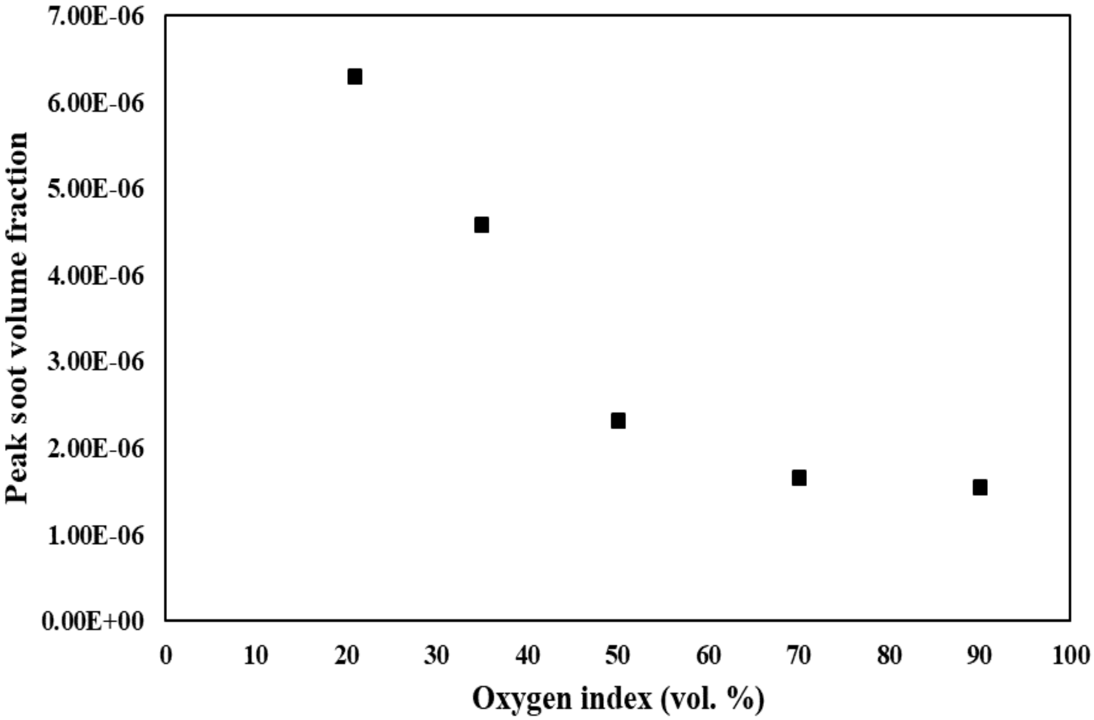

Figure 4.7. Peak soot volume fraction as a function of oxygen index; soot nucleation parameter (C_{α} = 54 s^{-1}) is constant over the range of oxygen indices.

As the oxygen index increases, the predicted value of peak soot volume fraction for a given value of the soot nucleation parameter decreases. It is apparent that holding the soot nucleation parameter constant results in an underprediction of soot volume fraction as OI increases and the model fails to replicate experimental trends.

An examination of how variation in the soot nucleation parameter affected predicted soot volume fraction was conducted for each OI. Simulations at each of the oxygen indices shown in Figure 4.7 were conducted to determine the appropriate value of the soot nucleation parameter that would result in predictions of peak soot volume fraction that agree with experiment. As an example, the peak soot volume fraction predicted as a function of incremental adjustment of C_{α} for a set of simulations with the ethylene flame at 70% OI is shown in Figure 4.8.

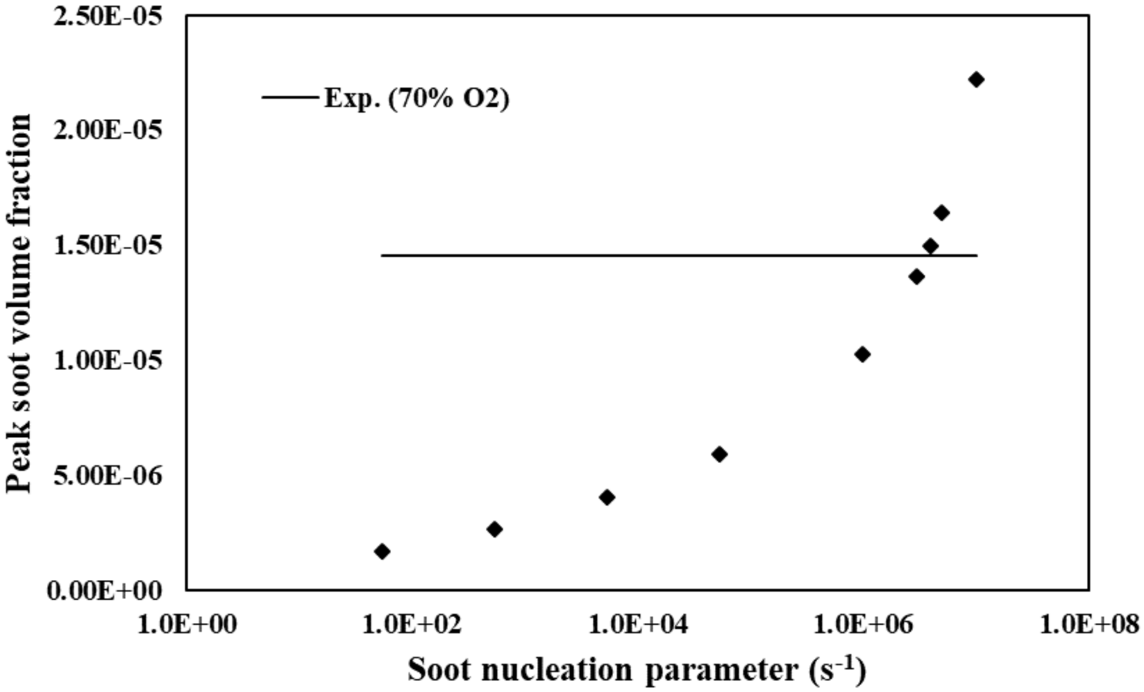

Figure 4.8. Predicted peak soot volume fractions in ethylene-oxygen flames (black diamonds) as a function of soot nucleation parameter for 70% O_2 index. Experimental value [96] of peak soot volume fraction (solid line) included for reference.

The analysis on nucleation parameter shown in Figure 4.8 was conducted for each OI examined to arrive at a specific value of C_α that resulted in peak soot volume fractions that agreed with experiment. The determined values are listed in Table 4.6.

Table 4.6. Values of soot nucleation parameter (C_α) determined in ethylene-oxygen diffusion flames with variable oxygen index.

Oxygen Index	Soot Nucleation Parameter (C_α)	Peak Soot Volume Fraction (Exp)	Peak Soot Volume Fraction (Numerical)
21% O_2 (Air)	4000	7.6E-06	7.5E-06
35% O_2	1800	5.1E-06	5.2E-06
50% O_2	1.0E+06	9.0E-06	8.8E-06
70% O_2	1.4E+07	1.5E-05	1.5E-05
90% O_2	2.3E+06	5.7E-06	5.7E-06

The values for C_α vary significantly as oxygen index increases and the values are much larger than the value associated with methane combustion, in agreement with observations by Moss *et al.* [102]. With these adjusted values of soot nucleation parameter, the soot volume fraction profiles above the burner nozzle were determined and compared against experimental measurements. Figure 4.9 shows the soot volume fractions predicted at 5-10 mm intervals above the nozzle for each OI and Figure 4.10 (a) – (d) shows the mesh-resolved numerical soot volume fraction profiles.

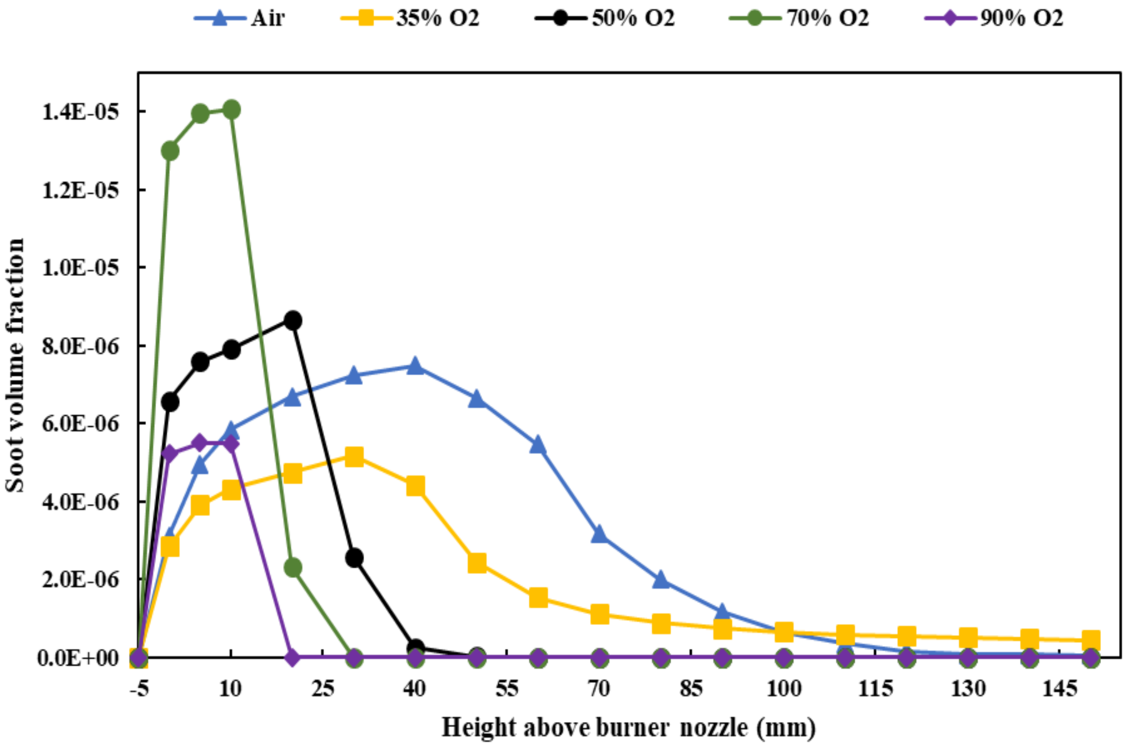

Figure 4.9. Soot volume fraction as function of height above the burner nozzle for OI 21% - 90%.

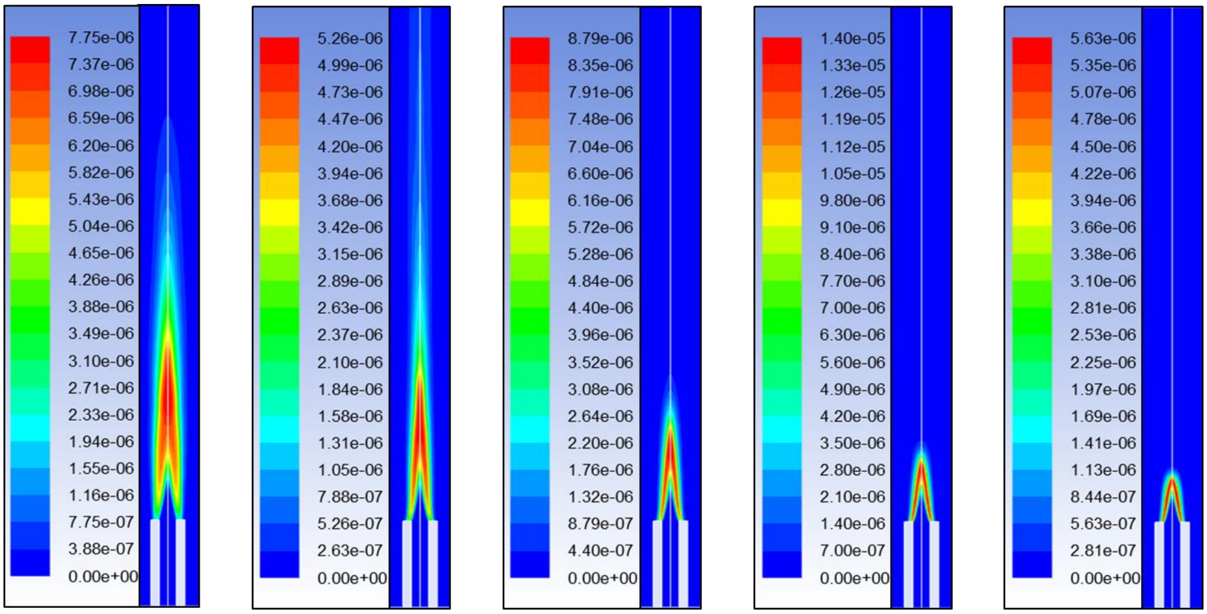

(a) **(b)** **(c)** **(d)** **(e)**

Figure 4.10. Numerical soot volume fraction profiles of ethylene diffusion flames: (a) Air; (b) 35% O_2; (c) 50% O_2; (d) 70% O_2; (e) 90% O_2

The soot volume fraction profiles seen in Figures 4.9 and 4.10 accurately predict peak soot volume fraction and narrowing of the soot region as OI increases. Direct comparisons of the axial soot profiles at each OI with the experimental data are shown in Figure 4.11 (a) – (e).

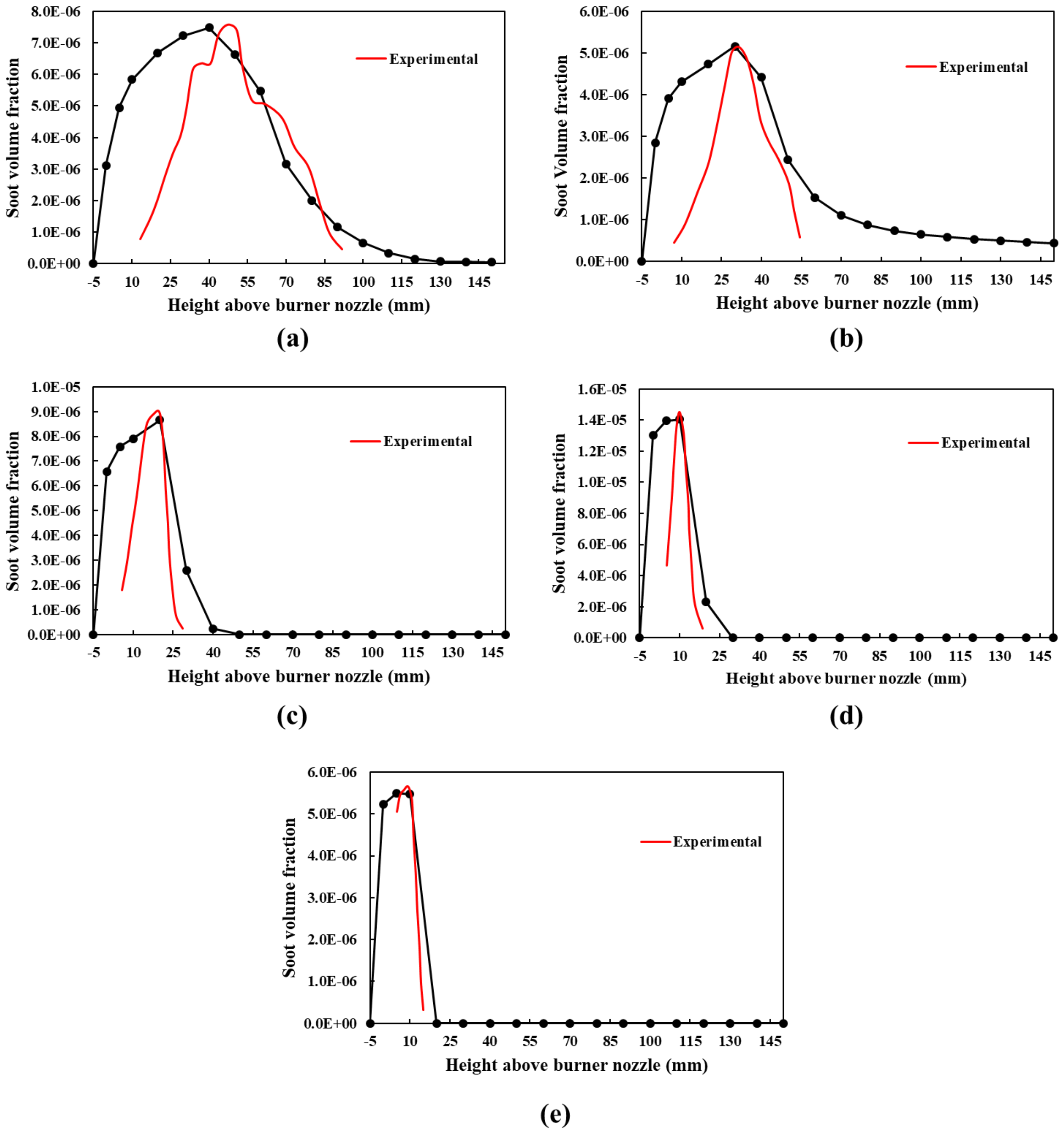

Figure 4.11. Axial soot profiles predicted by the numerical model compared against experimental measurements [96]: (a) Air; (b) 35% O_2; (c) 50% O_2; (d) 70% O_2; (e) 90% O_2. Experimental measurements are indicated in red lines in all cases.

The slight disagreement at regions close to the burner nozzle exit may be a result of LII measurement sensitivity in the experiment. However, the peak soot volume fractions and narrowing of the soot-producing region in the flame are in close agreement with the experimental data reported by Saanum and Ditaranto [96].

The results of this study led to the development of proposed models for the soot nucleation parameter as a function of oxygen index. Using the full set of results from all the oxygen indices examined, the model is

$$C_\alpha = 2 \times 10^{-5}(OI)^{5.9865}$$

However, as the peak soot volume fraction exhibits a significant decrease at OI higher than 70%, another model was developed that neglects the 90% OI result. This model was found to perform better against additional experimental measurements where the oxygen index was below 70%. The model for oxygen indices up to 70% is

$$C_\alpha = 2 \times 10^{-7}(OI)^{7.3738}$$

This second model was validated against two different sets of experimental data that featured different combustion geometries, fuel Reynolds numbers, and oxidizer compositions than the Saanum experiment. The first, published by Escudero *et al*. [53], measured peak soot volume fractions in ethylene flames where O_2/N_2 was the oxidizer, and the oxygen concentration was varied from 21% - 37%. The fuel stream Reynolds number was approximately one-fifth of the fuel stream Reynolds number of the experiment on which the model was based. The second set of experimental data used to validate the soot nucleation parameter model was published by Zhang *et al.* [32] where the oxidizer was O_2/CO_2 and the OI was varied from 30% - 50%. In both cases, new computational domains were constructed to replicate fuel and oxidizer inlet dimensions, and boundary conditions were adjusted to replicate fuel and oxidizer flow rates and compositions. Additionally, the highest reported oxygen index in each of the two additional experimental results were selected for comparison against the model predictions. Table 4.7 shows the model-based value used for C_α and predicted peak soot volume fractions compared against experimental soot volume fraction measurements from both experiments.

Table 4.7. Model-predicted peak soot volume fractions compared to experimental [32, 53] peak soot volume fraction measurements at selected oxygen indices.

Oxygen Index	Model-derived C_α	Experimental Peak SVF [53] (ppm)	Experimental Peak SVF [32] (ppm)	Predicted Peak SVF (ppm)
37%	73221	18 ± 4.5	---	5.85
50%	674365	---	8.22	7.22

The predicted value for peak soot volume fraction at 37% OI was significantly less than the experimental value. This is likely due to the suppression of soot production when using carbon dioxide as the diluent in the oxidizer stream vice nitrogen. Since the model was originally developed against an experiment with O_2/CO_2 as the oxidizer stream, it was expected that the model would underpredict the soot volume fraction for an O_2/N_2 system. In comparing the predicted soot volume fraction at 50% OI against experimental data in which CO_2 was the diluent, much closer agreement was achieved. The soot nucleation parameter model proposed in this study is applicable to laminar ethylene diffusion flames with oxygen indices less than 70% and with carbon dioxide as the diluent in the oxidizer stream.

Oxygen Index Effects on Radiant Fraction

Radiant fraction values for all OI cases were computed by ratio of volume integrals of the radiation source term to the heat of reaction source term in the transport equations. The radiation source term included effects of both radiating gases and the presence of soot. Radiant fraction values for each OI investigated are shown in Table 4.8.

Table 4.8. Radiant fraction values computed in simulations as a function of oxygen index. Experimental value [53] included for reference.

Oxidizer Composition	Peak Soot Volume Fraction (ppm)	Radiant Fraction
35/65 O_2/CO_2	5.2	0.089
50/50 O_2/CO_2	8.8	0.090
70/30 O_2/CO_2	15	0.145
90/10 O_2/CO_2	5.7	0.257
	Experimental [53]	
37/63 O_2/N_2		0.170

The computed values of radiant fraction shown in Table 4.8 are in reasonable agreement with experimental data published by Escudero *et al.* [53]. The Escudero experiment uses an O_2/N_2 mixture as the oxidizer vice O_2/CO_2, so it is expected that the radiant fractions predicted by the simulation are lower. The Escudero experimental data uses a maximum OI of 37% and shows a radiant fraction of approximately 0.17. The predicted radiant fraction in this study is approximately 0.09 at 35% OI. Additionally, the experimental data showed that the radiant fraction increased with increasing OI, due to increased flame temperature. This trend is also observed with the model predictions produced in this study.

Conclusions

This study was conducted to determine the applicability of a reduced global reaction mechanism in modeling soot and radiative heat transfer effects in laminar non-premixed ethylene-oxygen combustion. The model accurately predicts experimental trends in laminar ethylene flames with variation in oxygen index while using a reduced chemical reaction mechanism for computational efficiency. As OI increases, flame temperature increases, flame length decreases, and peak OH concentration increases. The peak soot volume fraction and soot profile within the flame were found to agree with experimental measurement through the tuning of the soot nucleation parameter in the Moss-Brookes soot model.

The adjustment of the soot nucleation parameter (C_α) over a wide range of oxygen indices led to the development of a model for C_α as a function of oxygen index. This model was validated against peak soot volume fraction measurements from additional laminar ethylene diffusion flame experiments, with reasonable agreement. This model should be further refined against additional experimental information under a wider range of oxidizer compositions, chemical reaction mechanisms, and varied soot model parameters like surface growth or oxidation parameters. Additional development of the model at high oxygen indices (above 70%) should be conducted.

Accounting for detailed experimental conditions is important when making comparisons of model predictions against experimental measurements. The fuel inlet stream to the combustion chamber was modeled with and without ensuing full development of a parabolic velocity profile. Small but significant differences in the predicted soot volume fraction resulted depending on the inlet velocity profile.

Addition of CO_2 to the oxidizer stream through flue gas recycle or direct injection has a suppressive effect on soot volume fraction, flame temperature, and radiant fraction. However, radiant fractions as high at 0.26 were predicted in this study due to increased flame temperature at high OI. As CO_2 emissions continue to be regulated, the use of CO_2 in flue gas recycle streams for oxy-fuel combustion appears to be a beneficial aspect to an often-unwanted byproduct.

CHAPTER V

RESEARCH SUMMARY & CONCLUSIONS

Research Summary

Two sets of distinct conclusions can be drawn from this research. The study on premixed ethylene-oxygen combustion in confined spaces (Chapter 3) shows that heat loss mechanisms play an important role in the nature of flame propagation, acceleration, and eventual detonation characteristics. Computational studies on flame propagation modes in premixed combustion systems require extremely precise spatial and temporal discretization, often at the expense of detailed chemical kinetics or incorporation of additional modes of heat transfer such as radiation. In this study, those aspects often neglected were addressed by using a reduced global reaction mechanism and including effects of product gas radiation, while keeping computational cost low.

The non-premixed study (Chapter 4) focused on modeling soot production in laminar ethylene diffusion flames with varying oxygen concentration in the oxidizer stream. Again, chemical kinetics information was addressed with a reduced global reaction mechanism, but radiation from product gases and soot was modeled more rigorously. Soot volume fraction was compared against benchmark experimental data, and laminar flame lengths were compared against theoretical values. An empirical model for the soot nucleation parameter (C_α) was proposed and validated against additional experimental results.

These two distinct studies were conducted with an open source academic CFD code with minimal computational hardware. While the major contributions of the studies are described above, an underlying goal was to perform these calculations with management of computational cost and efficiency in mind. Although computationally efficient, the methods and numerical results outlined in Chapters 3 & 4 represent more than 200 individual simulation trials, totaling more than 650 days of steady computation.

Conclusions

The premixed ethylene-oxygen study was performed in small, confined computational spaces near the lean limit of ethylene combustion. This was done to study flame acceleration characteristics and radiative heat transfer prior to eventual transition to detonation. The results from this study highlight the need to incorporate models or boundary conditions that are often not addressed. The methodology followed in this study shows that computational speed can be maintained while modeling important aspects of the combustion process. There are several important conclusions from this study:

1. Spatial and temporal discretization was found to be sufficient at 0.0305 mm and 1 μs, respectively. These values compared well with established reaction zone lengths and reaction timescales determined from detailed reaction mechanisms at the equivalence ratio ($\Phi = 0.2$) studied.
2. The accumulated integration error was determined to be approximately 0.06%, making the reliability of the simulation high with respect to spatial discretization.
3. The method of combustion initiation at lean conditions was found to be invariant during sensitivity analysis. Experimental observations at higher equivalence ratios showed a difference in flame velocities based on initiation strategy, but the lack of consistent experimental or numerical initiation methods in the literature required the comparison of methods at the lean limit.

4. Accounting for heat transfer due to radiative losses resulted in a reduction of flame velocity by 73% in the 1 mm diameter tube and 51% in the 2 mm diameter tube. Accurate characterization of radiative heat loss becomes more important as the ratio of wall surface area to flame volume increases.
5. Radiant fractions were calculated as 0.12 to 0.17 for the 1 mm diameter tube and 0.09 to 0.12 for the 2 mm diameter tube, depending on the radiation model applied. Although radiative heat loss resulted in decreased flame velocity in both diameter tubes, the differences in flame velocity due to radiation model were negligible.
6. Accurate characterization of wall thermal boundaries is important in small geometries. Simulations with either adiabatic or isothermal wall boundaries resulted in changes to the flame velocity of 28% in the 1 mm diameter tube and 11% in the 2 mm diameter tube. Experimental flame velocities were bounded between calculated values obtained assuming adiabatic conditions and isothermal conditions with radiative heat loss. Thermal boundary characterization is often neglected in the literature.
7. The use of single-step global reaction mechanisms can result in overestimation of flame temperatures and velocities due to an overestimation of CO_2 concentration. The use of a detailed mechanism that accounts for the slow CO oxidation reactions results in lower concentration of CO_2 at the flame front and correspondingly lower flame temperatures and velocities. Additionally, when radiation modeling is applied, increased CO_2 concentration resulting from the use of a single-step global reaction mechanism would also result in overestimation of radiative losses.

The non-premixed ethylene-oxygen combustion study was modeled after an experimental study on soot production in laminar ethylene diffusion flames at different oxygen indices. The overall focus of the study was to highlight the impacts of oxy-fuel combustion on soot volume fraction and the resulting radiative heat transfer impacts on oxy-fuel combustion system design. A similar methodology to the premixed study was followed in this study to manage computational cost. The major conclusions from this study are:

1. Spatial discretization at cell sizes smaller than 0.0625 mm produced grid-independent results. Although the same reaction mechanism was used in both studies, the steady state nature of the diffusion flame allowed grid convergence at larger cell sizes.
2. The fuel stream inlet profile was modeled as either fully developed parabolic flow or stabilized flow, while the oxidizer stream was modeled as a stabilized, flat profile. Small differences in the calculated soot volume fraction were observed, depending on the inlet profile used. Modeling the fuel and oxidizer inlet velocity profiles that are representative of experimental bases is important when comparing numerical results to experimental data.
3. Addition of CO_2 to the oxidizer stream has a suppressive effect on soot volume fraction, likely due to the lowering of flame temperatures. Additionally, soot volume fraction increases as oxygen index increases until a point at which soot oxidation and reduction in flame residence time effects begin to dominate the overall soot formation process.
4. A model for the soot nucleation parameter used in conjunction with the Moss-Brookes soot model and Lee oxidation model that can be used to provide a reasonable estimate of soot volume fraction under a range of oxygen indices in ethylene diffusion flames is $C_\alpha = 2\text{x}10^{-7}(\text{OI})^{7.3738}$.

5. Radiant fraction increases in proportion with oxygen index. This is due to increased soot volume fraction and higher flame temperatures. Oxy-fuel combustion design should account for increased heat loading at the combustor walls if CO_2 is separated from the flue gas recycle stream, resulting in an increased oxygen index.

The conclusions presented by this research provide an efficient CFD framework for future contributions to the body of knowledge on ethylene combustion, safety, and furnace design.

CHAPTER VI

FUTURE RESEARCH

Combustion is a broad area of research, with many potential experimental or numerical avenues of approach. The combination of thermodynamics, transport phenomena, chemical kinetics, fluid dynamics, and numerical methods make further research in this field virtually limitless.

Significant research time has been devoted to simple hydrogen combustion, but there are many other hydrocarbon fuels that should be fully investigated as viable fuel sources for either premixed or non-premixed systems. Although the combustion chemistry is significantly simplified with hydrogen as a fuel, it has inherent problems associated with storage, transport, and safety. Other gas-phase or liquid-phase fuels that are currently used in many combustion applications require insight into complex chemistry and should be further investigated.

Applied vs. Pure Research

Computational fluid dynamics approaches are used throughout the chemical processing industry to save time and materials, and to examine processes under a wide range of conditions that experimentation may not be able to easily replicate. Potential applications of CFD combustion research are the design of safety systems, the optimization of internal combustion engines using a variety of fuel sources, the design of novel engines like pulse detonation engines, oxy-fuel furnace design, industrial piping applications, and minimization of particulate and greenhouse gas emissions. As greater reliance is placed on renewable energy sources, novel uses for application of combustion technologies are warranted.

There are also several potential areas for pure research into combustion processes. The effect of turbulence and improvement in turbulence models, characterization of flame propagation modes in premixed combustion, detailed flame structure in non-premixed combustion, heat transfer, and rate limiting processes are all areas where additional research should be conducted. The ability to accurately characterize detonation risk in industrial chemical processing environments would be extremely beneficial to minimize recurrence of these types of hazards.

Premixed Combustion

One of the least understood processes in premixed combustion is the phenomena of deflagration-to-detonation transitions (DDT). While the current understanding of the process was discussed in Chapter 2, the major controlling mechanism for DDT onset is still debatable. Additionally, the prediction of DDT timing and location within a system configuration has not been demonstrated.

Within the realm of premixed combustion, additional gains could be made in evaluation of different fuels, different equivalence ratios, different system geometries, internal obstacle effects on flame/shock wave propagation, and impacts of high or low system pressure. Additional chemical reaction mechanisms could also be studied for their ability to predict flame velocity and temperature within the framework of computational requirements. A slightly different option for modeling the chemical kinetics of premixed systems, called the flamelet generated manifold (FGM) has shown recent promise in reducing computational load by pre-tabulating species concentrations and temperature profiles, similar to a mixture fraction approach.

Non-premixed Combustion

The benefits of oxy-fuel combustion are apparent from a hazardous emissions standpoint, but direct experimentation with different furnace designs with different operating conditions can be cost prohibitive. CFD simulations can increase efficiency in evaluating different fuel/oxidizer combinations for minimization of soot, NOx, and CO_2 emissions. Development of new soot models, or sensitivity studies on other soot model parameters could be conducted. Additionally, the effect of system pressure, different fuel and oxidizer Reynolds numbers, counterflow configurations, inverse diffusion flames, and mechanisms of soot formation in hydrocarbon flames are all attractive candidates for further research in non-premixed combustion.

APPENDICES

APPENDIX A

NOTATION AND ABBREVIATIONS

A: Arrhenius pre-exponential factor

$\boldsymbol{A}$: surface area vector

a_i: Planck mean absorption coefficient of species i (m^{-1} Pa^{-1})

a_λ: spectral absorption coefficient (m^{-1})

AFT: adiabatic flame temperature (K)

ASU: air separation unit

b^*_{nuc}: normalized soot nuclei concentration (particles m^{-3})

C_α: soot nucleation parameter (s^{-1})

C_β: soot coagulation rate parameter

C_γ: soot surface growth model parameter (kg m $kmol^{-1}$ s^{-1})

CFD: computational fluid dynamics

C_{oxid}: soot oxidation scaling rate parameter

Cp: heat capacity at constant pressure (J K^{-1})

c_p: specific heat capacity at constant pressure (J kg^{-1} K^{-1})

Cv: heat capacity at constant volume (J K^{-1})

c_v: specific heat capacity at constant volume (J kg^{-1} K^{-1})

C_xH_y: generalized hydrocarbon

C_ω: soot oxidation model constant (kg m kmol^{-1} K$^{-1/2}$ s^{-1})

D_0: binary diffusion coefficient (m^2 s^{-1})

d_p: mean diameter of a soot particle

DDT: deflagration to detonation transition

E: total energy (J)

E_a: activation energy (J kg^{-1})

k: reaction rate constant (units vary by reaction order)

NOx: generalized nitrogen oxides

$g_{x,y,z}$: gravitational acceleration in x, y, or z-direction (m s^{-2})

H: enthalpy (J)

h: specific enthalpy (J kg^{-1})

$I_{b\lambda}$: blackbody intensity (W m^2 μm^{-1} sr^{-1})

I_λ: spectral intensity (W m^{-1} sr^{-1})

$\mathscr{M}_\mathrm{i}$ molar mass of species i (kg kmol^{-1})

M_P: mass of incipient soot particle

n: refractive index

OI: oxygen index

p: pressure (Pa)

p_i: partial pressure of species i (Pa)

Q: heat flux (W m^{-3} s^{-1})

Q: volumetric flow rate (m^3 s^{-1})

$\boldsymbol{q}$: heat flux vector (W m^{-2} s^{-1})

R: specific gas constant (J kg^{-1} K^{-1})

$R_{i,r}$: reaction rate of species i participating in reaction r

R_S: reliability based on integration error

S_{acc}: accumulated error

S_i: integration error due to discretization

S_{max}: maximum allowable error

S_T: total error

S_ϕ: source term for general scalar quantity

T: temperature (K)

t: time (s)

T_α: activation temperature for soot nucleation (K)

T_b: bulk fluid temperature (K)

T_γ: activation temperature for soot surface growth (K)

T_f: final temperature (K)

T_o: initial (reference) temperature (K)

T_ω: activation temperature for soot oxidation (K)

V: volume (m^3)

$\boldsymbol{V}$: total velocity vector ($m\ s^{-1}$)

u: x-directional component of the velocity vector ($m\ s^{-1}$)

v: y-directional component of the velocity vector ($m\ s^{-1}$)

w: z-directional component of the velocity vector ($m\ s^{-1}$)

w_i: emission weighting factor for species i

X_i: mole fraction of species i

X_{sgs}: mole fraction of surface growth species

Y_i: mass fraction of species i

ΔH_f: heat of formation (J)

ΔH_{rxn}: heat of reaction (J)

Γ_i: diffusion coefficient of species i

λ: wavelength (m)

μ_t: turbulent viscosity

η_{coll}: collisional efficiency

ρ: density (kg m^{-3})

σ: Stefan-Boltzmann constant (W m^{-2} K^{-4})

$\sigma_{nuc/soot}$: turbulent Prandtl numbers for nuclei or soot transport

σ_s: scattering coefficient (m^{-1})

τ_{ij}: viscous stress

Φ: equivalence ratio

ϕ: general variable in transport equations

ω_i: rate of generation or consumption of chemical species i (kg m^{-3} s^{-1})

Ω': solid angle (sr)

APPENDIX B

PHYSICAL AND CHEMICAL PROPERTIES OF ETHYLENE

Selected Physical Properties

The table below shows the major chemical and physical properties of ethylene [107] routinely encountered in analytical or numerical evaluation of combustion processes.

Table B.1. Selected physical properties of ethylene

Name(s)	Ethylene, Ethene, Acetene, Olefiant Gas
Chemical Formula	C_2H_4
Molecular Weight	28.054 g/mol
Boiling Point	169 K
Flash point	137 K
Specific Gravity (relative to air)	0.978
Density	40.6 mol/m^3
Thermal Conductivity	0.020 W/m K
Dyanmic Viscosity	0.0103 cP
Kinematic Viscosity	9.05 cSt
Gibbs Free Energy of Formation	68 kJ/mol
Standard Heat of Formation	52.4 kJ/mol
Standard Heat of Combustion	-1411 kj/mol
Heat capacity, Cp	42.9 J/mol K
Heat capacity, Cv	
Standard Molar Entropy	219.32 J/mol K
Vapor pressure	6.9449 Mpa
Solubility in water	0.131 mg/mL

Note: all properties given for gas phase at 298 K and 1 bar, unless otherwise specified

Flame Temperature Calculations for Different Combustion Scenarios

The following figures represent gas-phase equilibrium calculations based on minimization of Gibbs Free Energy during a combustion reaction between ethylene and several different mixtures of oxidizer. The calculations were performed with the GasEq software package.

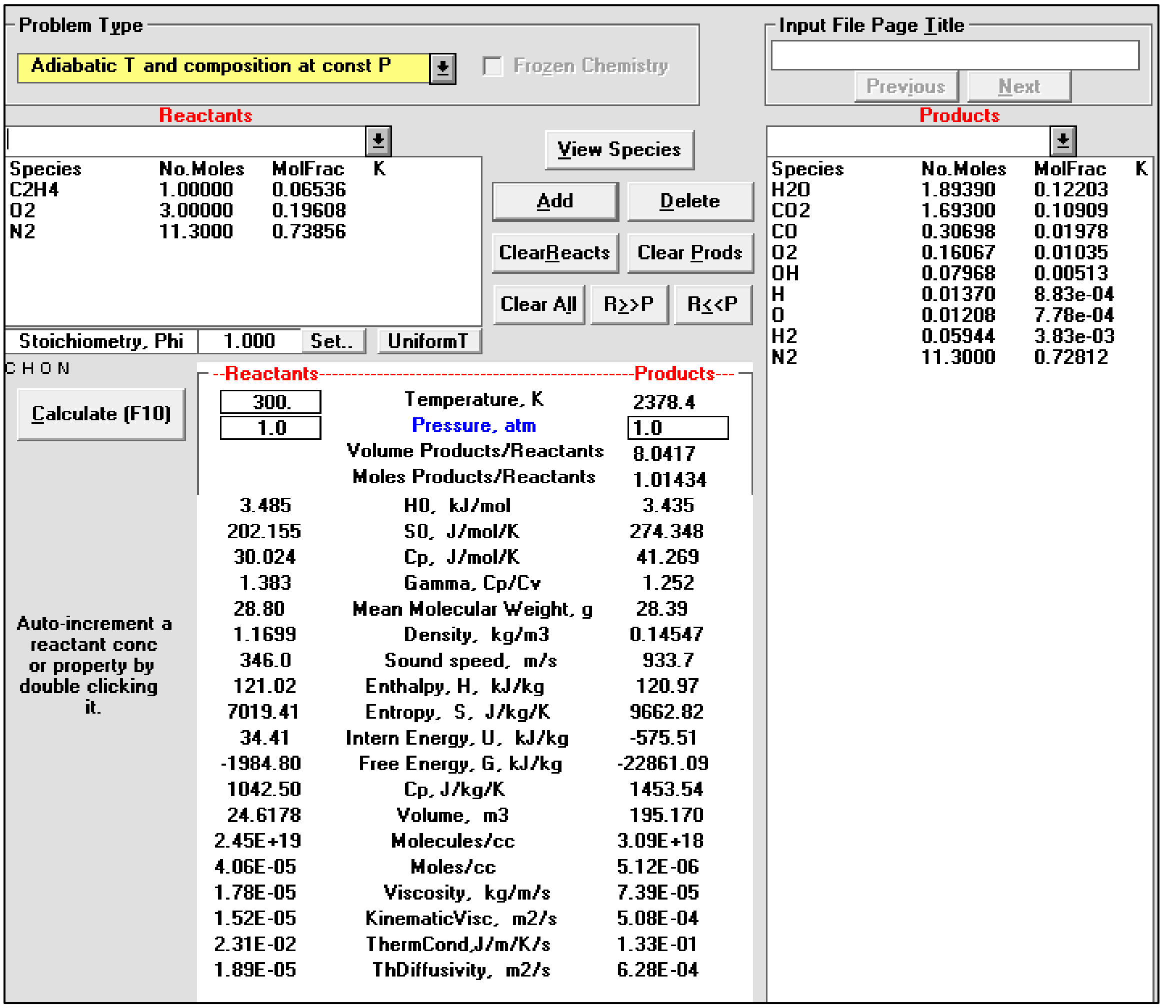

Problem Type: Adiabatic T and composition at const P

☐ Frozen Chemistry

Reactants

Species	No.Moles	MolFrac	K
C2H4	1.00000	0.06536	
O2	3.00000	0.19608	
N2	11.3000	0.73856	

Stoichiometry, Phi 1.000

Products

Species	No.Moles	MolFrac	K
H2O	1.89390	0.12203	
CO2	1.69300	0.10909	
CO	0.30698	0.01978	
O2	0.16067	0.01035	
OH	0.07968	0.00513	
H	0.01370	8.83e-04	
O	0.01208	7.78e-04	
H2	0.05944	3.83e-03	
N2	11.3000	0.72812	

--Reactants		Products---
300.	Temperature, K	2378.4
1.0	Pressure, atm	1.0
	Volume Products/Reactants	8.0417
	Moles Products/Reactants	1.01434
3.485	H0, kJ/mol	3.435
202.155	S0, J/mol/K	274.348
30.024	Cp, J/mol/K	41.269
1.383	Gamma, Cp/Cv	1.252
28.80	Mean Molecular Weight, g	28.39
1.1699	Density, kg/m3	0.14547
346.0	Sound speed, m/s	933.7
121.02	Enthalpy, H, kJ/kg	120.97
7019.41	Entropy, S, J/kg/K	9662.82
34.41	Intern Energy, U, kJ/kg	-575.51
-1984.80	Free Energy, G, kJ/kg	-22861.09
1042.50	Cp, J/kg/K	1453.54
24.6178	Volume, m3	195.170
2.45E+19	Molecules/cc	3.09E+18
4.06E-05	Moles/cc	5.12E-06
1.78E-05	Viscosity, kg/m/s	7.39E-05
1.52E-05	KinematicVisc, m2/s	5.08E-04
2.31E-02	ThermCond,J/m/K/s	1.33E-01
1.89E-05	ThDiffusivity, m2/s	6.28E-04

Auto-increment a reactant conc or property by double clicking it.

Figure B.1. Adiabatic flame temperature and equilibrium compositions for ethylene combustion in air under constant pressure conditions.

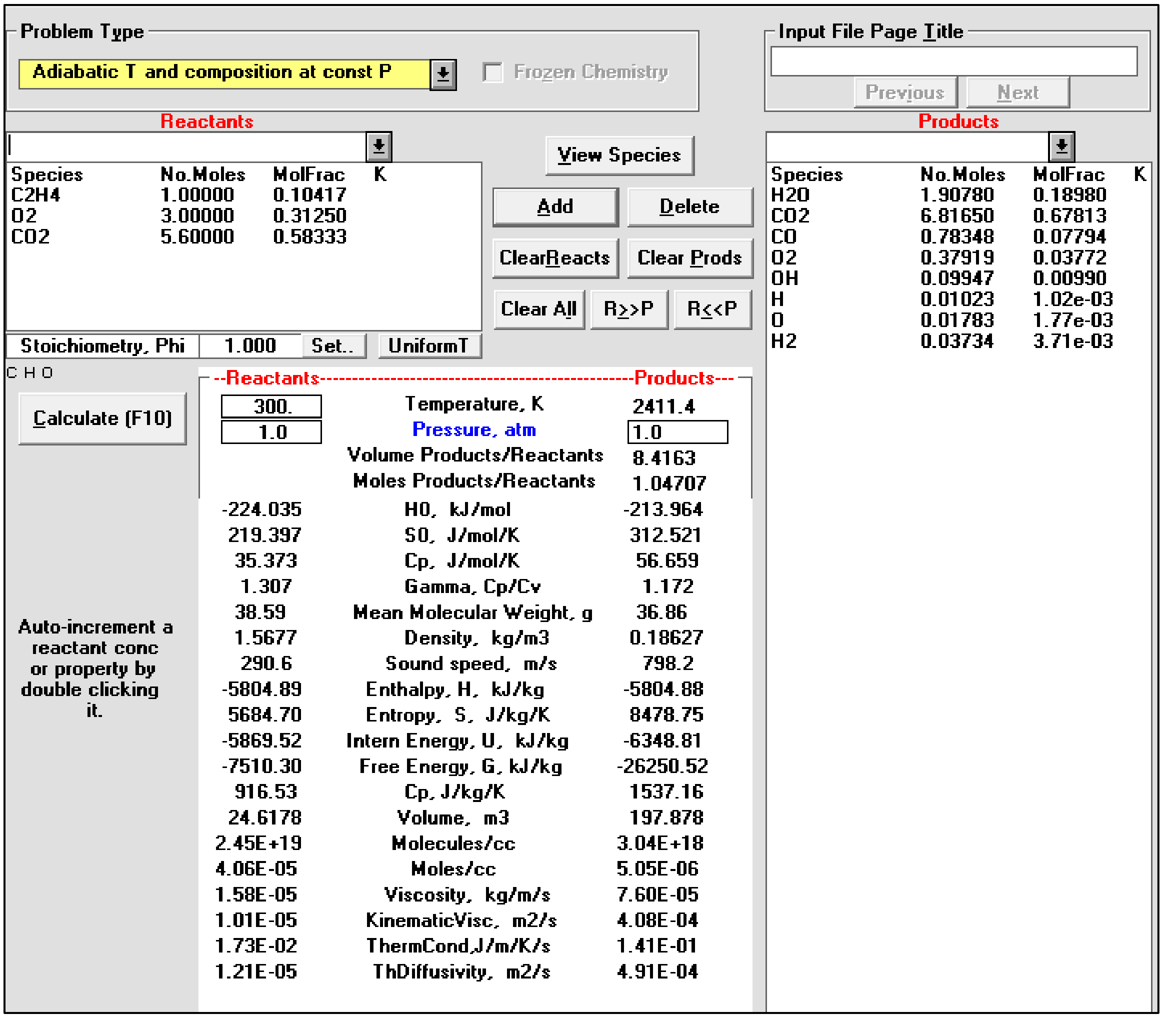

Problem Type: Adiabatic T and composition at const P

☐ Frozen Chemistry

Reactants

Species	No.Moles	MolFrac	K
C2H4	1.00000	0.10417	
O2	3.00000	0.31250	
CO2	5.60000	0.58333	

Stoichiometry, Phi 1.000

Products

Species	No.Moles	MolFrac	K
H2O	1.90780	0.18980	
CO2	6.81650	0.67813	
CO	0.78348	0.07794	
O2	0.37919	0.03772	
OH	0.09947	0.00990	
H	0.01023	1.02e-03	
O	0.01783	1.77e-03	
H2	0.03734	3.71e-03	

--Reactants		Products---
300.	Temperature, K	2411.4
1.0	Pressure, atm	1.0
	Volume Products/Reactants	8.4163
	Moles Products/Reactants	1.04707
-224.035	H0, kJ/mol	-213.964
219.397	S0, J/mol/K	312.521
35.373	Cp, J/mol/K	56.659
1.307	Gamma, Cp/Cv	1.172
38.59	Mean Molecular Weight, g	36.86
1.5677	Density, kg/m3	0.18627
290.6	Sound speed, m/s	798.2
-5804.89	Enthalpy, H, kJ/kg	-5804.88
5684.70	Entropy, S, J/kg/K	8478.75
-5869.52	Intern Energy, U, kJ/kg	-6348.81
-7510.30	Free Energy, G, kJ/kg	-26250.52
916.53	Cp, J/kg/K	1537.16
24.6178	Volume, m3	197.878
2.45E+19	Molecules/cc	3.04E+18
4.06E-05	Moles/cc	5.05E-06
1.58E-05	Viscosity, kg/m/s	7.60E-05
1.01E-05	KinematicVisc, m2/s	4.08E-04
1.73E-02	ThermCond,J/m/K/s	1.41E-01
1.21E-05	ThDiffusivity, m2/s	4.91E-04

Auto-increment a reactant conc or property by double clicking it.

Figure B.2. Adiabatic flame temperature and equilibrium compositions for ethylene combustion in 35% O_2 under constant pressure conditions.

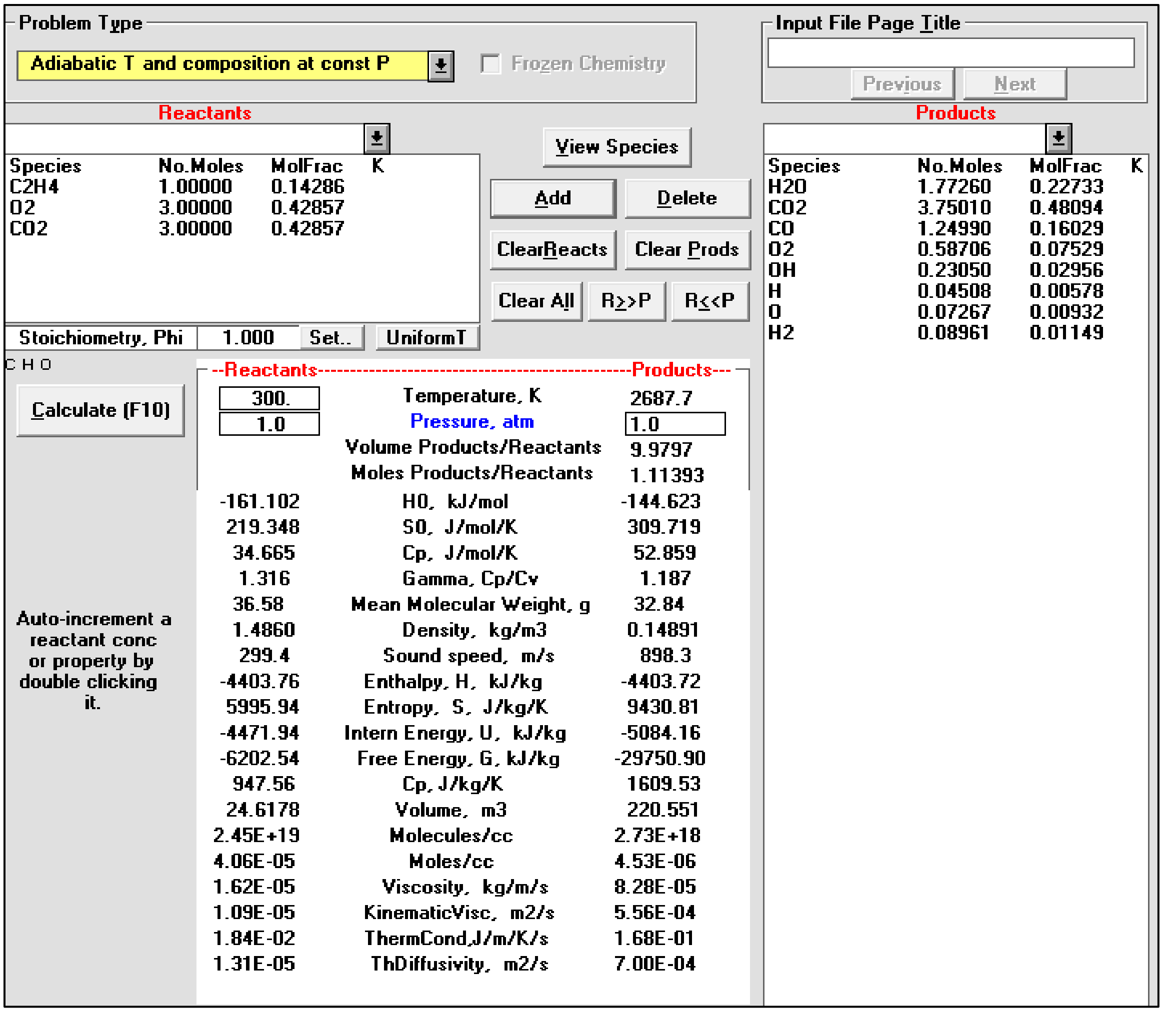

Problem Type: Adiabatic T and composition at const P

☐ Frozen Chemistry

Reactants

Species	No.Moles	MolFrac	K
C2H4	1.00000	0.14286	
O2	3.00000	0.42857	
CO2	3.00000	0.42857	

Stoichiometry, Phi 1.000

Products

Species	No.Moles	MolFrac	K
H2O	1.77260	0.22733	
CO2	3.75010	0.48094	
CO	1.24990	0.16029	
O2	0.58706	0.07529	
OH	0.23050	0.02956	
H	0.04508	0.00578	
O	0.07267	0.00932	
H2	0.08961	0.01149	

Auto-increment a reactant conc or property by double clicking it.

--Reactants--		--Products---
300.	Temperature, K	2687.7
1.0	Pressure, atm	1.0
	Volume Products/Reactants	9.9797
	Moles Products/Reactants	1.11393
-161.102	H0, kJ/mol	-144.623
219.348	S0, J/mol/K	309.719
34.665	Cp, J/mol/K	52.859
1.316	Gamma, Cp/Cv	1.187
36.58	Mean Molecular Weight, g	32.84
1.4860	Density, kg/m3	0.14891
299.4	Sound speed, m/s	898.3
-4403.76	Enthalpy, H, kJ/kg	-4403.72
5995.94	Entropy, S, J/kg/K	9430.81
-4471.94	Intern Energy, U, kJ/kg	-5084.16
-6202.54	Free Energy, G, kJ/kg	-29750.90
947.56	Cp, J/kg/K	1609.53
24.6178	Volume, m3	220.551
2.45E+19	Molecules/cc	2.73E+18
4.06E-05	Moles/cc	4.53E-06
1.62E-05	Viscosity, kg/m/s	8.28E-05
1.09E-05	KinematicVisc, m2/s	5.56E-04
1.84E-02	ThermCond,J/m/K/s	1.68E-01
1.31E-05	ThDiffusivity, m2/s	7.00E-04

Figure B.3. Adiabatic flame temperature and equilibrium compositions for ethylene combustion in 50% O_2 under constant pressure conditions.

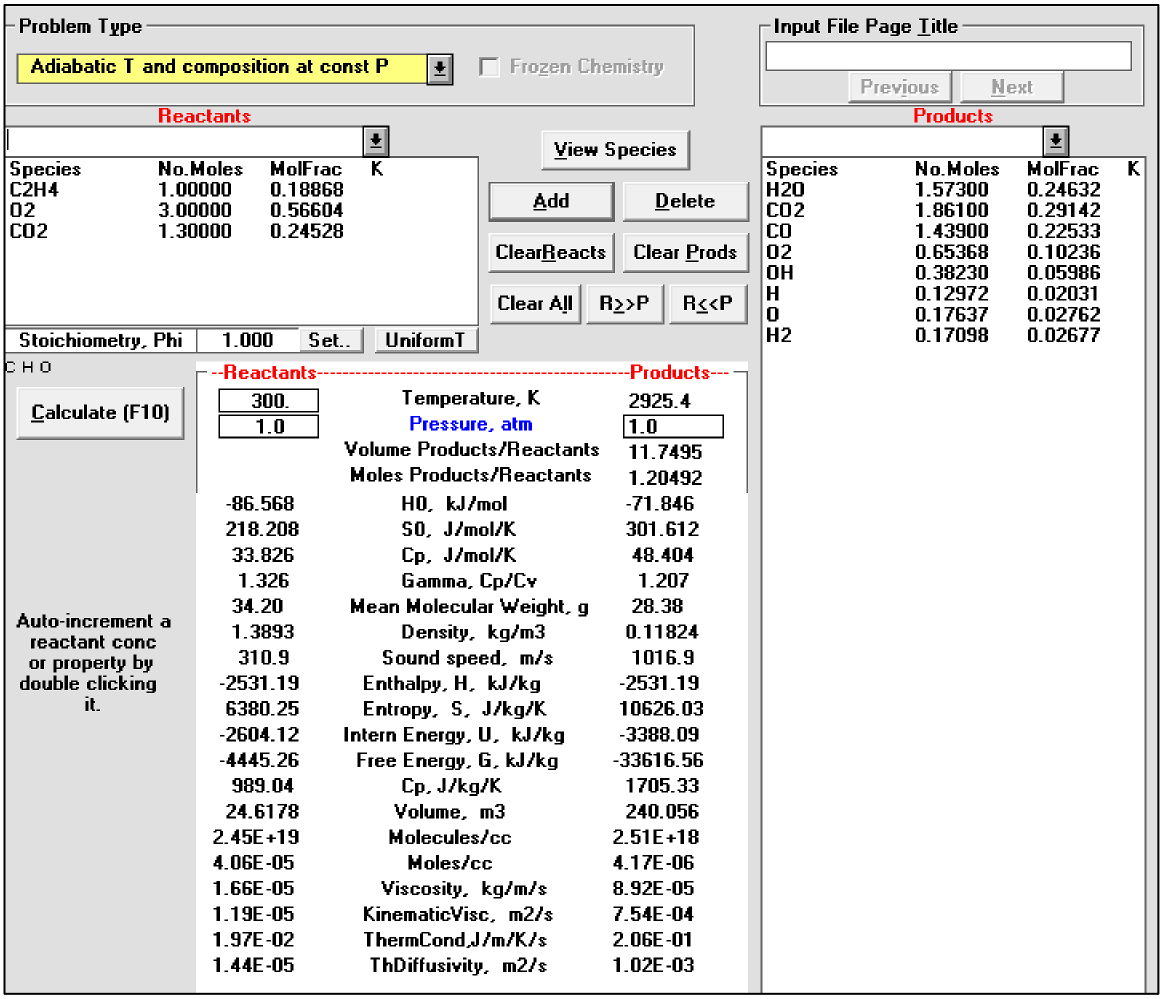

Problem Type: Adiabatic T and composition at const P

Reactants

Species	No.Moles	MolFrac	K
C2H4	1.00000	0.18868	
O2	3.00000	0.56604	
CO2	1.30000	0.24528	

Stoichiometry, Phi 1.000

Products

Species	No.Moles	MolFrac	K
H2O	1.57300	0.24632	
CO2	1.86100	0.29142	
CO	1.43900	0.22533	
O2	0.65368	0.10236	
OH	0.38230	0.05986	
H	0.12972	0.02031	
O	0.17637	0.02762	
H2	0.17098	0.02677	

--Reactants--		--Products--
300.	Temperature, K	2925.4
1.0	Pressure, atm	1.0
	Volume Products/Reactants	11.7495
	Moles Products/Reactants	1.20492
-86.568	H0, kJ/mol	-71.846
218.208	S0, J/mol/K	301.612
33.826	Cp, J/mol/K	48.404
1.326	Gamma, Cp/Cv	1.207
34.20	Mean Molecular Weight, g	28.38
1.3893	Density, kg/m3	0.11824
310.9	Sound speed, m/s	1016.9
-2531.19	Enthalpy, H, kJ/kg	-2531.19
6380.25	Entropy, S, J/kg/K	10626.03
-2604.12	Intern Energy, U, kJ/kg	-3388.09
-4445.26	Free Energy, G, kJ/kg	-33616.56
989.04	Cp, J/kg/K	1705.33
24.6178	Volume, m3	240.056
2.45E+19	Molecules/cc	2.51E+18
4.06E-05	Moles/cc	4.17E-06
1.66E-05	Viscosity, kg/m/s	8.92E-05
1.19E-05	KinematicVisc, m2/s	7.54E-04
1.97E-02	ThermCond,J/m/K/s	2.06E-01
1.44E-05	ThDiffusivity, m2/s	1.02E-03

Auto-increment a reactant conc or property by double clicking it.

Figure B.4. Adiabatic flame temperature and equilibrium compositions for ethylene combustion in 70% O_2 under constant pressure conditions.

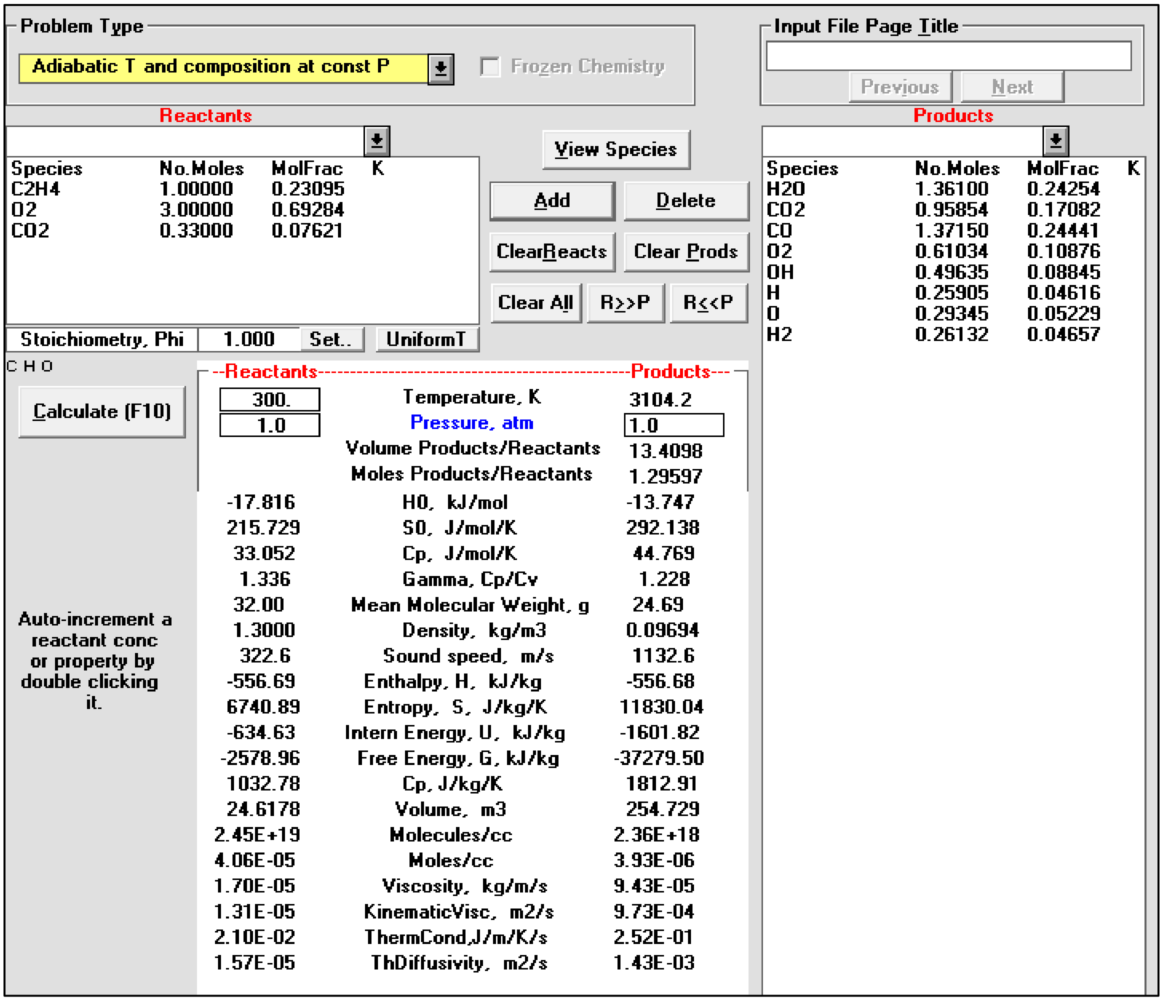

Problem Type: Adiabatic T and composition at const P

☐ Frozen Chemistry

Input File Page Title:

Reactants

Species	No.Moles	MolFrac	K
C2H4	1.00000	0.23095	
O2	3.00000	0.69284	
CO2	0.33000	0.07621	

Stoichiometry, Phi 1.000

Products

Species	No.Moles	MolFrac	K
H2O	1.36100	0.24254	
CO2	0.95854	0.17082	
CO	1.37150	0.24441	
O2	0.61034	0.10876	
OH	0.49635	0.08845	
H	0.25905	0.04616	
O	0.29345	0.05229	
H2	0.26132	0.04657	

--Reactants		Products---
300.	Temperature, K	3104.2
1.0	Pressure, atm	1.0
	Volume Products/Reactants	13.4098
	Moles Products/Reactants	1.29597
-17.816	H0, kJ/mol	-13.747
215.729	S0, J/mol/K	292.138
33.052	Cp, J/mol/K	44.769
1.336	Gamma, Cp/Cv	1.228
32.00	Mean Molecular Weight, g	24.69
1.3000	Density, kg/m3	0.09694
322.6	Sound speed, m/s	1132.6
-556.69	Enthalpy, H, kJ/kg	-556.68
6740.89	Entropy, S, J/kg/K	11830.04
-634.63	Intern Energy, U, kJ/kg	-1601.82
-2578.96	Free Energy, G, kJ/kg	-37279.50
1032.78	Cp, J/kg/K	1812.91
24.6178	Volume, m3	254.729
2.45E+19	Molecules/cc	2.36E+18
4.06E-05	Moles/cc	3.93E-06
1.70E-05	Viscosity, kg/m/s	9.43E-05
1.31E-05	KinematicVisc, m2/s	9.73E-04
2.10E-02	ThermCond,J/m/K/s	2.52E-01
1.57E-05	ThDiffusivity, m2/s	1.43E-03

Figure B.5. Adiabatic flame temperature and equilibrium compositions for ethylene combustion in 90% O_2 under constant pressure conditions.

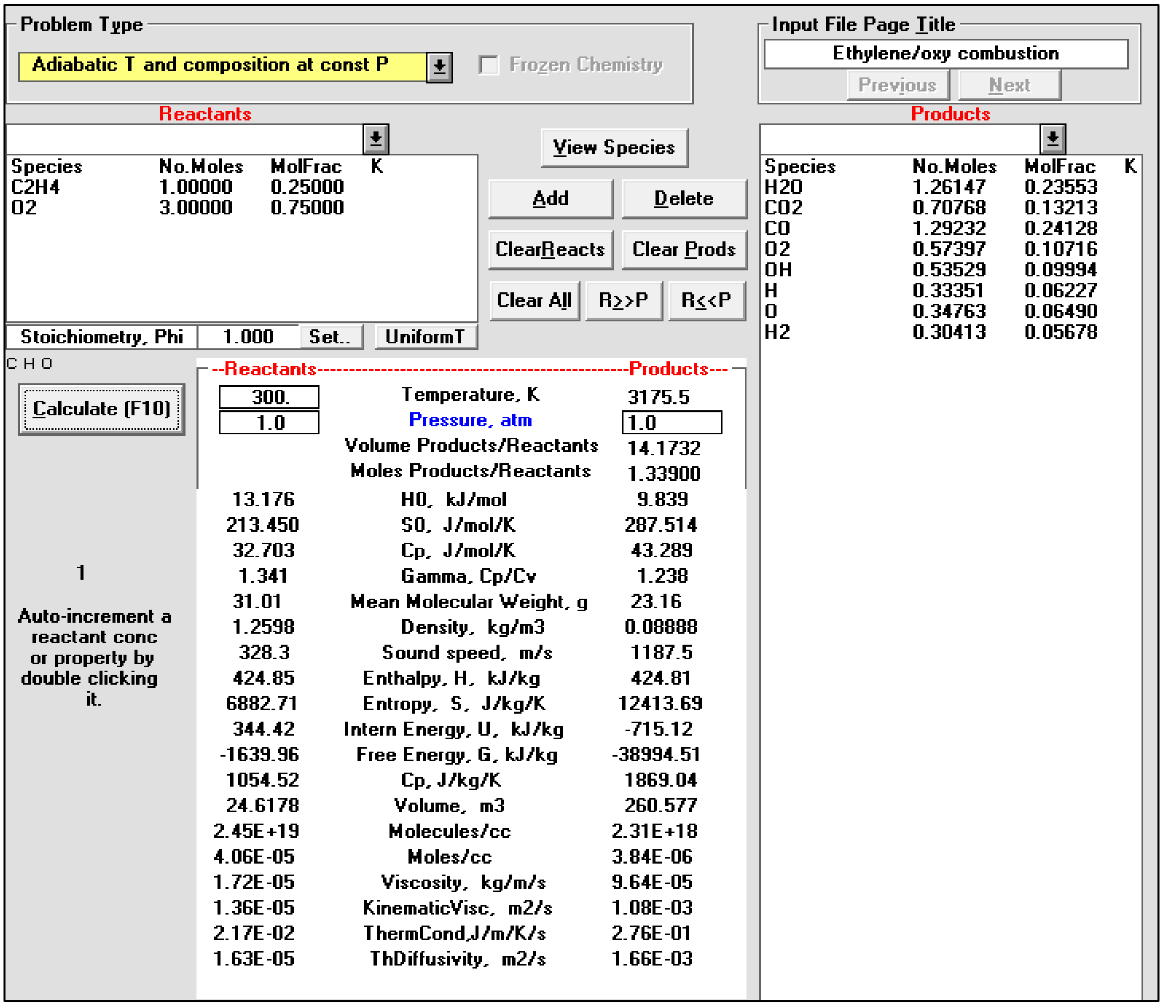

Problem Type: Adiabatic T and composition at const P

☐ Frozen Chemistry

Input File Page Title: Ethylene/oxy combustion

Reactants

Species	No.Moles	MolFrac	K
C2H4	1.00000	0.25000	
O2	3.00000	0.75000	

Stoichiometry, Phi: 1.000

C H O

Products

Species	No.Moles	MolFrac	K
H2O	1.26147	0.23553	
CO2	0.70768	0.13213	
CO	1.29232	0.24128	
O2	0.57397	0.10716	
OH	0.53529	0.09994	
H	0.33351	0.06227	
O	0.34763	0.06490	
H2	0.30413	0.05678	

--Reactants--		--Products--
300.	Temperature, K	3175.5
1.0	Pressure, atm	1.0
	Volume Products/Reactants	14.1732
	Moles Products/Reactants	1.33900
13.176	H0, kJ/mol	9.839
213.450	S0, J/mol/K	287.514
32.703	Cp, J/mol/K	43.289
1.341	Gamma, Cp/Cv	1.238
31.01	Mean Molecular Weight, g	23.16
1.2598	Density, kg/m3	0.08888
328.3	Sound speed, m/s	1187.5
424.85	Enthalpy, H, kJ/kg	424.81
6882.71	Entropy, S, J/kg/K	12413.69
344.42	Intern Energy, U, kJ/kg	-715.12
-1639.96	Free Energy, G, kJ/kg	-38994.51
1054.52	Cp, J/kg/K	1869.04
24.6178	Volume, m3	260.577
2.45E+19	Molecules/cc	2.31E+18
4.06E-05	Moles/cc	3.84E-06
1.72E-05	Viscosity, kg/m/s	9.64E-05
1.36E-05	KinematicVisc, m2/s	1.08E-03
2.17E-02	ThermCond,J/m/K/s	2.76E-01
1.63E-05	ThDiffusivity, m2/s	1.66E-03

1

Auto-increment a reactant conc or property by double clicking it.

Figure B.6. Adiabatic flame temperature and equilibrium compositions for ethylene combustion in 100% O_2 under constant pressure conditions.

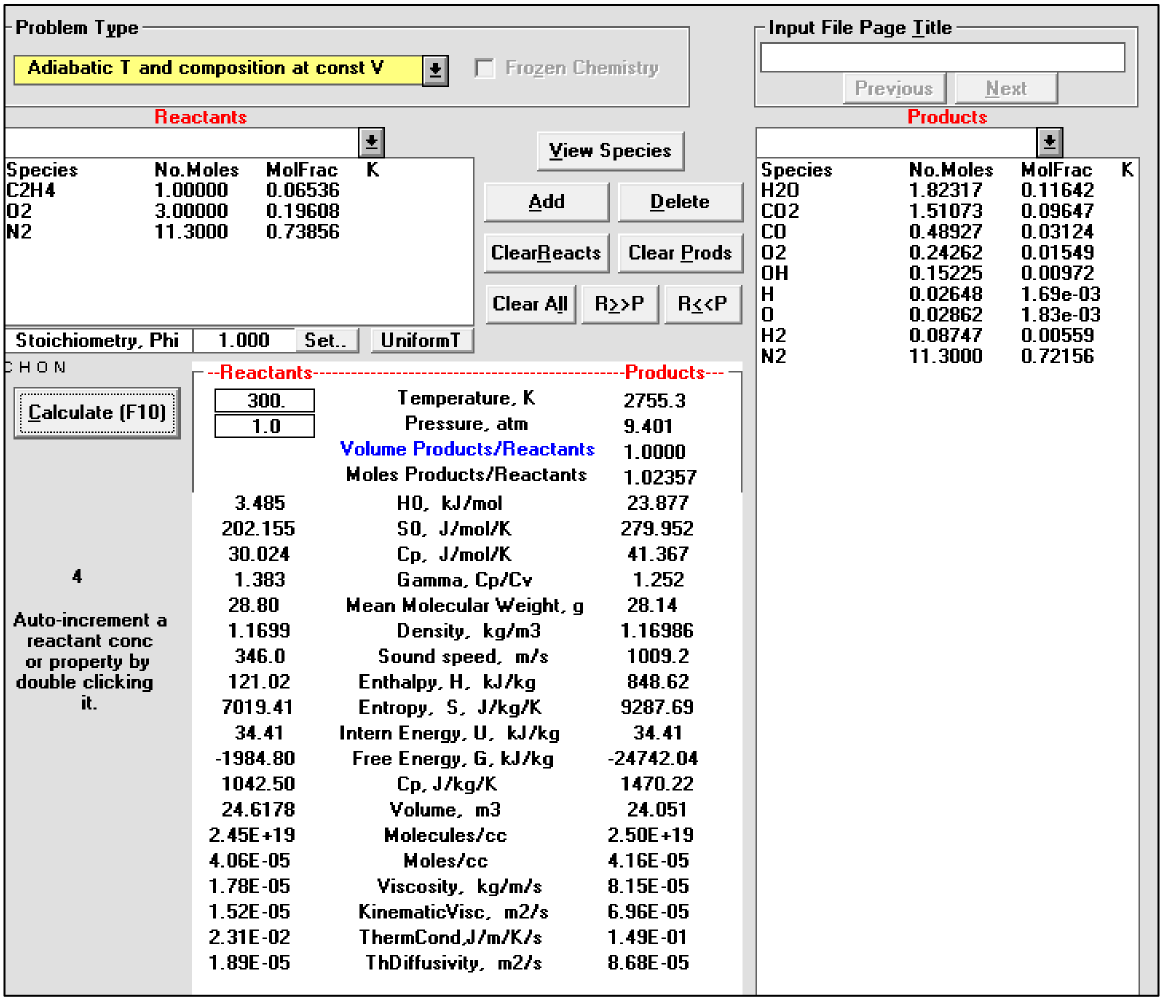

Problem Type: Adiabatic T and composition at const V

☐ Frozen Chemistry

Input File Page Title:

Reactants

Species	No.Moles	MolFrac	K
C2H4	1.00000	0.06536	
O2	3.00000	0.19608	
N2	11.3000	0.73856	

Stoichiometry, Phi 1.000

Products

Species	No.Moles	MolFrac	K
H2O	1.82317	0.11642	
CO2	1.51073	0.09647	
CO	0.48927	0.03124	
O2	0.24262	0.01549	
OH	0.15225	0.00972	
H	0.02648	1.69e-03	
O	0.02862	1.83e-03	
H2	0.08747	0.00559	
N2	11.3000	0.72156	

--Reactants		Products---
300.	Temperature, K	2755.3
1.0	Pressure, atm	9.401
	Volume Products/Reactants	1.0000
	Moles Products/Reactants	1.02357
3.485	H0, kJ/mol	23.877
202.155	S0, J/mol/K	279.952
30.024	Cp, J/mol/K	41.367
1.383	Gamma, Cp/Cv	1.252
28.80	Mean Molecular Weight, g	28.14
1.1699	Density, kg/m3	1.16986
346.0	Sound speed, m/s	1009.2
121.02	Enthalpy, H, kJ/kg	848.62
7019.41	Entropy, S, J/kg/K	9287.69
34.41	Intern Energy, U, kJ/kg	34.41
-1984.80	Free Energy, G, kJ/kg	-24742.04
1042.50	Cp, J/kg/K	1470.22
24.6178	Volume, m3	24.051
2.45E+19	Molecules/cc	2.50E+19
4.06E-05	Moles/cc	4.16E-05
1.78E-05	Viscosity, kg/m/s	8.15E-05
1.52E-05	KinematicVisc, m2/s	6.96E-05
2.31E-02	ThermCond,J/m/K/s	1.49E-01
1.89E-05	ThDiffusivity, m2/s	8.68E-05

Auto-increment a reactant conc or property by double clicking it.

Figure B.7. Isochoric flame temperature and equilibrium compositions for ethylene combustion in air under constant volume conditions.

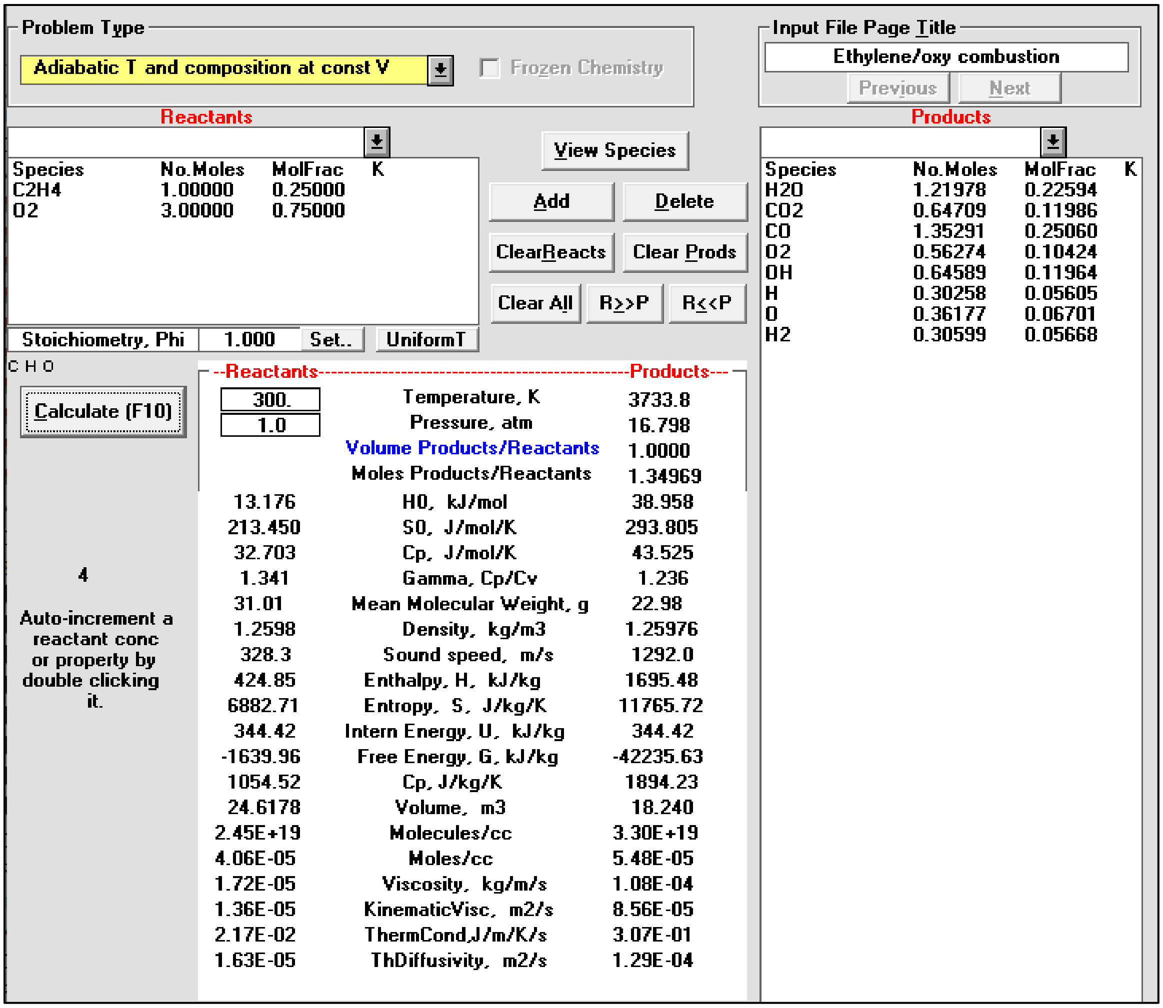

Problem Type: Adiabatic T and composition at const V

☐ Frozen Chemistry

Input File Page Title: Ethylene/oxy combustion

Reactants

Species	No.Moles	MolFrac	K
C2H4	1.00000	0.25000	
O2	3.00000	0.75000	

Stoichiometry, Phi 1.000

Products

Species	No.Moles	MolFrac	K
H2O	1.21978	0.22594	
CO2	0.64709	0.11986	
CO	1.35291	0.25060	
O2	0.56274	0.10424	
OH	0.64589	0.11964	
H	0.30258	0.05605	
O	0.36177	0.06701	
H2	0.30599	0.05668	

--Reactants--		--Products---
300.	Temperature, K	3733.8
1.0	Pressure, atm	16.798
	Volume Products/Reactants	1.0000
	Moles Products/Reactants	1.34969
13.176	H0, kJ/mol	38.958
213.450	S0, J/mol/K	293.805
32.703	Cp, J/mol/K	43.525
1.341	Gamma, Cp/Cv	1.236
31.01	Mean Molecular Weight, g	22.98
1.2598	Density, kg/m3	1.25976
328.3	Sound speed, m/s	1292.0
424.85	Enthalpy, H, kJ/kg	1695.48
6882.71	Entropy, S, J/kg/K	11765.72
344.42	Intern Energy, U, kJ/kg	344.42
-1639.96	Free Energy, G, kJ/kg	-42235.63
1054.52	Cp, J/kg/K	1894.23
24.6178	Volume, m3	18.240
2.45E+19	Molecules/cc	3.30E+19
4.06E-05	Moles/cc	5.48E-05
1.72E-05	Viscosity, kg/m/s	1.08E-04
1.36E-05	KinematicVisc, m2/s	8.56E-05
2.17E-02	ThermCond,J/m/K/s	3.07E-01
1.63E-05	ThDiffusivity, m2/s	1.29E-04

Figure B.8. Isochoric flame temperature and equilibrium compositions for ethylene combustion in 100% O_2 under constant volume conditions.

REFERENCES

1. I. Glassman, R. A. Yetter, and N. G. Glumac, *Combustion*. Academic Press, 2014.

2. "SIMON SAYS: Dr. Olefins provides his Economic Prognosis | Energy Trading Analytics International." [Online]. Available: https://etailpg.com/simon-says-dr-olefins-economic-prognosis. [Accessed: 14-Feb-2020].

3. R. and M. ltd, "The Ethylene Technology Report 2016 - Research and Markets." [Online]. Available: https://www.researchandmarkets.com/reports/3643672/the-ethylene-technology-report-2016. [Accessed: 09-Sep-2019].

4. C. Wang, Y. Zhao, and B. Zhang, "Numerical simulation of flame acceleration and deflagration-to-detonation transition of ethylene in channels," *Journal of Loss Prevention in the Process Industries*, vol. 43, pp. 120–126, Sep. 2016, doi: 10.1016/j.jlp.2016.05.008.

5. T. Araki, K. Yoshida, Y. Morii, N. Tsuboi, and A. K. Hayashi, "Numerical Analyses on Ethylene/Oxygen Detonation with Multistep Chemical Reaction Mechanisms: Grid Resolution and Chemical Reaction Model," *Combustion Science and Technology*, vol. 188, no. 3, pp. 346–369, Mar. 2016, doi: 10.1080/00102202.2015.1106484.

6. B. Demirgok, O. J. U. Almeyda, V. Akkerman, D. Valiev, V. Bychkov, and M.-H. Wu, "Analysis of ethylene-oxygen combustion in micro-pipes," presented at the Fall Technical Meeting of the Eastern States Section of the Combustion Institute 2013, 2013, pp. 155–160.

7. S. Turns, *An Introduction to Combustion: Concepts and Applications*. McGraw-Hill Higher Education, 1996.

8. J. M. Smith, H. C. V. Ness, and M. M. Abbott, *Introduction to Chemical Engineering Thermodynamics*. McGraw-Hill, 2005.

9. M. W. Chase, "NIST-JANAF Themochemical Tables, Fourth Edition," *J. Phys. Chem. Ref. Data, Monograph 9*, pp. 1–1951, 1998.

10. "Oxyfuel Combustion - an overview | ScienceDirect Topics." [Online]. Available: https://www.sciencedirect.com/topics/engineering/oxyfuel-combustion. [Accessed: 12-Sep-2019].

11. J. Wendt, *Computational Fluid Dynamics: An Introduction*. Springer Science & Business Media, 2008.

12. O. Zikanov, *Essential Computational Fluid Dynamics*. John Wiley & Sons, 2011.

13. J. D. Anderson, *Modern Compressible Flow: With Historical Perspective*. McGraw-Hill Education, 2003.

14. H. S. Fogler, *Elements of chemical reaction engineering*, 4th ed.. Upper Saddle River, NJ: Prentice Hall PTR, 2006.

15. G. Pio, V. Palma, and E. Salzano, "Comparison and Validation of Detailed Kinetic Models for the Oxidation of Light Alkenes," *Ind. Eng. Chem. Res.*, vol. 57, no. 21, pp. 7130–7135, May 2018, doi: 10.1021/acs.iecr.8b01377.

16. B. Fabiano, F. Pistritto, A. Reverberi, and E. Palazzi, "Ethylene–air mixtures under flowing conditions: a model-based approach to explosion conditions," *Clean Technologies and Environmental Policy*, vol. 17, no. 5, pp. 1261–1270, Jun. 2015, doi: 10.1007/s10098-015-0966-1.

17. D. J. Singh and C. J. Jachimowski, "Quasiglobal reaction model for ethylene combustion," *AIAA Journal*, vol. 32, no. 1, pp. 213–216, 1994, doi: 10.2514/3.11972.

18. C. Xu and A. A. Konnov, "Validation and analysis of detailed kinetic models for ethylene combustion," *Energy*, vol. 43, no. 1, pp. 19–29, Jul. 2012, doi: 10.1016/j.energy.2011.11.006.

19. N. Zettervall, C. Fureby, and E. J. K. Nilsson, "Small Skeletal Kinetic Reaction Mechanism for Ethylene–Air Combustion," *Energy Fuels*, vol. 31, no. 12, pp. 14138–14149, Dec. 2017, doi: 10.1021/acs.energyfuels.7b02078.

20. "Adiabatic Flame Temperatures," *Engineering ToolBox*. [Online]. Available: https://www.engineeringtoolbox.com/adiabatic-flame-temperature-d_996.html. [Accessed: 16-Sep-2019].

21. N. O. of D. and Informatics, "NIST Chemistry WebBook." [Online]. Available: https://webbook.nist.gov/chemistry/. [Accessed: 16-Sep-2019].

22. P. W. Cooper, *Explosives Engineering*. John Wiley & Sons, 2018.

23. "GRI-Mech 3.0." [Online]. Available: http://combustion.berkeley.edu/gri-mech/version30/text30.html. [Accessed: 17-Sep-2019].

24. "Chemical Mechanism: Combustion Research Group at UC San Diego." [Online]. Available: http://web.eng.ucsd.edu/mae/groups/combustion/mechanism.html. [Accessed: 17-Sep-2019].

25. B. Varatharajan and F. A. Williams, “Ethylene Ignition and Detonation Chemistry, Part 1: Detailed Modeling and Experimental Comparison,” *Journal of Propulsion and Power*, vol. 18, no. 2, pp. 344–351, 2002, doi: 10.2514/2.5940.

26. G. Jomaas, X. L. Zheng, D. L. Zhu, and C. K. Law, “Experimental determination of counterflow ignition temperatures and laminar flame speeds of C2–C3 hydrocarbons at atmospheric and elevated pressures,” *Proceedings of the Combustion Institute*, vol. 30, no. 1, pp. 193–200, Jan. 2005, doi: 10.1016/j.proci.2004.08.228.

27. R. Perry and D. Green, *Perry’s Chemical Engineers’ Handbook, Eighth Edition*. McGraw-Hill Education, 2008.

28. J. R. Howell, M. P. Menguc, and R. Siegel, *Thermal Radiation Heat Transfer, 5th Edition*. CRC Press, 2010.

29. H. Abdul-Sater, G. Krishnamoorthy, and M. Ditaranto, “Predicting Radiative Heat Transfer in Oxy-Methane Flame Simulations: An Examination of Its Sensitivities to Chemistry and Radiative Property Models,” *Journal of Combustion*, vol. 2015, pp. 1–20, Feb. 2015, doi: 10.1155/2015/439520.

30. L.-H. Dorey, N. Bertier, L. Tessé, and F. Dupoirieux, “Soot and radiation modeling in laminar ethylene flames with tabulated detailed chemistry,” *Comptes Rendus Mécanique*, vol. 339, no. 12, pp. 756–769, Dec. 2011, doi: 10.1016/j.crme.2011.09.004.

31. I. Hernández, G. Lecocq, D. Poitou, E. Riber, and B. Cuenot, “Computations of soot formation in ethylene/air counterflow diffusion flames and its interaction with radiation,” *Comptes Rendus Mécanique*, vol. 341, no. 1, pp. 238–246, Jan. 2013, doi: 10.1016/j.crme.2012.11.005.

32. Y. Zhang, F. Liu, and C. Lou, “Experimental and Numerical Investigations of Soot Formation in Laminar Coflow Ethylene Flames Burning in O2/N2 and O2/CO2 Atmospheres at Different O2 Mole Fractions,” *Energy Fuels*, vol. 32, no. 5, pp. 6252–6263, May 2018, doi: 10.1021/acs.energyfuels.7b04069.

33. G. Krishnamoorthy, M. Sami, S. Orsino, A. Perera, M. Shahnam, and E. D. Huckaby, “Radiation modelling in oxy-fuel combustion scenarios,” *International Journal of Computational Fluid Dynamics*, vol. 24, no. 3–4, pp. 69–82, Mar. 2010, doi: 10.1080/10618562.2010.485567.

34. R. S. Barlow, A. N. Karpetis, J. H. Frank, and J.-Y. Chen, “Scalar profiles and NO formation in laminar opposed-flow partially premixed methane/air flames,” *Combustion and Flame*, vol. 127, no. 3, pp. 2102–2118, Nov. 2001, doi: 10.1016/S0010-2180(01)00313-3.

35. G. Krishnamoorthy and L. N. Mulenga, “Impact of Radiative Losses on Flame Acceleration and Deflagration to Detonation Transition of Lean Hydrogen-Air Mixtures in a Macro-Channel with Obstacles,” *Fluids*, vol. 3, no. 4, p. 104, Dec. 2018, doi: 10.3390/fluids3040104.

36. N. Malik, T. Løvås, and F. Mauss, “The Effect of Preferential Diffusion on the Soot Initiation Process in Ethylene Diffusion Flames,” *Flow Turbulence Combust*, vol. 87, no. 2, p. 293, Mar. 2011, doi: 10.1007/s10494-011-9347-y.

37. F. Escudero *et al.*, “Effects of oxygen index on soot production and temperature in an ethylene inverse diffusion flame,” *Experimental Thermal and Fluid Science*, vol. 73, pp. 101–108, May 2016, doi: 10.1016/j.expthermflusci.2015.09.029.

38. M.-H. Wu and C.-Y. Wang, “Reaction propagation modes in millimeter-scale tubes for ethylene/oxygen mixtures,” *Proceedings of the Combustion Institute*, vol. 33, no. 2, pp. 2287–2293, 2011, doi: 10.1016/j.proci.2010.07.081.

39. E. S. Oran and V. N. Gamezo, “Origins of the deflagration-to-detonation transition in gas-phase combustion,” *Combustion and Flame*, vol. 148, no. 1, pp. 4–47, 2007, doi: 10.1016/j.combustflame.2006.07.010.

40. G. B. Goodwin, R. W. Houim, and E. S. Oran, “Shock transition to detonation in channels with obstacles,” *Proceedings of the Combustion Institute*, vol. 36, no. 2, pp. 2717–2724, 2017, doi: 10.1016/j.proci.2016.06.160.

41. M. Wu, M. P. Burke, S. F. Son, and R. A. Yetter, “Flame acceleration and the transition to detonation of stoichiometric ethylene/oxygen in microscale tubes,” *Proceedings of the Combustion Institute*, vol. 31, no. 2, pp. 2429–2436, 2007, doi: 10.1016/j.proci.2006.08.098.

42. M. A. Liberman, A. D. Kiverin, and M. F. Ivanov, “On detonation initiation by a temperature gradient for a detailed chemical reaction models,” *Physics Letters A*, vol. 375, no. 17, pp. 1803–1808, 2011, doi: 10.1016/j.physleta.2011.03.026.

43. E. S. Oran, “Stochasticity and Dynamics of High-Speed Reactive Flows,” *AIP Conference Proceedings*, vol. 1376, no. 1, pp. 38–44, Sep. 2011, doi: 10.1063/1.3651830.

44. M. A. Liberman, M. F. Ivanov, A. D. Kiverin, M. S. Kuznetsov, A. A. Chukalovsky, and T. V. Rakhimova, “Deflagration-to-detonation transition in highly reactive combustible mixtures,” *Acta Astronautica*, vol. 67, no. 7, pp. 688–701, 2010, doi: 10.1016/j.actaastro.2010.05.024.

45. W. Han, Y. Gao, and C. K. Law, “Flame acceleration and deflagration-to-detonation transition in micro- and macro-channels: An integrated mechanistic study,” *Combustion and Flame*, vol. 176, pp. 285–298, Feb. 2017, doi: 10.1016/j.combustflame.2016.10.010.

46. D. M. Valiev, V. Bychkov, V. Akkerman, L.-E. Eriksson, and C. K. Law, “Quasi-steady stages in the process of premixed flame acceleration in narrow channels,” *Physics of Fluids*, vol. 25, no. 9, 2013, doi: 10.1063/1.4819885.

47. M. A. Liberman, M. Kuznetsov, A. Ivanov, and I. Matsukov, “Formation of the preheated zone ahead of a propagating flame and the mechanism underlying the deflagration-to-detonation transition,” *Physics Letters A*, vol. 373, no. 5, pp. 501–510, 2009, doi: 10.1016/j.physleta.2008.12.008.

48. V. Akkerman, V. Bychkov, M. Kuznetsov, C. K. Law, D. Valiev, and M.-H. Wu, “Fast flame acceleration and deflagration-to-detonation transition in smooth and obstructed tubes, channels and slits,” *8th US National Combustion Meeting 2013*, vol. 2, pp. 970–978, Jan. 2013.

49. D. M. Valiev, V. Bychkov, V. Akkerman, and L.-E. Eriksson, “Different stages of flame acceleration from slow burning to Chapman-Jouguet deflagration,” *Physical Review E*, vol. 80, no. 3, 2009.

50. R. W. Houim, A. Ozgen, and E. S. Oran, “The role of spontaneous waves in the deflagration-to-detonation transition in submillimetre channels,” *Combustion Theory and Modelling*, vol. 20, no. 6, pp. 1068–1087, Nov. 2016, doi: 10.1080/13647830.2016.1249523.

51. F. Xu, P. B. Sunderland, and G. M. Faeth, “Soot formation in laminar premixed ethylene/air flames at atmospheric pressure,” *Combustion and Flame*, vol. 108, no. 4, pp. 471–493, Mar. 1997, doi: 10.1016/S0010-2180(96)00200-3.

52. A. Fuentes, R. Henríquez, F. Nmira, F. Liu, and J.-L. Consalvi, “Experimental and numerical study of the effects of the oxygen index on the radiation characteristics of laminar coflow diffusion flames,” *Combustion and Flame*, vol. 160, no. 4, pp. 786–795, Apr. 2013, doi: 10.1016/j.combustflame.2012.12.005.

53. F. Escudero, A. Fuentes, J.-L. Consalvi, F. Liu, and R. Demarco, “Unified behavior of soot production and radiative heat transfer in ethylene, propane and butane axisymmetric laminar diffusion flames at different oxygen indices,” *Fuel*, vol. 183, pp. 668–679, Nov. 2016, doi: 10.1016/j.fuel.2016.06.126.

54. J. Y. Hwang and S. H. Chung, “Growth of soot particles in counterflow diffusion flames of ethylene,” *Combustion and Flame*, vol. 125, no. 1, pp. 752–762, Apr. 2001, doi: 10.1016/S0010-2180(00)00234-0.

55. M. R. J. Charest, H. I. Joo, Ö. L. Gülder, and C. P. T. Groth, “Experimental and numerical study of soot formation in laminar ethylene diffusion flames at elevated pressures from 10 to 35atm,” *Proceedings of the Combustion Institute*, vol. 33, no. 1, pp. 549–557, Jan. 2011, doi: 10.1016/j.proci.2010.07.054.

56. F. Liu, A. E. Karataş, Ö. L. Gülder, and M. Gu, “Numerical and experimental study of the influence of CO2 and N2 dilution on soot formation in laminar coflow C2H4/air diffusion flames at pressures between 5 and 20atm,” *Combustion and Flame*, vol. 162, no. 5, pp. 2231–2247, May 2015, doi: 10.1016/j.combustflame.2015.01.020.

57. H. Guo, Z. Gu, K. A. Thomson, G. J. Smallwood, and F. F. Baksh, “Soot formation in a laminar ethylene/air diffusion flame at pressures from 1 to 8atm,” *Proceedings of the Combustion Institute*, vol. 34, no. 1, pp. 1795–1802, Jan. 2013, doi: 10.1016/j.proci.2012.07.006.

58. B. J. P. Buhre, L. K. Elliott, C. D. Sheng, R. P. Gupta, and T. F. Wall, “Oxy-fuel combustion technology for coal-fired power generation,” *Progress in Energy and Combustion Science*, vol. 31, no. 4, pp. 283–307, Jan. 2005, doi: 10.1016/j.pecs.2005.07.001.

59. R. Demarco, J.-L. Consalvi, and A. Fuentes, “A calibrated soot production model for ethylene inverse diffusion flames at different Oxygen Indexes,” *Fuel*, vol. 212, pp. 1–11, Jan. 2018, doi: 10.1016/j.fuel.2017.10.038.

60. B. M. Ayyub, *Numerical analysis for engineers: methods and applications*, Second edition.. Boca Raton: CRC Press, Taylor & Francis Group, 2016.

61. C.-W. Shu, “WENO methods,” *Scholarpedia*, vol. 6, no. 5, p. 9709, May 2011, doi: 10.4249/scholarpedia.9709.

62. A. Chinnayya, A. Hadjadj, and D. Ngomo, “Computational study of detonation wave propagation in narrow channels,” *Physics of Fluids*, vol. 25, no. 3, p. 36101, Mar. 2013, doi: 10.1063/1.4792708.

63. M. Fukuda, E. Dzieminska, A. Hayashi, E. Yamada, and N. Tsuboi, “Effect of wall conditions on DDT in hydrogen–oxygen mixtures,” *Shock Waves*, vol. 23, no. 3, pp. 191–200, May 2013, doi: 10.1007/s00193-013-0444-9.

64. T. Machida, M. Asahara, A. K. Hayashi, and N. Tsuboi, “Three-Dimensional Simulation of Deflagration-to-Detonation Transition with a Detailed Chemical Reaction Model,” *Combustion Science and Technology*, vol. 186, no. 10–11, pp. 1758–1773, Nov. 2014, doi: 10.1080/00102202.2014.935647.

65. K. Gottiparthi, F. Genin, S. Srinivasan, and S. Menon, “Simulation of Cellular Detonation Structures in Ethylene-Oxygen Mixtures,” in *47th AIAA Aerospace Sciences Meeting including The New Horizons Forum and Aerospace Exposition*, Orlando, Florida, 2009, doi: 10.2514/6.2009-437.

66. T. Ahmad, S. L. Plee, and J. P. Myers, “Fluent User’s Guide,” p. 2692.

67. T. Ahmad, S. L. Plee, and J. P. Myers, “Fluent Theory Guide,” p. 814.

68. E. S. Oran, *Numerical simulation of reactive flow*. New York: Elsevier, 1987.

69. N. Kubota, *Propellants and Explosives: Thermochemical Aspects of Combustion*. John Wiley & Sons, 2015.

70. H. Wang *et al.*, “USC Mech Version II. High-Temperature Combustion Reaction Model of H2/CO/C1-C4 Compounds,” May-2007. [Online]. Available: http://ignis.usc.edu/Mechanisms/USC-Mech%20II/USC_Mech%20II.htm. [Accessed: 01-Oct-2019].

71. B. Varatharajan and F. A. Williams, “Ethylene Ignition and Detonation Chemistry, Part 2: Ignition Histories and Reduced Mechanisms,” *Journal of Propulsion and Power*, vol. 18, no. 2, pp. 352–362, 2002, doi: 10.2514/2.5941.

72. H. Abdul-Sater and G. Krishnamoorthy, “An assessment of radiation modeling strategies in simulations of laminar to transitional, oxy-methane, diffusion flames,” *Applied Thermal Engineering*, vol. 61, no. 2, pp. 507–518, Nov. 2013, doi: 10.1016/j.applthermaleng.2013.08.027.

73. G. Krishnamoorthy, “A new weighted-sum-of-gray-gases model for CO2–H2O gas mixtures,” *International Communications in Heat and Mass Transfer*, vol. 37, no. 9, pp. 1182–1186, Nov. 2010, doi: 10.1016/j.icheatmasstransfer.2010.07.007.

74. T. Løvås, N. Malik, and F. Mauss, “Global reaction mechanism for ethylene flames with preferential diffusion,” *Combustion Science and Technology*, vol. 182, no. 11–12, pp. 1945–1960, 2010, doi: 10.1080/00102202.2010.497419.

75. G. B. Goodwin, R. W. Houim, and E. S. Oran, “Effect of decreasing blockage ratio on DDT in small channels with obstacles,” *Combustion and Flame*, vol. 173, pp. 16–26, Nov. 2016, doi: 10.1016/j.combustflame.2016.07.029.

76. N. Tsuboi, Y. Morii, and A. K. Hayashi, “Two-dimensional numerical simulation on galloping detonation in a narrow channel,” *Proceedings of the Combustion Institute*, vol. 34, no. 2, pp. 1999–2007, Jan. 2013, doi: 10.1016/j.proci.2012.06.132.

77. V. B. Nguyen, J.-M. Li, P.-H. Chang, C. J. Teo, and B. C. Khoo, “Effect of ethylene fuel/air equivalence ratio on the dynamics of deflagration-to-detonation transition and detonation propagation process,” *Combustion Science and Technology*, vol. 190, no. 9, pp. 1630–1658, Sep. 2018, doi: 10.1080/00102202.2018.1461091.

78. T. Xi, J. Di, Y. Li, S. Dai, C. Ma, and J. Zhao, “Measurement of ultrafast combustion process of premixed ethylene/oxygen flames in narrow channel with digital holographic interferometry,” *Opt. Express*, vol. 26, no. 22, p. 28497, Oct. 2018, doi: 10.1364/OE.26.028497.

79. J. Li, P. Zhang, L. Yuan, Z. Pan, and Y. Zhu, “Flame propagation and detonation initiation distance of ethylene/oxygen in narrow gap,” *Applied Thermal Engineering*, vol. 110, pp. 1274–1282, Jan. 2017, doi: 10.1016/j.applthermaleng.2016.09.037.

80. R. Mercier *et al.*, “Experimental and numerical investigation of the influence of thermal boundary conditions on premixed swirling flame stabilization,” *Combustion and Flame*, vol. 171, pp. 42–58, Sep. 2016, doi: 10.1016/j.combustflame.2016.05.006.

81. K. Maruta, T. Kataoka, N. I. Kim, S. Minaev, and R. Fursenko, “Characteristics of combustion in a narrow channel with a temperature gradient,” *Proceedings of the Combustion Institute*, vol. 30, no. 2, pp. 2429–2436, Jan. 2005, doi: 10.1016/j.proci.2004.08.245.

82. A. Brambilla, M. Schultze, C. E. Frouzakis, J. Mantzaras, R. Bombach, and K. Boulouchos, “An experimental and numerical investigation of premixed syngas combustion dynamics in mesoscale channels with controlled wall temperature profiles,” *Proceedings of the Combustion Institute*, vol. 35, no. 3, pp. 3429–3437, Jan. 2015, doi: 10.1016/j.proci.2014.06.131.

83. J. Ott, E. Oran, and J. Anderson, “A Mechanism for Flame Acceleration in Narrow Tubes,” *AIAA Journal*, vol. 41, no. 7, pp. 1391–1396, 2003, doi: 10.2514/2.2088.

84. E. Dziemińska and A. K. Hayashi, “Auto-ignition and DDT driven by shock wave – Boundary layer interaction in oxyhydrogen mixture,” *International Journal of Hydrogen Energy*, vol. 38, no. 10, pp. 4185–4193, Apr. 2013, doi: 10.1016/j.ijhydene.2013.01.111.

85. G. Krishnamoorthy, “Assessing uncertainties in prevailing methodologies for modeling radiative transfer in simulations of oxygen-enriched methane flames,” *J Braz. Soc. Mech. Sci. Eng.*, vol. 39, no. 10, pp. 4231–4248, Oct. 2017, doi: 10.1007/s40430-017-0896-4.

86. E. Schultz and J. Shepherd, “Validation of Detailed Reaction Mechanisms for Detonation Simulation,” 08-Feb-2000. [Online]. Available: https://resolver.caltech.edu/CaltechGALCITFM:1999.005. [Accessed: 28-Jun-2019].

87. N. N. Smirnov, V. B. Betelin, V. F. Nikitin, L. I. Stamov, and D. I. Altoukhov, “Accumulation of errors in numerical simulations of chemically reacting gas dynamics,” *Acta Astronautica*, vol. 117, pp. 338–355, Dec. 2015, doi: 10.1016/j.actaastro.2015.08.013.

88. W. L. Grosshandler, “RADCAL -- a narrow-band model for radiation calculations in a combustion environment.” National Institute of Standards and Technology, Building and Fire Research Laboratory, 1993.

89. M. R. Busupally and A. De, “Numerical modeling of soot formation in a turbulent C2H4/air diffusion flame,” *International Journal of Spray and Combustion Dynamics*, vol. 8, no. 2, pp. 67–85, Jun. 2016, doi: 10.1177/1756827716638814.

90. F. Liu, H. Guo, G. J. Smallwood, and Ö. L. Gülder, “The chemical effects of carbon dioxide as an additive in an ethylene diffusion flame: implications for soot and NOx formation,” *Combustion and Flame*, vol. 125, no. 1, pp. 778–787, Apr. 2001, doi: 10.1016/S0010-2180(00)00241-8.

91. K. M. Leung, R. P. Lindstedt, and W. P. Jones, “A simplified reaction mechanism for soot formation in nonpremixed flames,” *Combustion and Flame*, vol. 87, no. 3, pp. 289–305, Dec. 1991, doi: 10.1016/0010-2180(91)90114-Q.

92. K.-O. Lee *et al.*, “Soot formation effects of oxygen concentration in the oxidizer stream of laminar coannular nonpremixed methane/air flames,” *Combustion and Flame*, vol. 121, no. 1, pp. 323–333, Apr. 2000, doi: 10.1016/S0010-2180(99)00131-5.

93. C. P. Leusden and N. Peters, “Experimental and numerical analysis of the influence of oxygen on soot formation in laminar counterflow flames of acetylene,” *Proceedings of the Combustion Institute*, vol. 28, no. 2, pp. 2619–2625, Jan. 2000, doi: 10.1016/S0082-0784(00)80680-3.

94. S. J. Brookes and J. B. Moss, “Predictions of soot and thermal radiation properties in confined turbulent jet diffusion flames,” *Combustion and Flame*, vol. 116, no. 4, pp. 486–503, Mar. 1999, doi: 10.1016/S0010-2180(98)00056-X.

95. Q. Wang *et al.*, “Experimental assessment of the sudden-reversal of the oxygen dilution effect on soot production in coflow ethylene flames,” *Combustion and Flame*, vol. 183, pp. 242–252, Sep. 2017, doi: 10.1016/j.combustflame.2017.05.001.

96. I. Saanum and M. Ditaranto, “Soot formation in diffusion flames in oxy-fuel atmospheres,” p. 2, 2015, http://www.sintef.no/.

97. S. M. Hverven, “Laser Induced Incandescence with Long Pulse Duration,” Norwegian University of Science and Technology, Trondheim, 2013.

98. F. G. Roper, “The prediction of laminar jet diffusion flame sizes: Part I. Theoretical model,” *Combustion and Flame*, vol. 29, pp. 219–226, Jan. 1977, doi: 10.1016/0010-2180(77)90112-2.

99. M. A. Mikofski, T. C. Williams, C. R. Shaddix, and L. G. Blevins, “Flame height measurement of laminar inverse diffusion flames,” *Combustion and Flame*, vol. 146, no. 1, pp. 63–72, Jul. 2006, doi: 10.1016/j.combustflame.2006.04.006.

100. F. G. Roper, C. Smith, and A. C. Cunningham, “The prediction of laminar jet diffusion flame sizes: Part II. Experimental verification,” *Combustion and Flame*, vol. 29, pp. 227–234, Jan. 1977, doi: 10.1016/0010-2180(77)90113-4.

101. R. W. Elliott and H. Watts, “Diffusion of some Hydrocarbons in Air: a Regularity in the Diffusion Coefficients of a Homologous Series,” *Can. J. Chem.*, vol. 50, no. 1, pp. 31–34, Jan. 1972, doi: 10.1139/v72-005.

102. J. B. Moss, C. D. Stewart, and K. J. Syed, “Flowfield modelling of soot formation at elevated pressure,” *Symposium (International) on Combustion*, vol. 22, no. 1, pp. 413–423, Jan. 1989, doi: 10.1016/S0082-0784(89)80048-7.

103. A. Snegirev, E. Markus, E. Kuznetsov, J. Harris, and T. Wu, “On soot and radiation modeling in buoyant turbulent diffusion flames,” *Heat Mass Transfer*, vol. 54, no. 8, pp. 2275–2293, Aug. 2018, doi: 10.1007/s00231-017-2198-x.

104. G. Ma, J. Z. Wen, M. F. Lightstone, and M. J. Thomson, “Optimization of Soot Modeling in Turbulent Nonpremixed Ethylene/Air Jet Flames,” *Combustion Science and Technology*, vol. 177, no. 8, pp. 1567–1602, Aug. 2005, doi: 10.1080/00102200590956786.

105. K. B. Lee, M. W. Thring, and J. M. Beér, “On the rate of combustion of soot in a laminar soot flame,” *Combustion and Flame*, vol. 6, pp. 137–145, Jan. 1962, doi: 10.1016/0010-2180(62)90082-2.

106. C. P. Fenimore and G. W. Jones, “Oxidation of soot by hydroxyl radicals,” *J. Phys. Chem.*, vol. 71, no. 3, pp. 593–597, Feb. 1967, doi: 10.1021/j100862a021.

107. “Ethylene - Thermophysical Properties.” [Online]. Available: https://www.engineeringtoolbox.com/ethylene-ethene-C2H4-properties-d_2104.html. [Accessed: 13-Feb-2020].